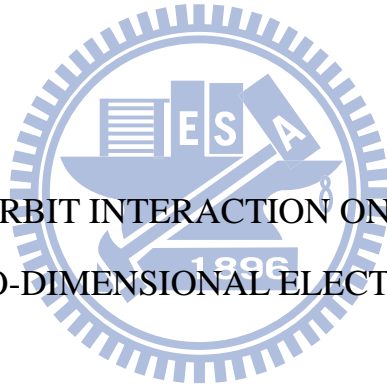


國立交通大學

電子物理研究所

碩士論文

自旋軌道作用對奈米圖形二維電子系統的影響



EFFECTS SPIN-ORBIT INTERACTION ON A NANO-PATTERNED
TWO-DIMENSIONAL ELECTRON GAS

研究生：蘇韋綾

指導教授：朱仲夏 教授

中華民國一百年七月

自旋軌道作用對奈米圖形二維電子系統的影響

**EFFECTS SPIN-ORBIT INTERACTION ON A NANO-PATTERNED
TWO-DIMENSIONAL ELECTRON GAS**

研究生：蘇韋綾

Student : Wei-Ling Su

指導教授：朱仲夏教授

Advisor : Prof. Chon Saar Chu

國立交通大學

電子物理研究所



A Thesis
Submitted to Department of Electrophysics
College of Science
National Chiao Tung University
in Partial Fulfillment of the Requirements
for the Degree of
Master
in
Electrophysics

July 2010

Hsinchu, Taiwan, Republic of China

中華民國一百年七月

自旋軌道作用對奈米圖形二維電子系統的影響

研究生：蘇韋綾

指導教授：朱仲夏教授

國立交通大學

電子物理研究所

摘要

我們考慮電子狀態在三角形週期電壓下的二維電子氣體中，有多對狄拉克角錐的結構在倒空間中的 K 點被找到。由於週期性的平面電位差造成的有效自旋軌道交互作用，導致在狄拉克點上的錐狀結構打開一個能隙。

與石墨烯的 Chern 值做比較，此週期性三角結構系統的 Chern 值不為零，是由於此系統(三角形週期晶格)有以垂直平面方向做轉軸旋轉 60 度倍數的系統對稱性。

由於拓撲學中的不變量 Z_2 值以及 Chern 值，可預期在樣品邊界擁有相反方向傳輸的邊緣態以及量子自旋霍爾效應是存在此系統的。此自旋軌道交互作用是造成此系統有拓撲絕緣相位的原因。

EFFECTS SPIN-ORBIT INTERACTION ON A NANO-PATTERNED TWO-DIMENSIONAL ELECTRON GAS

Student: Wei-Ling Su

Advisor: Prof. Chon-Saar Chu

Department of Electrophysics

National Chiao Tung University

Abstract

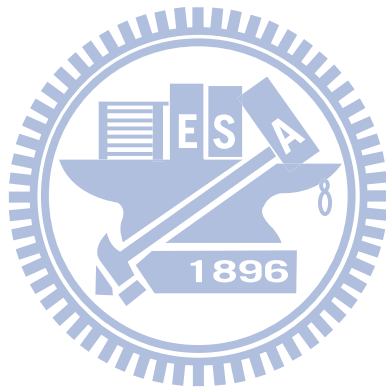
We consider the electronic state of a two-dimensional electron gas in a muffin-tin potential triangular lattice. Several Dirac cone structures at the \mathbf{K} points in the reciprocal space have been obtained.

Effects of spin-orbit interaction due to the in-plane potential gradient of the muffin-tin potential have been studied in detail. We find that gap opening at the Dirac points can lead to global gaps. In contrast to the graphene case, the Chern number of an energy band for a given spin state is nonzero. This is due to the rotational symmetry by rotating about an axis normal to the system by 60° .

As a result the system has a topological Z_2 invariant and we expected it to support helical edge states in the open boundary case. The spin-orbit interaction is thus shown to drive the system into a topological insulating phase.

致謝

感謝朱老師兩年來的指導，細心謹慎、清楚的邏輯思維以及做研究的耐心，深深的影響了我，讓我受益良多。並感謝實驗室的唐志雄學長在口試前的建議、律堯學長幫我修改論文、志宣學長教我程式的使用、榮興學長的人生開導以及其他同學悌鐳、文長、學弟儀玗、隔壁實驗室的同學們、伯儀學長、吉偉學長、呂智國博士、蔡政展學長、系辦的黃偉德先生的陪伴，也感謝陳衛國老師的狗 happy 在我做研究感到疲憊時露出可愛的動作撫慰我的心靈。謝謝我的父母、哥哥、奶奶以及關心我的親戚、朋友，感謝交大電物的人力和資源讓我順利完成碩士學位。



Contents

Abstract in Chinese	i
Abstract in English	ii
Acknowledgement	iii
1 Introduction	1
1.1 Background	1
1.1.1 spin-orbit coupling in solid-state system	1
1.1.2 Quantum Hall effect	4
1.1.3 Quantum spin Hall effect	4
1.2 Motivation	6
1.3 A guiding tour to this thesis	9
2 Energy band structure without SOI effect	10
2.1 Energy band structure for a muffin-tin potential lattice in 2DEG	10
2.1.1 The Analytical result by perturbation method	15
2.2 The numerical result compare with single well system	18
2.3 Brief summary	20
3 Energy band structure with SOI effect	21
3.1 Muffin-tin potential lattice in the presence of SOI	21
3.1.1 The Analytical result in the presence of SOI by perturbation method	23

CONTENTS

3.2	The position symmetry for muffin-tin triangular lattice	27
3.3	The numerical result compare with single well system in the presence of SOI	29
3.4	Results for energy band structure in the presence of SOI	32
3.5	The relationship between time reversal property and our system	34
3.6	Brief summary	36
4	Berry curvature with SOI effect in our system	37
4.1	Berry phase	37
4.2	Berry curvature analysis	38
4.2.1	The analytic result of Berry curvature	40
4.2.2	The Berry curvature of numerical result compare with the analytic result	42
4.2.3	The relationship between time reversal property and Berry curvature	44
4.2.4	The numerical result of Berry curvature	46
4.3	Brief summary and discussion	48
5	Searching for quantum spin Hall effect in our system	50
5.1	The Chern number of the energy band	50
5.2	Z_2 invariant	53
5.3	Brief summary	56
6	Conclusion and future work	59
6.1	Conclusion	59
6.2	future work	60
A	Labeling the periodic wave function basis K points	61
B	The calculations about the periodic potential coefficient V'_m	63
C	The numerical results of high energy bands structure	67

CONTENTS

D	The Berry curvature of numerical results for high energy bands	69
E	The other parameters for our system	72



List of Figures

1.1	The graphene structure (hexagon lattice) in (a) and the energy dispersion which have Dirac cones in (b). Ref: http://en.wikipedia.org/wiki/Graphene .	6
1.2	(a) Scanning electron microscopy images of the nano-patterned modulation-doped GaAs/AlGaAs sample. [11]. (b)The conduction bands and valence bands of each AlGaAs and GaAs produce the states interaction making 2DEG.	7
1.3	The energy dispersion of MTP (hexagon lattice). [11].	8
1.4	A muffin-tin type with a center to center distance a . The potential is U_0 inside the disk with diameter d and zero outside.	8
1.5	The lowest two energy bands dispersion of a hexagonal 2DEG superlattice.	9
2.1	The Brillouin zone of hexagonal lattice.	11
2.2	The lowest two energy bands calculation of a hexagonal 2DEG superlattice . The Dirac point energy which is at the crossing of the two bands.	13
2.3	The contour of energy dispersion for (a) the first lowest band, (b) the second lowest band which $m^* = 0.023m_e$, $a=40\text{nm}$, $d=0.663a$ and $U_0=165\text{meV}$	14
2.4	This figure shows the wave function which be expanded to $\mathbf{K}_1, \mathbf{K}_2, \mathbf{K}_3$ by \mathbf{G}_m	15

LIST OF FIGURES

2.5 The energy band structure for (a) the numerical MTP in 2DEG system. Compared the energy level with (b) the single well in 2DEG system. $U_0 = -300\text{meV}$, $a = 40\text{nm}$; $d=0.663a$ 19

3.1 The lowest two bands which wave vector is near K_1 ($k_y=0$, $-0.1K_1 < k_x < 0.1K_1$). The red line: the numerical result for three K point with SOI; blue line: the analytic result for 2×2 matrix with SOI, $\lambda=120\text{\AA}^2$ (InAs); $m^* = 0.023m_e$; $U_0 = 165\text{meV}$; $a=40\text{nm}$; $d=0.663a$ 27

3.2 This figure shows the rotating symmetry property for triangular lattice, the original system (a) in real-space correspond to (a) in k-space, then rotate $\frac{\pi}{3}$ from central point to become (b) in real-space and k-space , and do the same work to become (c) in real-space and k-space, where \tilde{n} is an integer(the blue point note the system which has been rotated). 28

3.3 Energy band structure with parameters units typical for InAs are: effective mass $m^*=0.023m_e$; $a = 40\text{nm}$; SO coupling constant $\lambda=120\text{\AA}^2$ (a) numerical muffin-tin potential ($U_0 = -300\text{meV}$) in the presence of SOI. Compared with (b) single well ($V_0=300\text{meV}$) in 2DEG. 31

3.4 Parameters units typical for InAs are: effective mass $m^*=0.023m_e$; $U_0 = 165\text{meV}$, $a = 40\text{nm}$; SO coupling constant $\lambda=120\text{\AA}^2$ The blue line is without SOI and the red line is with SOI which spin-up and spin -down are flipping in muffin-tin lattice 32

3.5 The lowest two bands which wave vector is near K_1 . Red circle: the system with SOI; blue star: the system without SOI, $\lambda=120\text{\AA}^2$ (InAs); $m^* = 0.023m_e$; $U_0 = 165\text{meV}$; $a=40\text{nm}$; $d=0.663a$ 33

3.6 This figure shows the value of gap for first lowest energy band and second lowest energy band which depend on C_{range} (show in appendix A). 34

4.1	The inset shows the contour of Berry curvature for the lowest band (in spin-up case) by considering three K point and we chose (a) $k_y=0k_{y_{\max}}$, (b) $k_y=0.3k_{y_{\max}}$ and (c) $k_y=0.6k_{y_{\max}}$ (black line) corresponding to the dispersion which is expanded from $K_1 (k_x = k_y = 0)$ in the main panel. The blue line is analytic result $n=-1, s=1 (C_{range}=1)$; the red line is numerical result (the lowest band).	42
4.2	The inset shows the contour of Berry curvature for the second lowest band (in spin up case) by considering three K point and we chose (a) $k_y=0k_{y_{\max}}$, (b) $k_y=0.3k_{y_{\max}}$ and (c) $k_y=0.6k_{y_{\max}}$ (black line) corresponding to the dispersion which is expanded from $K_1 (k_x = k_y = 0)$ in the main panel. The blue line is analytic result $n=1, s=1 (C_{range}=1)$; the red line is numerical result (the second lowest band).	43
4.3	The C_{range} increase to 11, the numerical Berry curvature would almost stable.	44
4.4	The Berry curvature of the lowest energy band for $n=1$ (a) the contour for spin-up (b) the contour for spin-down ($n'=2,3$); $\lambda=120\text{\AA}^2$ (InAs); $m^* = 0.023m_e$; $U_0 = 165\text{meV}$; $a=40\text{nm}$; $d=0.663a$ (where $k_x=k_y=0$ is Γ point). .	47
4.5	The Berry curvature of the second lowest energy band for $n=1$ (a) the contour for spin-up (b) the contour for spin-down ($n'=2,3$); $\lambda=120\text{\AA}^2$ (InAs); $m^* = 0.023m_e$; $U_0 = 165\text{meV}$; $a=40\text{nm}$; $d=0.663a$ (where $k_x=k_y=0$ is Γ point).	48
4.6	The (a) show the energy dispersion of graphene in BZ. (b) The Berry curvature of graphene in BZ. [15]	49
4.7	There are without rotating symmetry in graphene, which imply $K \neq K'$ in k-space (the blue point note the system which has been rotated).	49

LIST OF FIGURES

5.1 The rotating symmetry property for triangular lattice, the original system in real-space correspond to the BZ in k-space (top right), rotating x axis 180° the position in real-space is not change (the blue point note the system which has been rotated) and k_y becomes $-k_y$ in k-space (bottom right). The (a) shows the pink triangular is the smallest repeated unit cell in BZ. 51

5.2 The hexagon black line shows the area of Brillouin zone and the area of triangle dashed line is the basic area for integrating which we mention at below in main panel, and the inset shows the contour of Berry curvature near K_1 (red box) is isotropic with κ 52

5.3 The numerical results of Chern number for first lowest band (the blue line in top right figure). 53

5.4 Quantum spin Hall effect: the upper edge contains a forward mover(like a magnetic field \mathbf{B} with \hat{z} direction) with up spin and a backward mover (like a magnetic field \mathbf{B} with $-\hat{z}$ direction) with down spin, and conversely for the lower edge. 54

5.5 (Color online)Edge states in the quantum spin Hall insulator (QSHI). (a) The interface between a QSHI and an ordinary insulator. (b) The edge state dispersion in the graphene model in which up(blue arrow) and down(green arrow) spins propagate in opposite directions [20]. 55

5.6 The sketches show the electronic structure (energy versus momentum) for a trivial insulator (left) and a strong topological insulator (right), such as $\text{Bi}_{1-x}\text{Sb}_x$. In both cases, there are allowed electron states (black lines) introduced by the surface that lie in the bulk band gap (the bulk valence and conduction bands are indicated by the green and blue lines, respectively). In the trivial case, even a small perturbation (changing the chemistry of the surface) can open a gap in the surface states, but in the nontrivial case, the conducting surface states are protected.(Illustration: Alan Stonebraker/stonebrakerdesignworks.com) 56

5.7 This figure shows Chern number of spin-up and spin-down for each energy bands and the comparison for Fermi energy, $C_{\uparrow_{occupied}}$, $C_{\downarrow_{occupied}}$, Z_2 number. 57

5.8 The setup of experiment, we use the external bias making the n-dope layer to control the Fermi energy. 58

A.1 The number m includes two index v_1, v_2 ; the green arrows denote the basis vector $\mathbf{b}_1, \mathbf{b}_2$ in k -space; the green point is K_1 which is the expanded point for wave function; the red points are all K points for m ; the hexagons are Brillouin zones and the blue circles are defined as a number: C_{range} 62

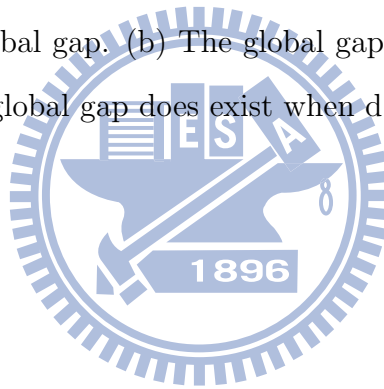
B.1 A muffin-tin type with center-to-center distance a . The external potential energy is U_0 inside the disk with diameter d and zero outside the disk. . . 63

C.1 This figure shows the contours of energy band structure without spin-orbit interaction for (a) the third lowest band (b) the fourth lowest band (c) the fifth lowest band (d) the sixth lowest band (e) the seventh lowest band, and the parameter is $m^* = 0.023m_e$, $a=40\text{nm}$, $d=0.663a$ and $U_0=165\text{ meV}$. 68

D.1 The energy dispersion in present SOI in our system, and the parameters are $m^* = 0.023m_e$, $a=40\text{nm}$, $d=0.663a$ and $U_0=165\text{ meV}$ 70

D.2 This figure shows the contours of Berry curvature of numerical results with spin-orbit interaction for spin-up (a) the third lowest band (b) the fourth lowest band (c) the fifth lowest band (d) the sixth lowest band (e) the seventh lowest band. (where $m^* = 0.023m_e$, $a=40\text{nm}$, $d=0.663a$ and $U_0=165\text{meV}$; $k_x = k_y = 0$ is Γ point.) 71

E.1 (a)The contour plot of the energy gap for the lowest two band by various parameters a , d but a fixed $U_0=165\text{meV}$. The red line denotes the maximum gap when $d/a=0.663$ for all a , the white arrows denote that the systems without global gap at K point for $a=15,20,30\dots(\text{nm})$ correspond to those rates, so we roughly estimate the minimum rate line is the white dash line for having global gap. (b) The global gap does not exist for $d = 0.1a$, $a=40\text{nm}$ (c) The global gap does exist when $d = 0.2a$, $a=40\text{nm}$ 73



Chapter 1

Introduction

1.1 Background

Recently, graphene have attracted a lot of studies because graphene has Dirac points structure at each corners of Brillouin zone. Therefore, to find out new structure with Dirac cone by artificial fabrication in semiconductors can be addressed an important issue. In realistic case we must consider the spin-orbit interaction for our case (see chapter1). Another interesting topic is quantum spin Hall state which has a special property for electrons transmission with certain spin helix.

1.1.1 spin-orbit coupling in solid-state system

Electron spin, the only internal degree of freedom of electrons, follows naturally from the Dirac equation when Dirac tried to put wave function in a covariant form, when space and time appear on equal footing. A nonrelativistic limit of the Dirac equation gives rise to the spin-orbit interaction term, that has been found great success in atomic energy spectra. The spin-orbit interaction, in vacuum can be expressed by [2]

$$H_{\text{SO}} = -\frac{e\hbar}{4m_0^2c^2} \boldsymbol{\sigma} \cdot (\mathbf{E} \times \mathbf{p}) = \frac{\hbar}{4m_0^2c^2} \boldsymbol{\sigma} \cdot (\nabla V \times \mathbf{p}), \quad (1.1)$$

where m_0 is the free electron mass, \hbar the Planck constant and c the light speed of light. The physical mechanism of H_{SO} can be interpreted: an electron moving in an electric potential region sees, in its frame of reference, an effective magnetic field which couples with the electron spin through the magnetic moment of the electron spin. Through this effective magnetic field, which certainly depends on the orbital motion of the electron, the SOI is established. This physical picture holds in semiconductor too, when $V(\mathbf{r})$ could be the periodic potential of the host lattice and also the impurities.

The $\mathbf{k} \cdot \mathbf{p}$ model is often applied to the electron energy band calculation in semiconductor, when the states in the vicinity of the band edges. Furthermore, within the envelope function approximation (EFA), the energy band can be characterized by effective masses. The SOI in semiconductors requires, first of all, an effective electric field in the material. Such effective electric field can be contributed from the build-in crystal field where the crystal has bulk inversion asymmetric (BIA) the so-called Dresselhaus SOI, or structural inversion asymmetry (SIA), the so-called Rashba SOI. The BIA is found in zinc-blende structure and the SIA in asymmetric quantum wells (QWs) or heterostructures.

Based on the effective mass approximation, the effect of all the fast-varying atomic potential has been incorporated into the effective mass. Slower varying $V(\mathbf{r})$, with variation length scale much greater than the lattice spacing, is found to contribute to SOI with a much greater SO coupling constant λ . For a central potential $V(\mathbf{r}) = V(r)$ in vacuum, the SO coupling is

$$\frac{\hbar}{4m_0^2c^2} \boldsymbol{\sigma} \cdot (\nabla V \times \mathbf{p}) = \frac{\hbar}{4m_0^2c^2} \frac{1}{r} \frac{dV}{dr} \boldsymbol{\sigma} \cdot (\mathbf{r} \times \mathbf{p}) = \frac{\hbar^2}{4m_0^2c^2} \frac{1}{r} \frac{dV}{dr} \frac{\mathbf{L}}{\hbar} \cdot \boldsymbol{\sigma} = -\frac{\lambda_{\text{vac}}}{\hbar} \frac{1}{r} \frac{dV}{dr} \mathbf{L} \cdot \boldsymbol{\sigma},$$

where \mathbf{L} is the orbital angular momentum, $\boldsymbol{\sigma}$ is the vector Pauli matrices and $\lambda_{\text{vac}} = -\hbar^2/(4m_0^2c^2) \approx -3.72 \times 10^{-6} \text{ \AA}^2$.

But in a semiconductor, also for a central potential $V(\mathbf{r}) = V(r)$, the SO coupling is

$$H_{\text{SO}} = -\frac{\lambda}{\hbar} \frac{1}{r} \frac{dV}{dr} \mathbf{L} \cdot \boldsymbol{\sigma},$$

where

$$\lambda \approx \frac{P^2}{3} \left[\frac{1}{E_g^2} - \frac{1}{(E_g + \Delta_0)^2} \right].$$

For a 2DEG, the SOI becomes

$$H_{\text{SO}} = -\frac{\lambda}{\hbar} \frac{1}{\rho} \frac{dV(\rho)}{d\rho} L_z \sigma_z.$$

Here P is the momentum matrix element between s - and p -orbitals, E_g is the energy band gap, and Δ_0 represents the SOI energy split to the spin split-off hole band [3, 4]. Of particular interest is that $\lambda = 120 \text{ \AA}^2$ in InAs, which is seven order of magnitude greater than λ_{vac} [3, 5].

Qualitatively, this large enhancement of SO coupling constant can be explained in the following. With $\lambda_{\text{vac}} \propto \frac{1}{m_0^2 c^2} = \frac{1}{m_0} \frac{1}{m_0 c^2}$, we can see that

$$\frac{\lambda}{\lambda_{\text{vac}}} \sim \frac{m_0}{m^*} \frac{m_0 c^2}{E_g}.$$

For InAs, $m_0/m^* \sim \frac{1}{0.023}$; $\frac{m_0 c^2}{E_g} \sim \frac{0.5 \text{ MeV}}{0.418 \text{ eV}}$; leading to

$$\frac{\lambda}{\lambda_{\text{vac}}} \sim 52 \times 10^6.$$

Comparing with $\frac{120 \text{ \AA}^2}{3.73 \times 10^{-6} \text{ \AA}^2} = 32 \times 10^6$, such hand waving argument has captured the essential physical origin of the great enhancement.

1.1.2 Quantum Hall effect

The integer quantum Hall state (von Klitzing, Dorda, and Pepper, 1980; Prange and Girvin, 1987), occurs when free electrons are confined to two dimensions by applying a strong magnetic field. The quantization of the electrons circular orbits with cyclotron frequency ω_c leads to quantized Landau levels with energy $\varepsilon_m = \hbar\omega_c(m + 1/2)$. If N Landau levels are filled and the rest are empty, then an energy gap separates the occupied and empty states just as in an insulator. Unlike an insulator, though, an x-direction electric field causes the cyclotron orbits to drift, leading to a Hall current characterized by the quantized Hall conductivity,

$$\sigma_{xy} = Ne^2/h. \tag{1.2}$$

This precision is a manifestation of the topological nature of σ_{xy} . Landau levels can be viewed as a band structure. Since the generators of translations do not commute with one another in a magnetic field, electronic states cannot be labeled by momentum. However, if a unit cell with area $2\pi\hbar c/eB$ enclosing a flux quantum is defined, then lattice translations restore the commutation relation, so Bloch's theorem allows electron states to be labeled by 2D crystal momentum \mathbf{k} . In the absence of a periodic potential, the energy levels are simply the \mathbf{k} independent of Landau levels $E_m(\mathbf{k}) = \varepsilon_m$. In the presence of a lattice periodic potential, the energy levels will disperse with \mathbf{k} . This leads to a band structure that looks identical to that of an ordinary insulator.

1.1.3 Quantum spin Hall effect

The quantum spin Hall state is a state of matter proposed to exist in special, two-dimensional, semiconductors with spin-orbit coupling. The quantum spin Hall state of matter is the cousin of the integer quantum Hall state, but, unlike the latter, it does not require the application of a large magnetic field. The quantum spin Hall state does not break any discrete symmetries (such as time-reversal or parity symmetry). The first

proposal for the existence of a quantum spin Hall state was developed by Kane and Mele [6] who adapted an earlier model for graphene by Haldane [7] which exhibits an integer quantum Hall effect. The Kane and Mele model is two copies of the Haldane model such that the spin up electron exhibits a chiral integer quantum Hall Effect while the spin down electron exhibits an anti-chiral integer quantum Hall effect. It has been recently proposed [8] and subsequently experimentally realized [9] in mercury (II) telluride (HgTe) semiconductors.

Overall the Kane-Mele model has a charge-Hall conductance of exactly zero but a spin-Hall conductance of exactly $\sigma_{xy}^{spin} = (\text{in units of } \frac{e}{4\pi})$. Independently, a quantum spin Hall model was proposed by Bernevig and Zhang [10] in an intricate strain architecture which engineers, due to spin-orbit coupling, a magnetic field pointing upwards for spin-up electrons and a magnetic field pointing downwards for spin-down electrons. The main ingredient is the existence of spin-orbit coupling, which can be understood as a momentum-dependent magnetic field coupling to the spin of the electron.

Strictly speaking, the models with spin-orbit coupling do not have a quantized spin Hall conductance $\sigma_{xy}^{spin} \neq 2$. Those models are more properly referred as topological insulator which is an example of topologically ordered states.

1.2 Motivation

A material "garphene" which has six pairs Dirac points at each corners of Brillouin zone (show in Fig. 1.2). The electrical properties of graphene can be described by a conventional tight-binding model, and the eigenvalues are given by

$$\begin{vmatrix} -E & -\gamma f_1(\mathbf{k}) \\ -\gamma f_1^*(\mathbf{k}) & -E \end{vmatrix} = E^2 - \gamma^2 |f_1(\mathbf{k})|^2 = 0, \quad (1.3)$$

so that the eigenvalues are given by $E(\mathbf{k}) = \pm\gamma |f_1(\mathbf{k})|$. $E(\mathbf{k})$ that $|f_1(\mathbf{k})| = 0$ for some \mathbf{k} leading to a gapless energy band. $|f_1(\mathbf{k})|^2$ is given by $|f_1(\mathbf{k})|^2 = 1 + 4 \cos^2(k_y \frac{a_0}{2}) + 4 \cos(k_y \frac{a_0}{2}) \cos(k_x \frac{\sqrt{3}a_0}{2})$ [1].

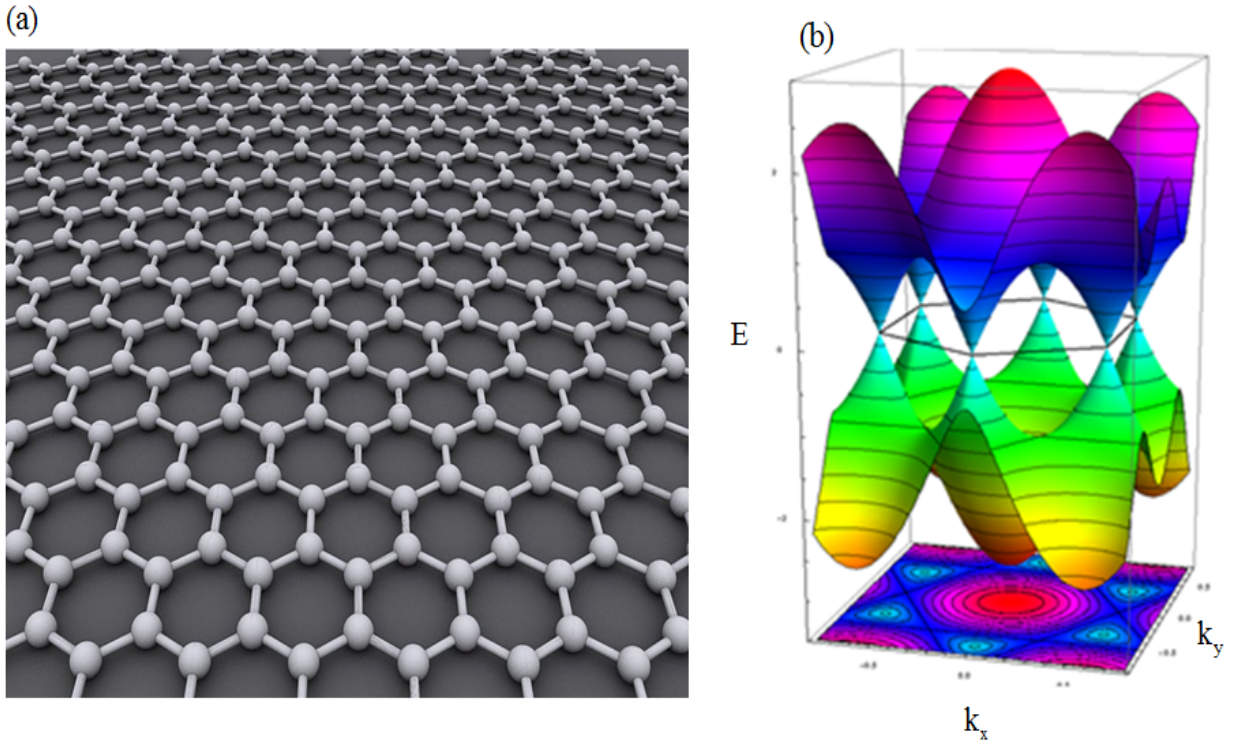


Figure 1.1: The graphene structure (hexagon lattice) in (a) and the energy dispersion which have Dirac cones in (b). Ref: <http://en.wikipedia.org/wiki/Graphene>.

This Dirac physics of graphene has been in widespread discussed, because the Dirac

physics often exist in high energy physics system but in graphene can be found in Solid-state physics.

Marco Gibertini, Achintya Singha, Vittorio Pellegrini, and Marco Polini, have provided an artificial graphene-like system and discuss an experimental realization [11] in a modulation-doped (the model shows in Fig. 1.2(a)) GaAs quantum well (see Fig. 1.2(b)) and the numerical results (shown in Fig. 1.3), which Dirac cones exist at K points .

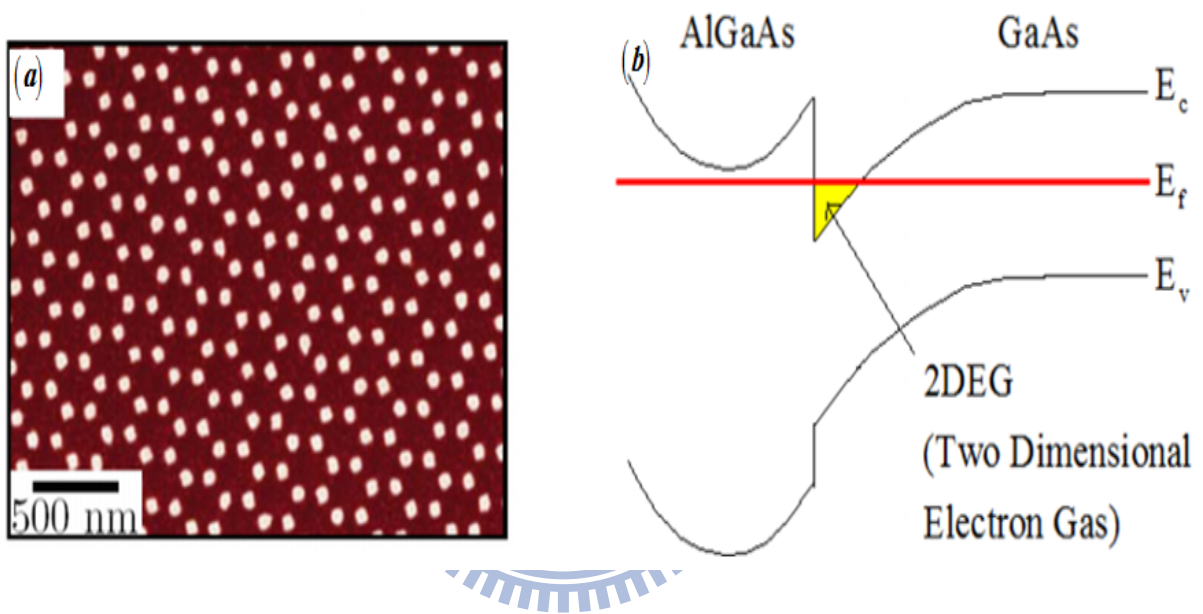


Figure 1.2: (a) Scanning electron microscopy images of the nano-patterned modulation-doped GaAs/AlGaAs sample. [11]. (b) The conduction bands and valence bands of each AlGaAs and GaAs produce the states interaction making 2DEG.

Recently, a theoretical work [12] was proposed by Cheol-Hwan Park and Steven G. Louie* which is an ordinary two-dimensional electron gas (2DEG) under an appropriate external muffin-tin potential (MTP) as shown in Fig. 1.4 reveals that massless Dirac fermions are generated near the corners of the supercell Brillouin zone (see Fig. 1.5). They provide detailed theoretical estimates to realize such artificial graphene-like system.

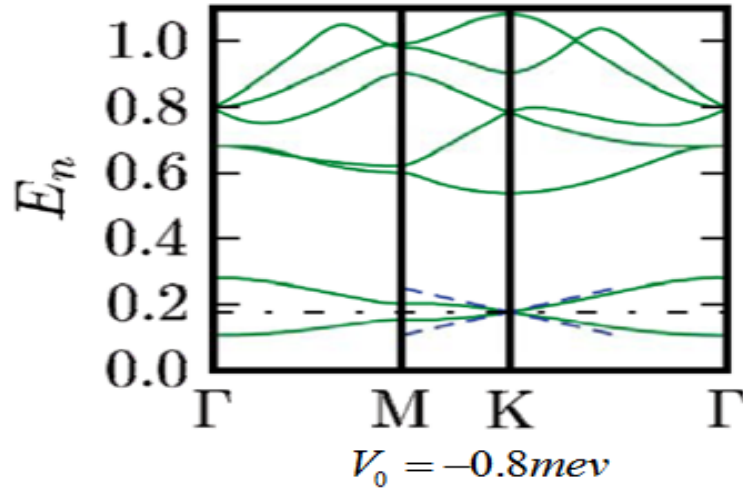


Figure 1.3: The energy dispersion of MTP (hexagonal lattice). [11].

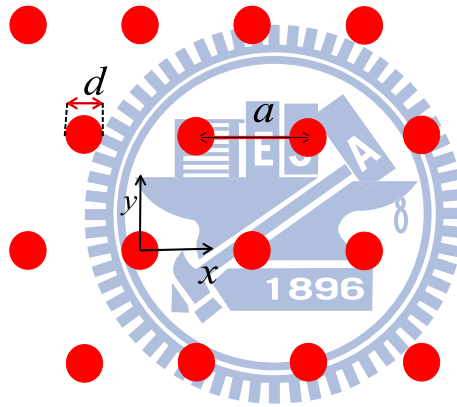


Figure 1.4: A muffin-tin type with a center to center distance a . The potential is U_0 inside the disk with diameter d and zero outside.

In this thesis, we start from the model which was proposed by Cheol-Hwan Park and Steven G. Louie*, and further consider the effect of spin-orbit coupling (SOI) (which comes from the in-plane potential gradient) due to muffin-tin potential (MTP) lattice. We expect the SOI can open up gaps at Dirac points. And new class of topological states has emerged recently, namely quantum spin Hall (QSH) states, which occur in the gap between bulk state. So we discuss whether QSH is provided by topological invariant in our systems.

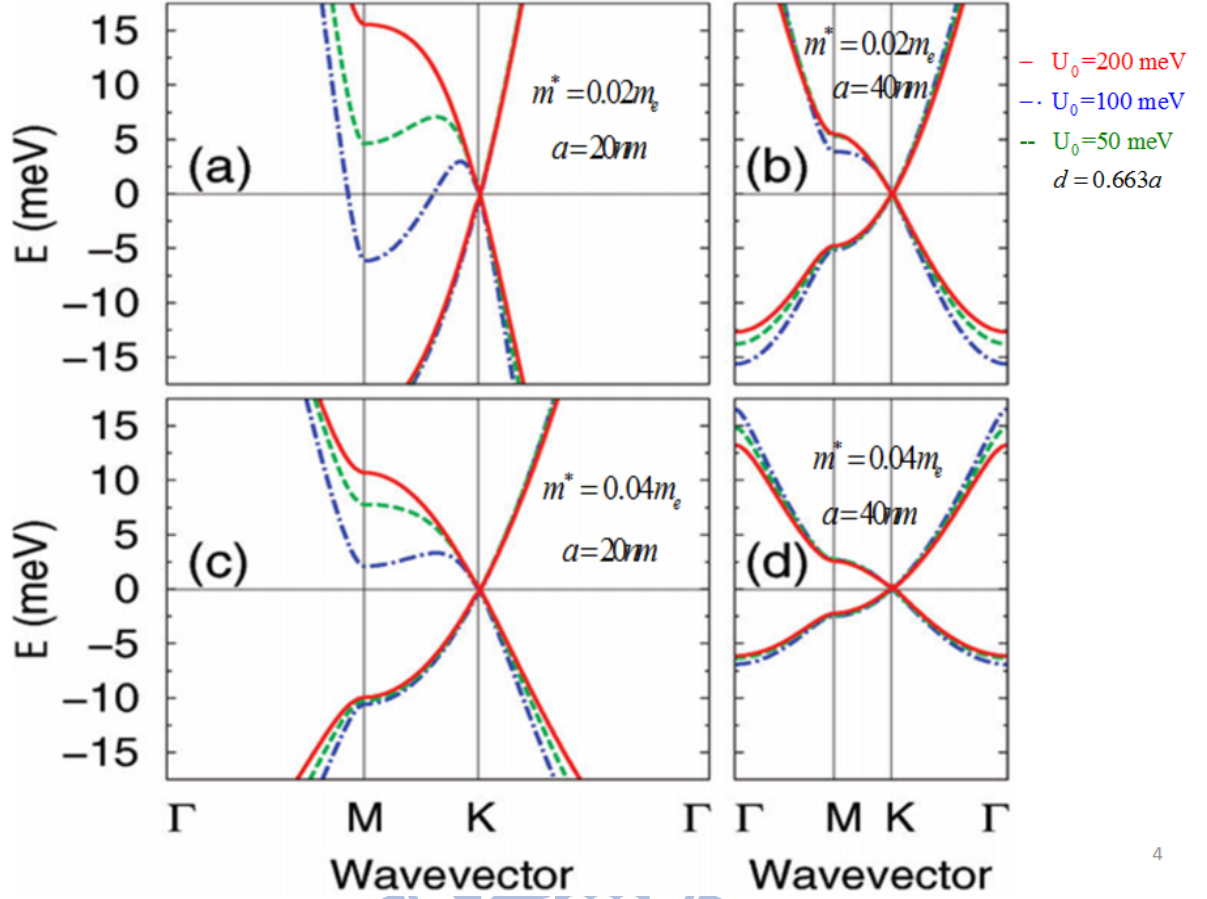


Figure 1.5: The lowest two energy bands dispersion of a hexagonal 2DEG superlattice.

1.3 A guiding tour to this thesis

In Chapter 2, we study the system about 2DEG under an appropriate external periodic potential. In Chapter 3, we consider the effect of spin-orbital coupling in our system and discuss the numerical result. In Chapter 4, we introduce the numerical calculations of Berry curvature. The numerical results for each bands would be showed and discuss it. In Chapter 5, we introduce and calculate the Chern number and Z_2 number which are topological invariant. Those can help us to expect the edge states and the quantum spin Hall states for bulk system. In Chapter 6 present our conclusion and possible future work.

Chapter 2

Energy band structure without SOI effect

In this chapter we demonstrate a work about energy band engineering by the artificial pattern mechanism to achieve the graphene-like band structure. An ordinary two-dimensional electron gas (2DEG) under an appropriate external periodic potential (muffin-tin type array) reveals that massless Dirac fermions are generated near the corners of the supercell Brillouin zone.

2.1 Energy band structure for a muffin-tin potential lattice in 2DEG

The Hamiltonian for a 2D muffin-tin type (triangular lattice) potential $V(\mathbf{r})$ can be expressed by

$$H = -\frac{\hbar^2}{2m^*}\nabla^2 + V(\mathbf{r}), \quad (2.1)$$

where m^* is the effective electron mass. The Bloch wave function for this muff-tin potential (MTP) lattice can be described by

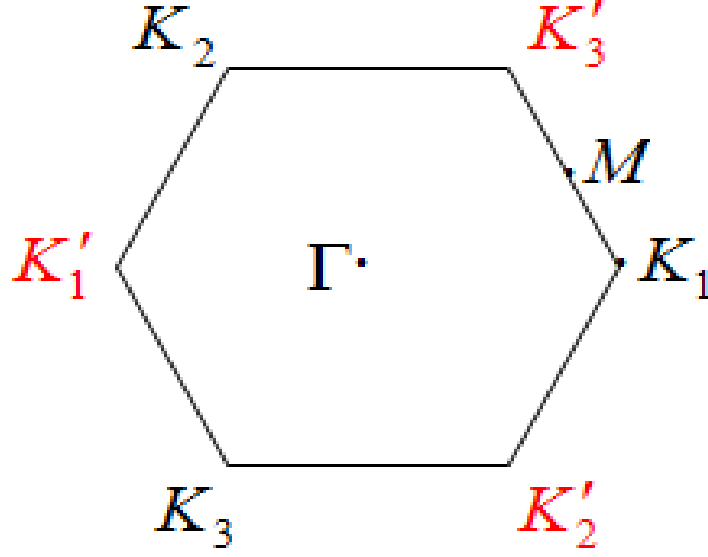


Figure 2.1: The Brillouin zone of hexagonal lattice.

Defined the wave function and periodic potential as bellow:

$$\Psi_{\boldsymbol{\kappa}}(\mathbf{r}) = \frac{1}{\sqrt{N \cdot A_{\text{unit cell}}}} e^{i\boldsymbol{\kappa} \cdot \mathbf{r}} \sum_n e^{i\mathbf{G}_n \cdot \mathbf{r}} c_n. \quad (2.2)$$

The wave function can be approximately expressed as a linear combination of many (n) plane-wave states, where N is the number of unit cell; $A_{\text{unit cell}}$ is the area of unit cell in real space; $\boldsymbol{\kappa} = \mathbf{K}_1 + \mathbf{k}$ the small $\boldsymbol{\kappa}$ was expanded from \mathbf{K}_1 (Fig. 2.1). The form of external potential is showed below:

$$V(\mathbf{r}) = \sum_m e^{i\mathbf{G}_m \cdot \mathbf{r}} V'_m, \quad (2.3)$$

where \mathbf{G}_m is the vector of each K point in \mathbf{k} space (there are showed in appendixA about how to label m); $V'_m = \frac{2\pi U_0 d}{\sqrt{3} G_m a_1 a_2} J_1\left(\frac{G_m d}{2}\right)$ (U_0 is external potential energy, and the explicit form is derived in appendixB) is the interaction coefficient for each localized component \mathbf{G}_m potential ; m is the labels K point.

We substitute this wave function $\Psi(\mathbf{r})$ and MTP $V(\mathbf{r})$ to Schrödinger equation $H\Psi =$

$E\Psi$, given by

$$\begin{aligned}
 & \sum_n e^{i\mathbf{k}\cdot\mathbf{r}} e^{i(\mathbf{G}_n+\mathbf{K}_1)\cdot\mathbf{r}} \left[\frac{\hbar^2}{2m^*} (\mathbf{k}^2 + 2\mathbf{k}\cdot(\mathbf{G}_n + \mathbf{K}_1) + (\mathbf{G}_n + \mathbf{K}_1)^2) \right] c_n \\
 & + \sum_{mn} e^{i\mathbf{k}\cdot\mathbf{r}} e^{i[\mathbf{K}_1+(\mathbf{G}_n+\mathbf{G}_m)]\cdot\mathbf{r}} V'_m c_n \\
 & = E \sum_n e^{i\mathbf{k}\cdot\mathbf{r}} e^{i(\mathbf{G}_n+\mathbf{K}_1)\cdot\mathbf{r}} c_n,
 \end{aligned} \tag{2.4}$$

where $\sum_{n,m} e^{i(\mathbf{G}_m+\mathbf{G}_n)\cdot\mathbf{r}} V'_m c_n = \sum_{n',m} e^{i\mathbf{G}_{n'}\cdot\mathbf{r}} V'_m c_{n'-m} = \sum_{n,m} e^{i\mathbf{G}_n\cdot\mathbf{r}} V'_m c_{n-m} = \sum_{n,m'} e^{i\mathbf{G}_n\cdot\mathbf{r}} V'_{n-m'} c_{m'}$, then $m' = m$, and we confined the same spatial factor $e^{i\mathbf{k}\cdot\mathbf{r}} e^{i(\mathbf{G}_n+\mathbf{K}_1)\cdot\mathbf{r}}$ on both side and the orthogonality gives us

$$\sum_{nm} \left[\frac{\hbar^2}{2m^*} (\mathbf{k}^2 + 2\mathbf{k}\cdot(\mathbf{G}_n + \mathbf{K}_1) + (\mathbf{G}_n + \mathbf{K}_1)^2) \delta_{mn} + V'_{n-m} \right] c_m = E \sum_{nm} c_m \delta_{mn}, \tag{2.5}$$

where V'_{n-m} is the interaction coefficient for MTP; the n, m label \mathbf{K} points in \mathbf{k} -space and we assume $\sum_{nm} \left[\frac{\hbar^2}{2m^*} (\mathbf{k}^2 + 2\mathbf{k}\cdot(\mathbf{G}_n + \mathbf{K}_1) + (\mathbf{G}_n + \mathbf{K}_1)^2) \delta_{mn} + V'_{n-m} \right] = M_{nm}$. This equation is cast into a matrix form for numerical calculation (see Eq. (2.6)),

$$\frac{\hbar^2 K_0^2}{2m^*} \begin{bmatrix} \tilde{M}_{nm} \end{bmatrix} \begin{bmatrix} c_m \end{bmatrix} = \frac{\hbar^2 K_0^2}{2m^*} \varepsilon_m \begin{bmatrix} c_m \end{bmatrix}, \tag{2.6}$$

where the dimensionless parameters are $M_{nm} = \frac{\hbar^2 K_0^2}{2m} \tilde{M}_{nm}$, $\mathbf{k} = K_0 \boldsymbol{\kappa}$, $K_1 = K_0 K'_1$, $\mathbf{G}_n = K_0 \mathbf{G}'$, $E = \frac{\hbar^2 K_0^2}{2m} \varepsilon$, $U_0 = \frac{\hbar^2 K_0^2}{2m} u_0$, $V'_{n-m} = \frac{\hbar^2 K_0^2}{2m} \tilde{V}'_{n-m}$. With this numerical matrix formulation as shown as Eq. (2.5) and Eq. (2.6), we can obtain the numerical result.

There are the numerical result of energy distribution in MTP lattice (Fig. 2.2), we can see the Dirac point at K point, this phenomenon confirm with the results proposed by Cheol-Hwan Park and Steven G. Louie* [12].

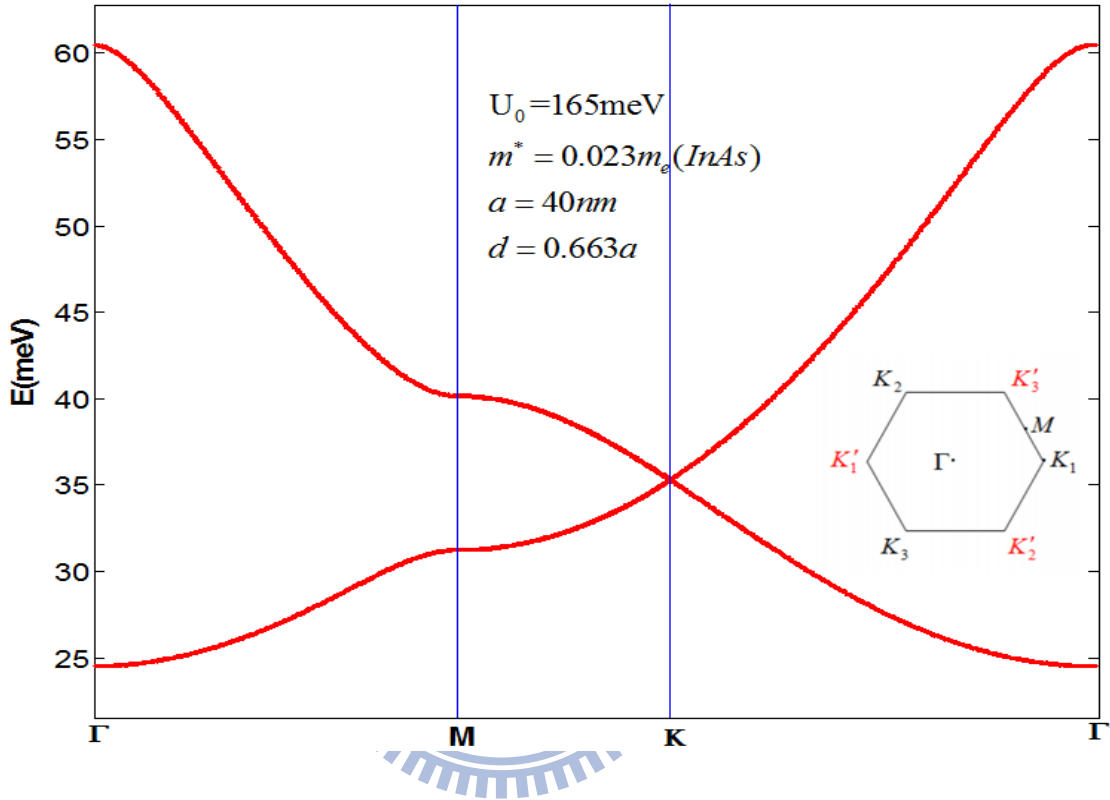


Figure 2.2: The lowest two energy bands calculation of a hexagonal 2DEG superlattice . The Dirac point energy which is at the crossing of the two bands.

And the Fig. 2.3 shows the results of our rework which are a periodic structure (for wide area in k-space can obviously discover it) and we can see the Dirac points at each corners of Brillouin zone. And the results for other higher energy bands dispersion are showed in appendixC.

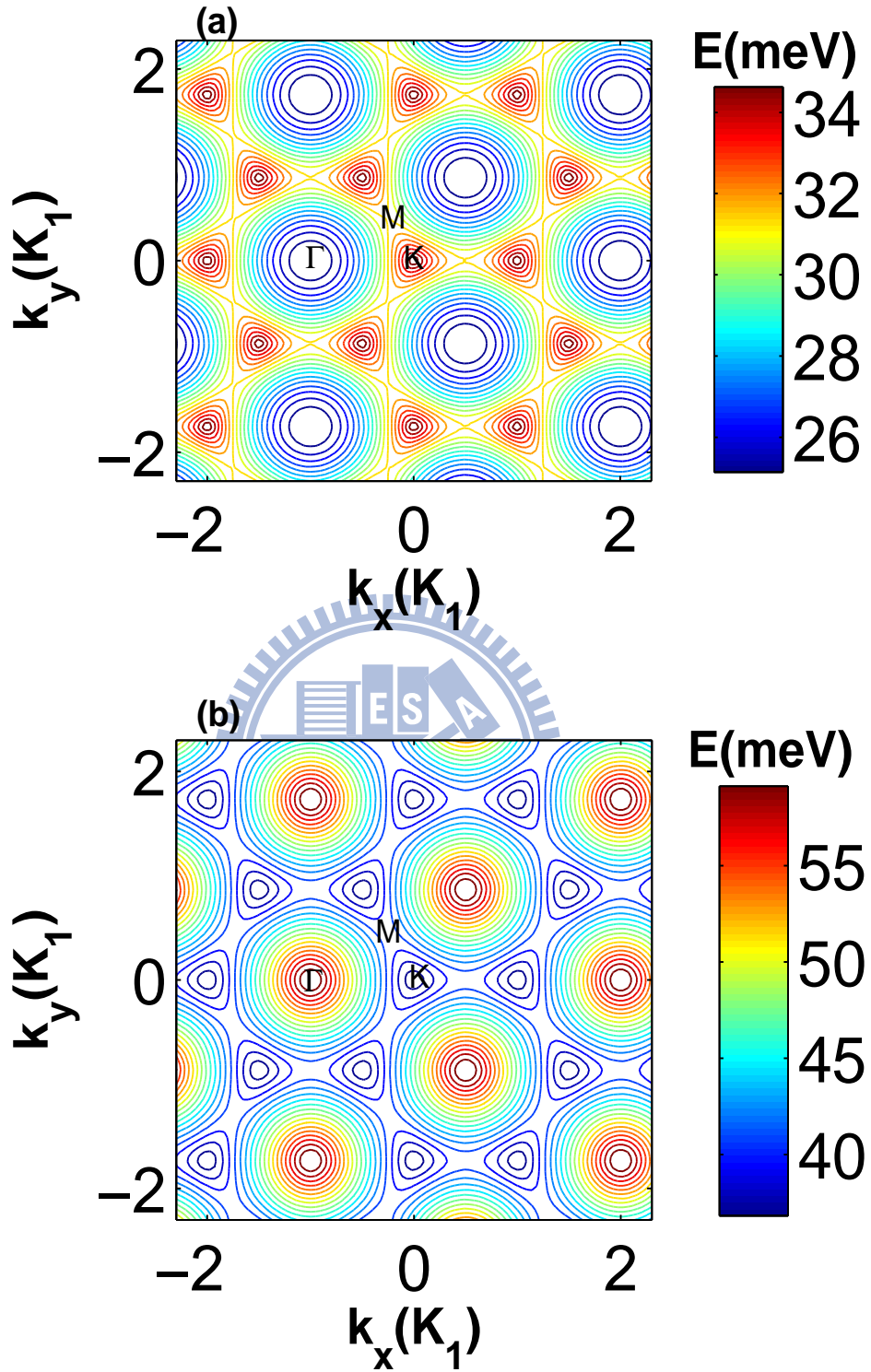


Figure 2.3: The contour of energy dispersion for (a) the first lowest band, (b) the second lowest band which $m^* = 0.023m_e$, $a=40\text{nm}$, $d=0.663a$ and $U_0=165\text{ meV}$.

2.1.1 The Analytical result by perturbation method

The wave function $\Psi_{\kappa}(\mathbf{r})$ can be approximately expressed as a linear superposition (as show asEq. (2.2)) of three plane-wave states. The reason for choosing this three basis ($\mathbf{K}_1, \mathbf{K}_2, \mathbf{K}_3$) is that they are same energy and connected by the most simple reciprocal vectors $\mathbf{G}_1, \mathbf{G}_2$ and \mathbf{G}_3 (shown in Fig. 2.4),

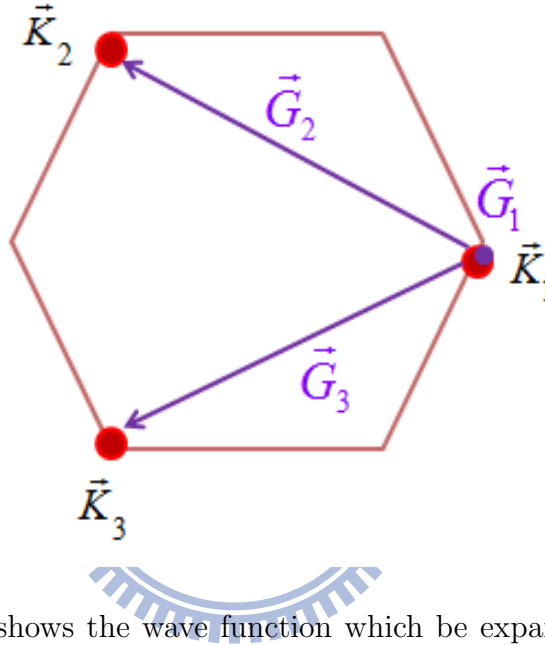


Figure 2.4: This figure shows the wave function which be expanded to $\mathbf{K}_1, \mathbf{K}_2, \mathbf{K}_3$ by \mathbf{G}_m .


$$\Psi_{\kappa}(\mathbf{r}) = \frac{1}{\sqrt{3A_c}} [c_1 \exp(i(\mathbf{K}_1 + \mathbf{k}) \cdot \mathbf{r}) + c_2 \exp(i(\mathbf{K}_2 + \mathbf{k}) \cdot \mathbf{r}) + c_3 \exp(i(\mathbf{K}_3 + \mathbf{k}) \cdot \mathbf{r})], \quad (2.7)$$

where $\frac{1}{\sqrt{3A_c}}$ is the normalized coefficient of the wave function and $\mathbf{K}_1, \mathbf{K}_2,$ and \mathbf{K}_3 represent wavevectors at the supercell Brillouin zone corners 1, 2, and 3, respectively, in Fig. 2.4. Because of the Schrödinger equation $H\Psi = E\Psi$ and Eq. (3.1), we can obtain those equations as bellow:

$$\begin{aligned}
 e^{i(\mathbf{K}_1+\mathbf{k})\cdot\mathbf{r}} \left\{ c_1 \left[\frac{\hbar^2}{2m^*}(\mathbf{k} + \mathbf{K}_1 + \mathbf{G}_1)^2 + V'_{1-1} \right] + c_2 V'_{1-2} + c_3 V'_{1-3} \right\} &= e^{i(\mathbf{K}_1+\mathbf{k})\cdot\mathbf{r}} E_1 c_1 \\
 e^{i(\mathbf{K}_2+\mathbf{k})\cdot\mathbf{r}} \left\{ c_1 V'_{2-1} + c_2 \left[\frac{\hbar^2}{2m^*}(\mathbf{k} + \mathbf{K}_1 + \mathbf{G}_2)^2 + V'_{2-2} \right] + c_3 V'_{2-3} \right\} &= e^{i(\mathbf{K}_2+\mathbf{k})\cdot\mathbf{r}} E_2 c_2 , \\
 e^{i(\mathbf{K}_3+\mathbf{k})\cdot\mathbf{r}} \left\{ c_1 V'_{3-1} + c_2 V'_{3-2} + c_3 \left[\frac{\hbar^2}{2m^*}(\mathbf{k} + \mathbf{K}_1 + \mathbf{G}_3)^2 + V'_{3-3} \right] \right\} &= e^{i(\mathbf{K}_3+\mathbf{k})\cdot\mathbf{r}} E_3 c_3
 \end{aligned} \tag{2.8}$$

where $\mathbf{K}_1 + \mathbf{G}_1 = \mathbf{K}_1$, $\mathbf{K}_1 + \mathbf{G}_2 = \mathbf{K}_2$, $\mathbf{K}_1 + \mathbf{G}_3 = \mathbf{K}_3$.

Equivalently, we could express the eigenstate as a three-component column vector $\mathbf{c} = (c_1, c_2, c_3)^T$. Within this basis, the Hamiltonian H (which ignore the \mathbf{k}^2 term, because the secondly contribution can be ignored), will give us

$$\frac{\hbar^2 K^2}{2m^*} \begin{pmatrix} 1 & 0 & 0 \\ 0 & 1 & 0 \\ 0 & 0 & 1 \end{pmatrix} + H_0 + H_1,$$


$$H_0 = W \begin{pmatrix} 0 & 1 & 1 \\ 1 & 0 & 1 \\ 1 & 1 & 0 \end{pmatrix}, \tag{2.9}$$

, where $V'_{n-m} = V'_{1-2} = V'_{2-1} = V'_{1-3} = V'_{3-1} = V'_{2-3} = V'_{3-2} = W$; $V'_{1-1} = V'_{2-2} = V'_{3-3} = 0$ ($V'_m = \frac{2\pi U_0 d}{\sqrt{3} G_m a_1 a_2} J_1(\frac{G_m d}{2})$) and

$$H_1 = \hbar v_0 k \begin{pmatrix} \cos \theta_{\mathbf{k}} & 0 & 0 \\ 0 & \cos(\theta_{\mathbf{k}} - \frac{2\pi}{3}) & 0 \\ 0 & 0 & \cos(\theta_{\mathbf{k}} - \frac{4\pi}{3}) \end{pmatrix}, \tag{2.10}$$

where $\frac{\hbar^2}{m}(\mathbf{k} \cdot \mathbf{K}_i) = v_0 \hbar k \cos \theta_{\mathbf{k}}$, v_0 is the group velocity and $\theta_{\mathbf{k}}$ is the polar angle of the

wavevector \mathbf{k} from the $+\mathbf{x}$ direction. The eigenvalues of the unperturbed Hamiltonian H_0 are given by $E_0 = -W, -W, 2W$. These two degenerated eigenvectors of H_0 with the same eigenvalue $-W$.

$$|c_1\rangle = \frac{1}{\sqrt{2}} \begin{pmatrix} 0 \\ 1 \\ -1 \end{pmatrix}, \quad (2.11)$$

$$|c_2\rangle = \frac{1}{\sqrt{6}} \begin{pmatrix} 2 \\ -1 \\ -1 \end{pmatrix}. \quad (2.12)$$

Thus H_1 can be treated as a perturbation, which is approximate for $\hbar v_0 k < W$ and restricted to the sub-Hilbert space spanned by the two vectors is represented by a 2×2 matrix \tilde{H}_1 (degenerate perturbation theory).

$$\tilde{H}_1 = \begin{pmatrix} \langle c_1 | H_1 | c_1 \rangle & \langle c_1 | H_1 | c_2 \rangle \\ \langle c_2 | H_1 | c_1 \rangle & \langle c_2 | H_1 | c_2 \rangle \end{pmatrix} = \hbar \frac{v_0}{2} \begin{pmatrix} -k_x & -k_y \\ -k_y & k_x \end{pmatrix}. \quad (2.13)$$

The eigenenergies of \tilde{H}_1 are given by

$$E(\mathbf{k}) = \pm \frac{\hbar v_0}{2} k. \quad (2.14)$$

Therefore we can see at $\mathbf{k}=0$, there are degenerate eigenstates and the group velocity near \mathbf{K} ($\mathbf{k} \approx 0$) shows the linear behavior comparing with Fig. 2.2.

2.2 The numerical result compare with single well system

We use the same program to calculate the case of $U_0 = -300 \text{ meV}$. When the extra potential is negative, the MTP are consisted of many single wells. Such wave under MTP can be illustrated by the overlapping wave function of the nearest single wells.

Schrödinger equation in cylinder coordinates, can be written by

$$\left\{ -\frac{\hbar^2}{2m^*} \left[\frac{1}{r} \frac{d}{dr} \left(r \frac{d}{dr} \right) + \frac{1}{r^2} \frac{d}{d\phi^2} \right] + V(r) \right\} \Psi(r, \phi) = E \Psi(r, \phi). \quad (2.15)$$

Applying the factored form $\Psi(r, \phi) = R(r)\Phi(\phi)$, where $R(r)$ is the radial part, and ϕ is the angle between \mathbf{r} and \hat{x} , one can obtain

$$\frac{A}{R(r)} \frac{d}{dr} \left(r \frac{dR(r)}{dr} \right) - r^2 (V(r) - E) = -A \frac{d^2 \Phi(\phi)}{\Phi(\phi) d\phi^2}. \quad (2.16)$$

This Schrödinger can be decoupled into the radial and azimuthal parts,

$$\begin{aligned} \frac{d^2 R(r)}{dr^2} + \frac{1}{r} \frac{dR(r)}{dr} + \left[\frac{(V(r) - E)}{-A} - \frac{l^2}{r^2} \right] R(r) &= 0, \\ \frac{d^2 \Phi(\phi)}{d\phi^2} &= -l^2 \Phi(\phi), \end{aligned} \quad (2.17)$$

where we assume $A = \frac{\hbar^2}{2m^*}$, and the disk-shaped potential $V(r) = -V_0 \theta(\frac{d}{2} - r)$, $V_0 > 0$ is external potential strength; d is the diameter of potential region.

The solution of radial equation is the Bessel equation. Therefore the electron wave function in two dimensions can be written in form

$$\Psi_l(r, \phi) = \begin{cases} C_l J_l(\alpha r) e^{il\phi} & r \leq \frac{d}{2}, \\ E_l K_l(\beta r) e^{il\phi} & r \geq \frac{d}{2}, \end{cases}$$

where $\alpha = \sqrt{\frac{V_0 + E}{A}}$; $\beta = \sqrt{\frac{|E|}{A}}$. The wave function is continuous at the boundary

$r = \frac{d}{2}$, therefore we can get the energy level of finite single well. The Fig. 2.5 shows (a) MTP case and (b) single well case, where the l is the orbital quantum number, the $l=0$ is single state; $|l|=1$ includes two state. Although the single well energy band structure is not exactly as same as muffin-tin potential, the band energy level agrees quite well with each other.

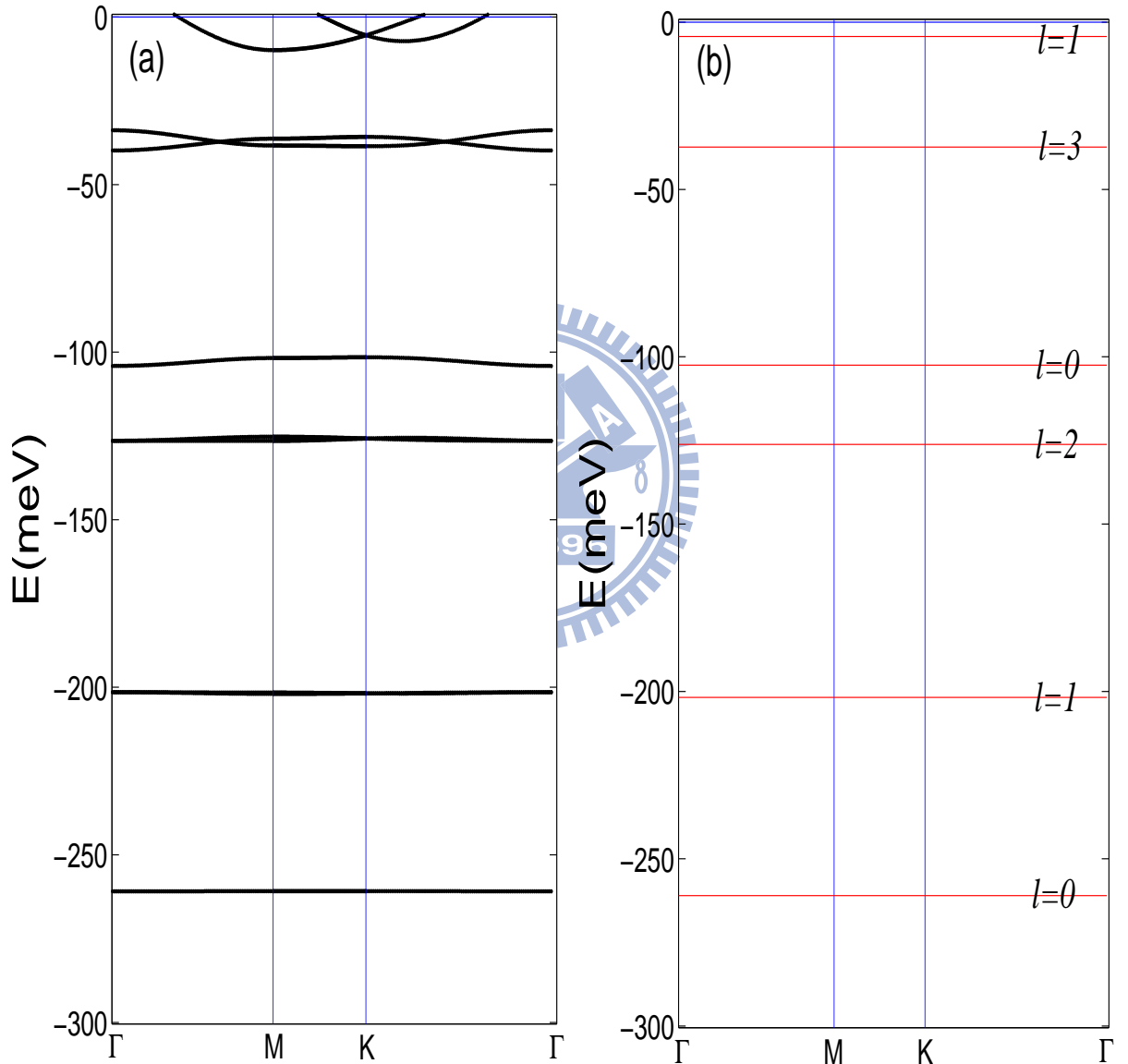


Figure 2.5: The energy band structure for (a) the numerical MTP in 2DEG system. Compared the energy level with (b) the single well in 2DEG system. $U_0 = -300\text{meV}$, $a = 40\text{nm}$; $d=0.663a$.

2.3 Brief summary

In this chapter, we show that the energy band structures excluding SOI effect in external periodic potential in 2DEG. There are massless Dirac points at the corners of Brillouin zone (K_1 points) as graphene system.

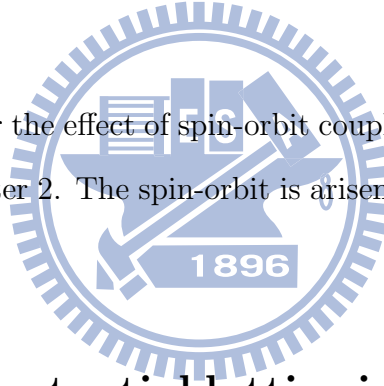
And we also do another work for inspecting the numerical results. The wave function be expanded from Γ point and compare the numerical energy dispersion with the results which the wave function be expanded from K_1 . The result for comparison is exactly the same.



Chapter 3

Energy band structure with SOI effect

In this chapter, we consider the effect of spin-orbit coupling on the energy band structure, we have discussed in Chapter 2. The spin-orbit is arisen from the in-plane gradient of the periodic potential.



3.1 Muffin-tin potential lattice in the presence of SOI

The Hamiltonian H for a 2D MTP system with spin-orbital interaction can be expressed by.

$$H = \frac{\mathbf{p}^2}{2m^*} + V(\mathbf{r}) + H_{SO}. \quad (3.1)$$

The spin-orbit interaction term, in vacuum can be desired by

$$H_{SO} = \frac{e\lambda}{\hbar} \boldsymbol{\sigma} \cdot (\mathbf{p} \times \mathbf{E}) = -\frac{e\lambda}{\hbar} \boldsymbol{\sigma} \cdot (\mathbf{p} \times \nabla U) = \frac{\lambda}{\hbar} \boldsymbol{\sigma} \cdot (\mathbf{p} \times \nabla V) = -\frac{\lambda}{\hbar} \boldsymbol{\sigma} \cdot (\nabla V \times \mathbf{p}), \quad (3.2)$$

where in-plane electric field $\mathbf{E} = -\nabla U$ (U : electric potential); V (Electric potential energy) = $-eU$ ($e > 0$); spin-orbit coupling constant $\lambda=120\text{\AA}^2$ (for InAs)

The wave function includes both spin-up and spin-down component in column vector form:

$$\Psi_{\boldsymbol{\kappa}}(\mathbf{r}) = e^{i\boldsymbol{\kappa}\cdot\mathbf{r}} \sum_n e^{i\mathbf{G}_n\cdot\mathbf{r}} \begin{bmatrix} c_{n\uparrow} \\ c_{n\downarrow} \end{bmatrix}. \quad (3.3)$$

The Hamiltonian of SOI term operates on the wave function leading to:

$$\begin{aligned} H_{SO}\Psi(\mathbf{r}) &= -\frac{i\lambda}{\hbar} \sum_m e^{i\mathbf{G}_m\cdot\mathbf{r}} V'_m \boldsymbol{\sigma} \cdot (\mathbf{G}_m \times \mathbf{p}) \sum_n e^{i(\mathbf{G}_n+\boldsymbol{\kappa})\cdot\mathbf{r}} \begin{bmatrix} c_{n\uparrow} \\ c_{n\downarrow} \end{bmatrix} \\ &= -\frac{i\lambda}{\hbar} \begin{bmatrix} \sum_m e^{i\mathbf{G}_m\cdot\mathbf{r}} V'_m (\mathbf{G}_m \times \mathbf{p})_z & 0 \\ 0 & -\sum_m e^{i\mathbf{G}_m\cdot\mathbf{r}} V'_m (\mathbf{G}_m \times \mathbf{p})_z \end{bmatrix} \begin{bmatrix} \sum_n e^{i(\mathbf{G}_n+\boldsymbol{\kappa})\cdot\mathbf{r}} c_{n\uparrow} \\ \sum_n e^{i(\mathbf{G}_n+\boldsymbol{\kappa})\cdot\mathbf{r}} c_{n\downarrow} \end{bmatrix} \\ &= -i\lambda \sum_{mn} e^{i[\mathbf{G}_m+(\mathbf{G}_n+\boldsymbol{\kappa})]\cdot\mathbf{r}} \begin{bmatrix} c_{n\uparrow} V'_m (\mathbf{G}_m \times (\mathbf{G}_n + \boldsymbol{\kappa}))_z \\ -c_{n\downarrow} V'_m (\mathbf{G}_m \times (\mathbf{G}_n + \boldsymbol{\kappa}))_z \end{bmatrix}, \end{aligned} \quad (3.4)$$

where $\mathbf{G}_m \times \mathbf{p}$ is along z-direction, so $\boldsymbol{\sigma} \cdot \hat{z} = \sigma_z$ and $\sum_{n,m} e^{i(\mathbf{G}_m+\mathbf{G}_n)\cdot\mathbf{r}} V'_m c_n = \sum_{n',m} e^{i\mathbf{G}_{n'}\cdot\mathbf{r}} V'_m c_{n'-m} = \sum_{n,m} e^{i\mathbf{G}_n\cdot\mathbf{r}} V'_m c_{n-m} = \sum_{n,m'} e^{i\mathbf{G}_n\cdot\mathbf{r}} V'_{n-m'} c_{m'} (m' = m)$. The matrix here is diagonal, showing that spin-up and spin-down are decoupled because H_{SO} depends only on σ_z . Due to Eq. (3.1), and Schrödinger equation $H\Psi(\mathbf{r}) = E\Psi(\mathbf{r})$, and the orthogonal term of plane-wave form $e^{i\mathbf{k}\cdot\mathbf{r}} e^{i(\mathbf{K}_1+\mathbf{G}_n)\cdot\mathbf{r}}$ can be a substrate the m'th component to form a matrix equation. For getting the simple numerical formulation, we take off $e^{i\mathbf{k}\cdot\mathbf{r}} e^{i(\mathbf{K}_1+\mathbf{G}_n)\cdot\mathbf{r}}$ and obtain:

$$\begin{aligned}
 & \frac{\hbar^2}{2m^*} \sum_n \begin{bmatrix} k^2 + 2\mathbf{k} \cdot (\mathbf{G}_n + \mathbf{K}_1) + (\mathbf{G}_n + \mathbf{K}_1)^2 & 0 \\ 0 & k^2 + 2\mathbf{k} \cdot (\mathbf{G}_n + \mathbf{K}_1) + (\mathbf{G}_n + \mathbf{K}_1)^2 \end{bmatrix} \begin{bmatrix} c_{n\uparrow} \\ c_{n\downarrow} \end{bmatrix} + \\
 & \sum_{mn} V'_{n-m} \begin{bmatrix} 1 - i\lambda [\mathbf{G}_{n-m} \times (\mathbf{G}_m + \boldsymbol{\kappa})] & 0 \\ 0 & 1 + i\lambda [\mathbf{G}_{n-m} \times (\mathbf{G}_m + \boldsymbol{\kappa})] \end{bmatrix} \begin{bmatrix} c_{m\uparrow} \\ c_{m\downarrow} \end{bmatrix} \\
 & = \sum_n \begin{bmatrix} E_{c_{n\uparrow}} \\ E_{c_{n\downarrow}} \end{bmatrix}.
 \end{aligned} \tag{3.5}$$

This equation shows that the spin-up $c_{n\uparrow}$ part is decoupled with spin-down $c_{n\downarrow}$ (the element only exist on diagonal term). The numerical result is shown on the subsection 3.4.

The Fig. 3.5 shows the lowest two bands with wave vector near K_1 . We can see that the original Dirac point opens up a gap in the presence of SOI and the numerical result shows $E_{c_{n\uparrow}} = E_{c_{n\downarrow}}$.

3.1.1 The Analytical result in the presence of SOI by perturbation method

The subsection will show the analytical calculation in our system in the presence of SOI. The Schrödinger equation for a 2DEG in the presence of SOI, using the Eq. (3.1) and Eq. (3.2) (where we defined $H_{SO} = h_{SO}\sigma_z$, because of $\nabla V \times \mathbf{p}$ is along z direction) can be written in the following form

$$\begin{aligned}
 H\Psi_{\boldsymbol{\kappa}}(\mathbf{r}) & = \left\{ \left[\frac{\mathbf{p}^2}{2m^*} + V(\mathbf{r}) \right] \begin{pmatrix} 1 & 0 \\ 0 & 1 \end{pmatrix} + h_{SO} \begin{pmatrix} 1 & 0 \\ 0 & -1 \end{pmatrix} \right\} e^{i\boldsymbol{\kappa}\cdot\mathbf{r}} \sum_n e^{i\mathbf{G}_n\cdot\mathbf{r}} \begin{bmatrix} c_{n\uparrow} \\ c_{n\downarrow} \end{bmatrix} \\
 & = e^{i\boldsymbol{\kappa}\cdot\mathbf{r}} \sum_n e^{i\mathbf{G}_n\cdot\mathbf{r}} E_n \begin{bmatrix} c_{n\uparrow} \\ c_{n\downarrow} \end{bmatrix}.
 \end{aligned} \tag{3.6}$$

The wave function $\Psi_{\kappa}(\mathbf{r})_{\kappa} = \Psi(\mathbf{r})_{\mathbf{k}+\mathbf{K}_1}$ (\mathbf{k} is very close to \mathbf{K}_1 , all at the equivalent \mathbf{K} points (see Fig. 2.4) can be approximately expressed as a linear superposition of three plane-wave states,

$$\Psi_{\kappa,s}(\mathbf{r}) = \frac{1}{\sqrt{3A_c}} [c_{1s} \exp(i(\mathbf{K}_1 + \mathbf{k}) \cdot \mathbf{r}) + c_{2s} \exp(i(\mathbf{K}_2 + \mathbf{k}) \cdot \mathbf{r}) + c_{3s} \exp(i(\mathbf{K}_3 + \mathbf{k}) \cdot \mathbf{r})], \quad (3.7)$$

where $s = \pm 1$ (spin up $s=1$; spin down $s=-1$), and $\frac{\mathbf{p}^2}{2m^*} + V(\mathbf{r})$ expand is subspace of $|\mathbf{k} + \mathbf{K}_1\rangle$, $|\mathbf{k} + \mathbf{K}_2\rangle$ and $|\mathbf{k} + \mathbf{K}_3\rangle$, will give

$$\frac{\hbar^2 K^2}{2m^*} \begin{pmatrix} 1 & 0 & 0 \\ 0 & 1 & 0 \\ 0 & 0 & 1 \end{pmatrix} + H_0 + H_1,$$

Here, H_0 , given by Eq. (2.9), denotes the effect of $V(\mathbf{r})$, and H_1 given by Eq. (2.10) which is linear in \mathbf{k} .

The Eq. (3.6) has a spin-orbit term, as show bellow

$$\begin{aligned} & h_{SO} \Psi_{s=\pm 1}(\mathbf{r}) \\ &= -i\lambda e^{i\mathbf{k}\cdot\mathbf{r}} \sum_m V'_m \left[e^{i[\mathbf{K}_1+(\mathbf{G}_1+\mathbf{G}_m)]\cdot\mathbf{r}} \{ \mathbf{G}_m \times [\mathbf{G}_1 + (\mathbf{K}_1 + \mathbf{k})] \} c_{1s} \right. \\ & \quad \left. + \begin{aligned} & e^{i[\mathbf{K}_1+(\mathbf{G}_2+\mathbf{G}_m)]\cdot\mathbf{r}} \{ \mathbf{G}_m \times [\mathbf{G}_2 + (\mathbf{K}_1 + \mathbf{k})] \} c_{2s} \\ & e^{i[\mathbf{K}_1+(\mathbf{G}_3+\mathbf{G}_m)]\cdot\mathbf{r}} \{ \mathbf{G}_m \times [\mathbf{G}_3 + (\mathbf{K}_1 + \mathbf{k})] \} c_{3s} \end{aligned} \right] \quad (3.8) \\ &= -i\lambda e^{i\mathbf{k}\cdot\mathbf{r}} \sum_m V'_m \left[e^{i(\mathbf{K}_1+\mathbf{G}_m)\cdot\mathbf{r}} \mathbf{G}_m \times (\mathbf{K}_1 + \mathbf{k}) c_{1s} \right. \\ & \quad \left. + e^{i(\mathbf{K}_2+\mathbf{G}_m)\cdot\mathbf{r}} \mathbf{G}_m \times (\mathbf{K}_2 + \mathbf{k}) c_{2s} + e^{i(\mathbf{K}_3+\mathbf{G}_m)\cdot\mathbf{r}} \mathbf{G}_m \times (\mathbf{K}_3 + \mathbf{k}) c_{3s} \right], \end{aligned}$$

$$\begin{aligned}
 & h_{SO}\Psi_{s=\pm 1}(\mathbf{r}) \\
 &= -i\lambda \begin{bmatrix} V'_{1-1}\mathbf{G}_{1-1} \times (\kappa_1) & V'_{1-2}\mathbf{G}_{1-2} \times (\kappa_2) & V'_{1-3}\mathbf{G}_{1-3} \times (\kappa_3) \\ V'_{2-1}\mathbf{G}_{2-1} \times (\kappa_1) & V'_{2-2}\mathbf{G}_{2-2} \times (\kappa_2) & V'_{2-3}\mathbf{G}_{2-3} \times (\kappa_3) \\ V'_{3-1}\mathbf{G}_{3-1} \times (\kappa_1) & V'_{3-2}\mathbf{G}_{3-2} \times (\kappa_2) & V'_{3-3}\mathbf{G}_{3-3} \times (\kappa_3) \end{bmatrix} \begin{bmatrix} e^{i(\mathbf{K}_1+\mathbf{k})\cdot\mathbf{r}} c_{1s} \\ e^{i(\mathbf{K}_2+\mathbf{k})\cdot\mathbf{r}} c_{2s} \\ e^{i(\mathbf{K}_3+\mathbf{k})\cdot\mathbf{r}} c_{3s} \end{bmatrix} \\
 &= \begin{bmatrix} E_{1s} e^{i(\mathbf{K}_1+\mathbf{k})\cdot\mathbf{r}} c_{1s} \\ E_{2s} e^{i(\mathbf{K}_2+\mathbf{k})\cdot\mathbf{r}} c_{2s} \\ E_{3s} e^{i(\mathbf{K}_3+\mathbf{k})\cdot\mathbf{r}} c_{3s} \end{bmatrix},
 \end{aligned} \tag{3.9}$$

where $\kappa_1 = \mathbf{K}_1 + \mathbf{k}$, $\kappa_2 = \mathbf{K}_2 + \mathbf{k}$, $\kappa_3 = \mathbf{K}_3 + \mathbf{k}$, and the same spatial factor $e^{i\mathbf{k}\cdot\mathbf{r}} e^{i(\mathbf{G}_n+\mathbf{K}_1)\cdot\mathbf{r}}$ on both side can be ignore for the matrix form.

$$\begin{aligned}
 & h_{SO}(\boldsymbol{\kappa}) \\
 &= -i\lambda W \begin{bmatrix} 0 & (\mathbf{G}_{1-2} \times \mathbf{K}_2 + \mathbf{G}_{1-2} \times \mathbf{k}) & (\mathbf{G}_{1-3} \times \mathbf{K}_3 + \mathbf{G}_{1-3} \times \mathbf{k}) \\ (\mathbf{G}_{2-1} \times \mathbf{K}_1 + \mathbf{G}_{2-1} \times \mathbf{k}) & 0 & (\mathbf{G}_{2-3} \times \mathbf{K}_3 + \mathbf{G}_{2-3} \times \mathbf{k}) \\ (\mathbf{G}_{3-1} \times \mathbf{K}_1 + \mathbf{G}_{3-1} \times \mathbf{k}) & (\mathbf{G}_{3-2} \times \mathbf{K}_2 + \mathbf{G}_{3-2} \times \mathbf{k}) & 0 \end{bmatrix},
 \end{aligned} \tag{3.10}$$

where $V'_{n-m} = V'_{1-2} = V'_{2-1} = V'_{1-3} = V'_{3-1} = V'_{2-3} = V'_{3-2} = W$; $V'_{1-1} = V'_{2-2} = V'_{3-3} = 0$ ($V'_m = \frac{2\pi U_0 d}{\sqrt{3} G_m a_1 a_2} J_1(\frac{G_m d}{2})$), and we also assume $A = G_{n-m} \cdot K_n \sin(\frac{5\pi}{6})$. At the \mathbf{K} point, the H_0 has a doubly degenerate energy $-W$. Using the correspond eigenstates, $|c_1\rangle$ and $|c_2\rangle$ given by, Eq. (2.11), Eq. (2.12), we obtain the 2×2 subspace representation of H_0 , H_1 and h_{SO} .

$$\tilde{H}_0 = \begin{pmatrix} \langle c_1 | H_0 | c_1 \rangle & \langle c_1 | H_0 | c_2 \rangle \\ \langle c_2 | H_0 | c_1 \rangle & \langle c_2 | H_0 | c_2 \rangle \end{pmatrix} = -W \begin{pmatrix} 1 & 0 \\ 0 & 1 \end{pmatrix}, \quad (3.11)$$

$$\tilde{H}_1 = \begin{pmatrix} \langle c_1 | H_1 | c_1 \rangle & \langle c_1 | H_1 | c_2 \rangle \\ \langle c_2 | H_1 | c_1 \rangle & \langle c_2 | H_1 | c_2 \rangle \end{pmatrix} = \frac{\hbar v_0}{2} \begin{pmatrix} -k_x & -k_y \\ -k_y & k_x \end{pmatrix}, \quad (3.12)$$

$$\tilde{h}_{SO,s} = \begin{pmatrix} \langle c_1 | H_{SO} | c_1 \rangle & \langle c_1 | H_{SO} | c_2 \rangle \\ \langle c_2 | H_{SO} | c_1 \rangle & \langle c_2 | H_{SO} | c_2 \rangle \end{pmatrix} = i\sqrt{3}s\lambda W A \begin{pmatrix} 0 & 1 \\ -1 & 0 \end{pmatrix}, \quad (3.13)$$

where λ is spin-orbit coupling constant. We ignore the energy shift term \tilde{H}_0 and obtain:

$$\tilde{H}_1 + \tilde{h}_{SO,s} = \begin{pmatrix} -\frac{\hbar v_0}{2} k_x & -\frac{\hbar v_0}{2} k_y + i\sqrt{3}s\lambda W A \\ -\frac{\hbar v_0}{2} k_y - i\sqrt{3}s\lambda W A & \frac{\hbar v_0}{2} k_x \end{pmatrix}, \quad (3.14)$$

$$E = -W \pm \sqrt{\left(\frac{\hbar v_0}{2} k\right)^2 + 3(s\lambda W)^2}. \quad (3.15)$$

The Eq. (3.15) shows the lowest two energy bands at K point opens up a gap ($2\sqrt{3}\lambda W$), the $s=1$ (spin-up) and $s=-1$ (spin-down) the energy dispersion is the same (which is as same as numerical result, see subsection 3.4).

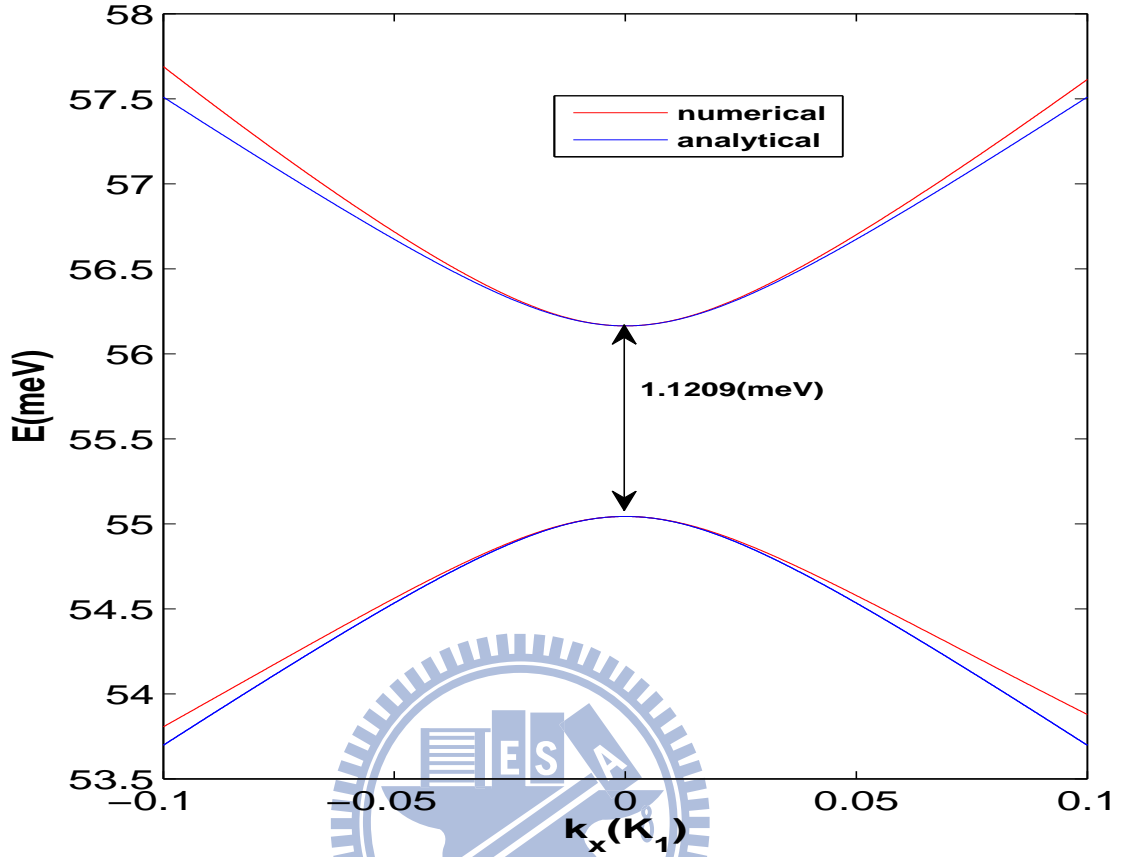


Figure 3.1: The lowest two bands which wave vector is near K_1 ($k_y=0$, $-0.1K_1 < k_x < 0.1K_1$). The red line: the numerical result for three K point with SOI; blue line: the analytic result for 2×2 matrix with SOI, $\lambda=120\text{\AA}^2$ (InAs); $m^* = 0.023m_e$; $U_0 = 165\text{meV}$; $a=40\text{nm}$; $d=0.663a$.

The Fig. 3.5 shows the energy of analytic energy band (restrict in subspace) is higher than numerical energy band (3×3 matrix) except the $\mathbf{k} \approx 0$ (close to K_1). Because of the numerical energy band consider the $2W$ (higher energy), leading the energy higher than analytic energy band (only consider $-W$).

3.2 The position symmetry for muffin-tin triangular lattice

There are an external muffin-tin triangular potential in the 2DEG. This structure has a symmetry property for rotating 60° along the z-axis. We can interpret the symmetry

property from Fig. 3.2, each muffin-tin triangular structure (a), (b), (c) in real-space have the corresponding BZ (a), (b), (c) in k-space. For example, the figure (a) rotate 60° to become figure (b) in real-space and the K system in (a) change to K' system in (b) relatively in k-space. Because of the action for rotating 60° doesn't change the structure, the rotating symmetry is tenable.

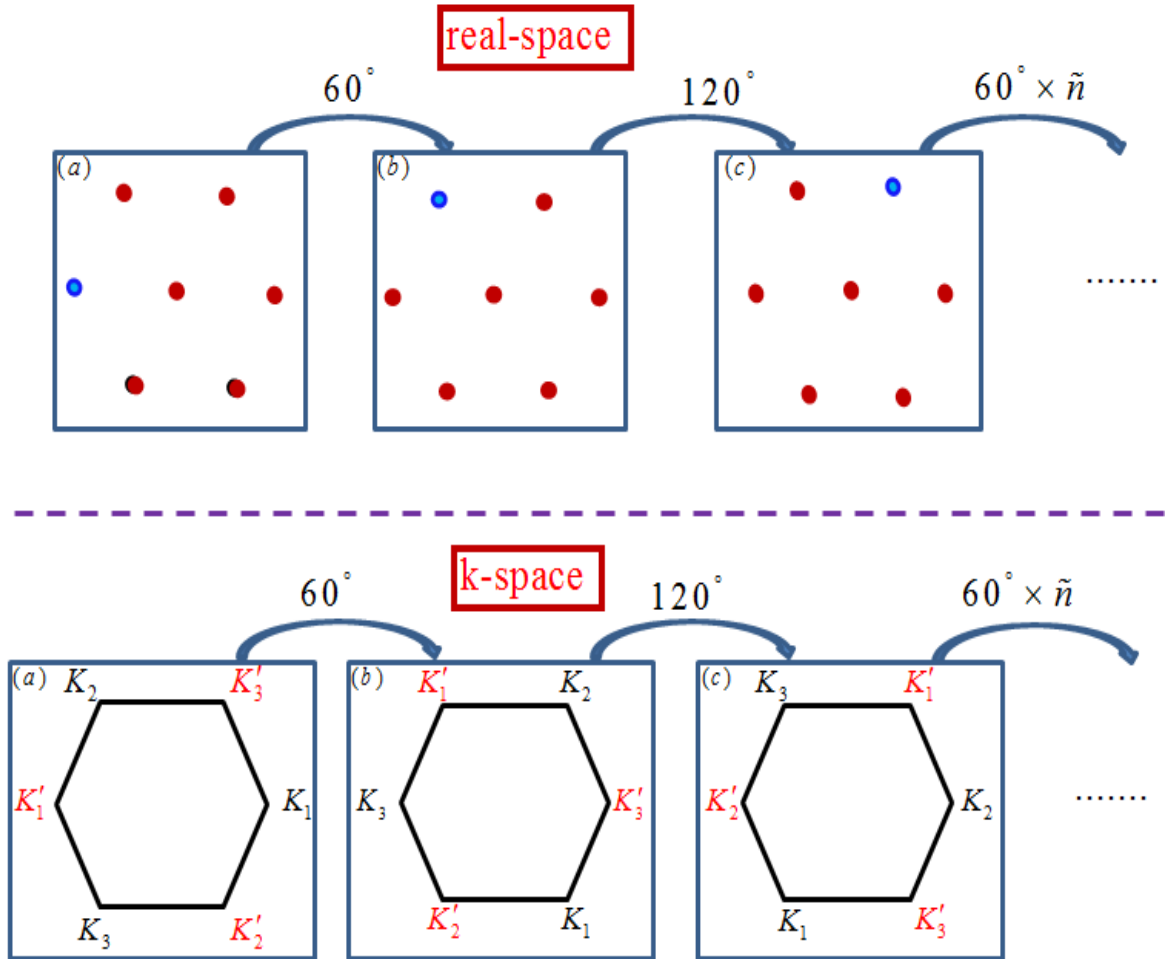


Figure 3.2: This figure shows the rotating symmetry property for triangular lattice, the original system (a) in real-space correspond to (a) in k-space, then rotate $\frac{\pi}{3}$ from central point to become (b) in real-space and k-space, and do the same work to become (c) in real-space and k-space, where \tilde{n} is an integer (the blue point note the system which has been rotated).

For the analytic calculation, the wave function expanded from K'_1 point (using the K'_1, K'_2, K'_3 be the basis), the method is as same as K system. There are only H_1 term different

from K system which the \mathbf{k} become $-\mathbf{k}$.

$$H_1 = -\hbar v_0 k \begin{pmatrix} \cos \theta_{\mathbf{k}} & 0 & 0 \\ 0 & \cos(\theta_{\mathbf{k}} - \frac{2\pi}{3}) & 0 \\ 0 & 0 & \cos(\theta_{\mathbf{k}} - \frac{4\pi}{3}) \end{pmatrix}, \quad (3.16)$$

Therefore, we obtain the subspace (as show in Eq. (3.12) and Eq. (3.13)) representation of H_0 , H_1 and h_{SO} , and count the energy dispersion. The result of energy dispersion in K' system is as same as K system $E = -W \pm \sqrt{(\frac{\hbar v_0}{2} k)^2 + 3(sA\lambda W)^2}$. This result prove the position symmetry property(show in Fig. 3.2) which is authentic.

3.3 The numerical result compare with single well system in the presence of SOI

Using the same numerical program calculates the case of $U_0 = -300\text{meV}$. When the extra potential is negative, the MTP resembles many single wells. Such wave under MTP can be illustrated by the overlapping wave functions of the nearest single wells.

$$H_{SO} = -\frac{\lambda}{\hbar} \boldsymbol{\sigma} \cdot \left(\hat{r} \frac{\partial V}{\partial r} \times \mathbf{p} \right) = -\frac{\lambda}{\hbar r} \frac{\partial V}{\partial r} \boldsymbol{\sigma} \cdot (\mathbf{r} \times \mathbf{p}) = -\frac{\lambda}{\hbar r} \frac{\partial V}{\partial r} \sigma_z L_z. \quad (3.17)$$

The disk-shaped potential with step-like profile $V(r) = -V_0 \theta(\frac{d}{2} - r)$ gives rise to SOI term, where d is the diameter of the single well.

$$H_{SO} = -\frac{\lambda V_0 \delta(\frac{d}{2} - r)}{\hbar r} \sigma_z L_z. \quad (3.18)$$

The total wave function with spin state χ_s is written as $\Psi_{\kappa,s}(r, \phi) = R_i^s(r) \Phi(\phi) \chi_s = R_i^s(r) e^{i l \phi} \chi_s$.

Here $\sigma_z \chi_s = s \chi_s$, ($s = \pm 1$ the meaning is spin-up or spin-down state). Substituting

wave function into the Schrodinger equation, the radial differential equation reads

$$\left[\frac{d}{dr} \left(r \frac{d}{dr} \right) - \frac{l^2}{r} - \frac{rV(r)}{A} - \frac{lsH_{SO}}{A} \right] R_l^s(r) = -\frac{r}{A} E R_l^s(r). \quad (3.19)$$

The radial function $R_l^s(r)$ has different coefficients for inside and outside the disk, that depend on the index s, given by

$$R_l^s(r) = \begin{cases} C_l^s J_l(\alpha r) & r \leq \frac{d}{2}, \\ E_l^s K_l(\beta r) & r \geq \frac{d}{2}, \end{cases} \quad (3.20)$$

The H_{SO} is nonzero only at $r=\frac{d}{2}$, the boundary condition that bring forth the spin degeneracy is given by

$$r \frac{dR_l(r)}{dr} \Big|_{\frac{d}{2}^+} + \frac{\lambda s V_0}{A} R_l\left(\frac{d}{2}\right) = 0. \quad (3.21)$$

Finally, the wave function is continuous at boundary, we obtain the coefficient C_l^s , E_l^s , energy level, and orbital quantum number.

Compared with the energy level of a single well, we can obviously discover the each energy band is almost same level (see Fig. 3.3). There are two energy bands equal to same orbital quantum number (l) when the $|l| \neq 0$. For the (l)=0 case, only have one energy band because the $l=0$ did not have opposite quantum number. This work can provide a method to prove the program which is authentic.

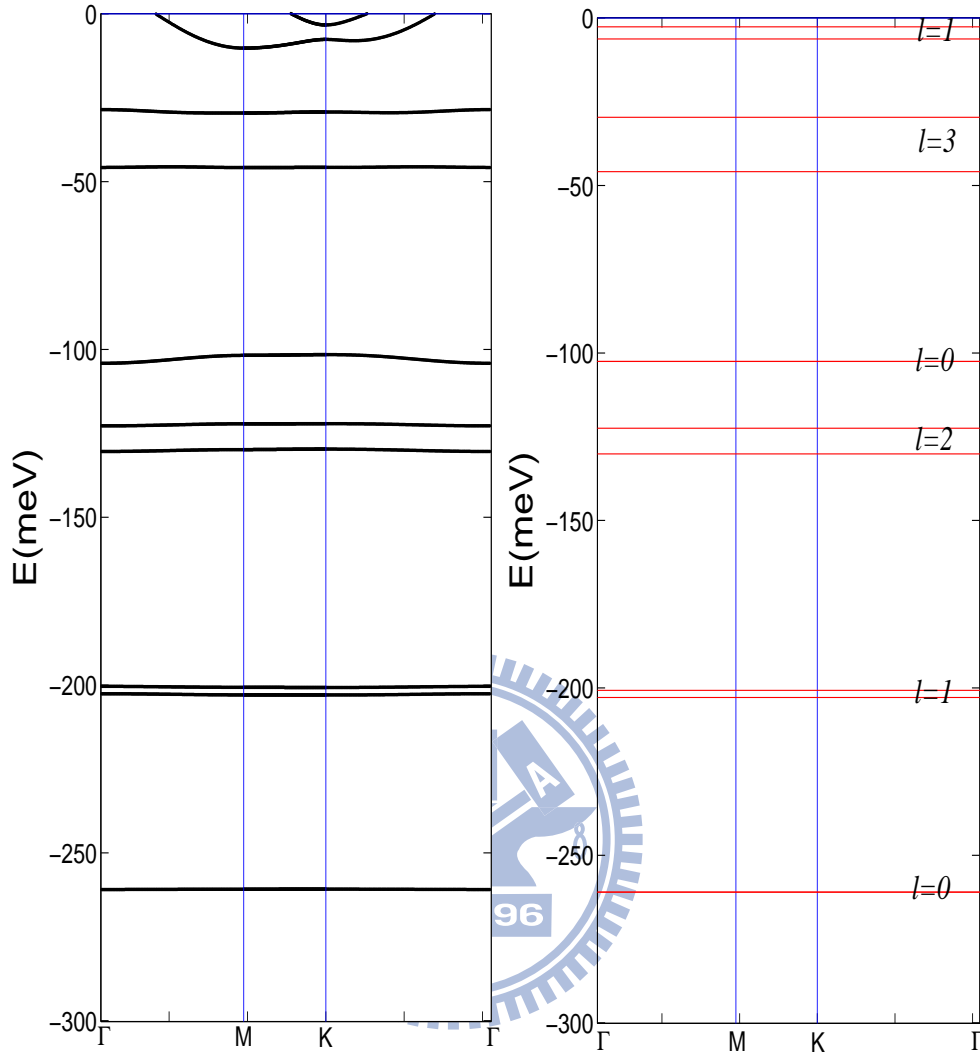


Figure 3.3: Energy band structure with parameters units typical for InAs are: effective mass $m^*=0.023m_e$; $a = 40\text{nm}$; SO coupling constant $\lambda=120\text{\AA}^2$ (a) numerical muffin-tin potential ($U_0 = -300\text{meV}$) in the presence of SOI. Compared with (b) single well ($V_0=300\text{meV}$) in 2DEG.

3.4 Results for energy band structure in the presence of SOI

In our numerical examples, physic parameters are chosen for InAs in the practical experimental parameters. The Fig. 3.4 shows the energy dispersion with SOI which open

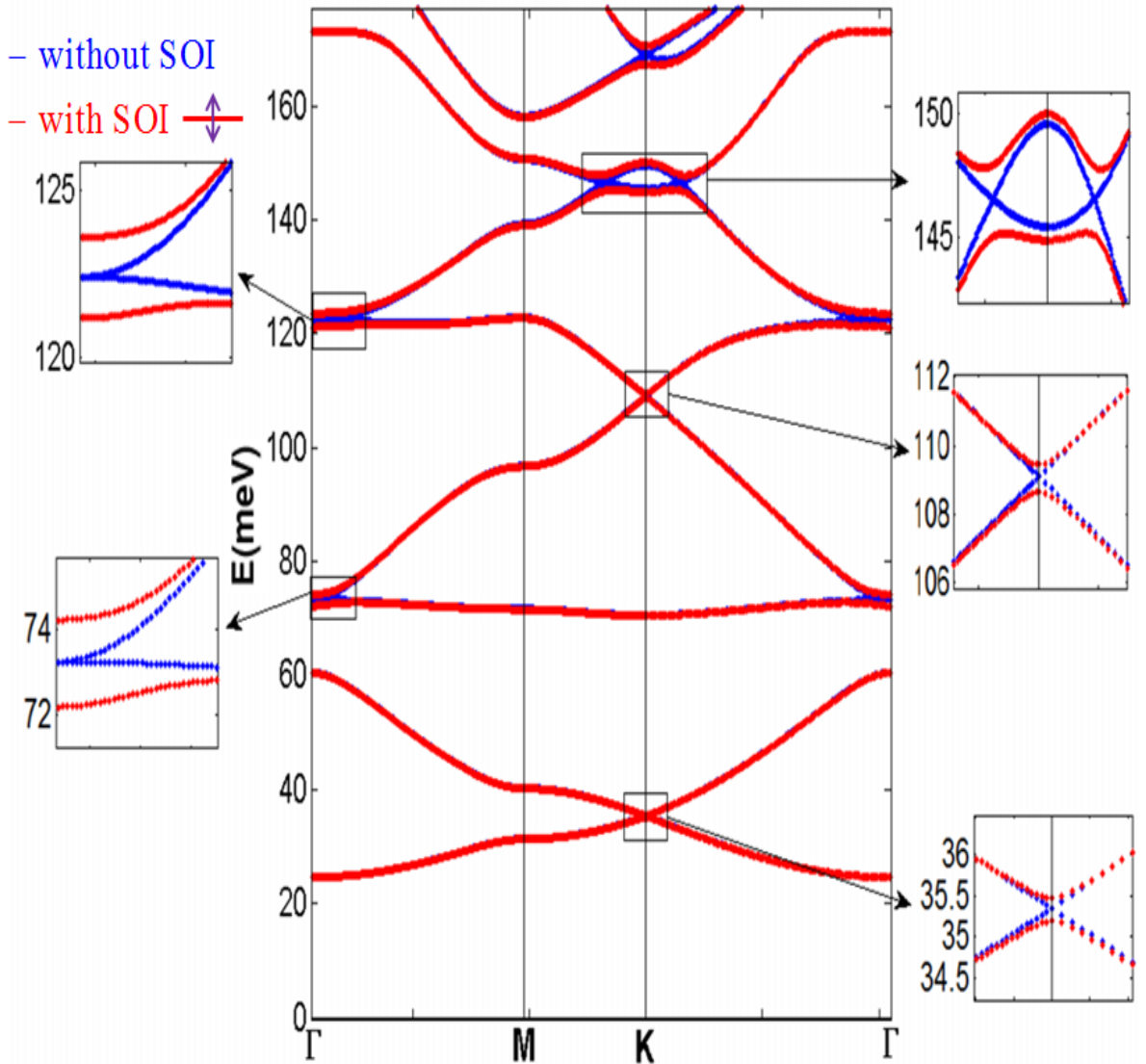


Figure 3.4: Parameters units typical for InAs are: effective mass $m^*=0.023m_e$; $U_0 = 165\text{meV}$, $a = 40\text{nm}$; SO coupling constant $\lambda=120\text{\AA}^2$ The blue line is without SOI and the red line is with SOI which spin-up and spin-down are flipping in muffin-tin lattice.

up gaps at K and Γ points (the magnitudes of each gaps are shown in Fig. 5.7), the

spin-up states and spin-down states are same energy dispersion but spins opposite site in z-direction (Fig. 3.4). And for the lowest two energy band, the spin-up and spin-down

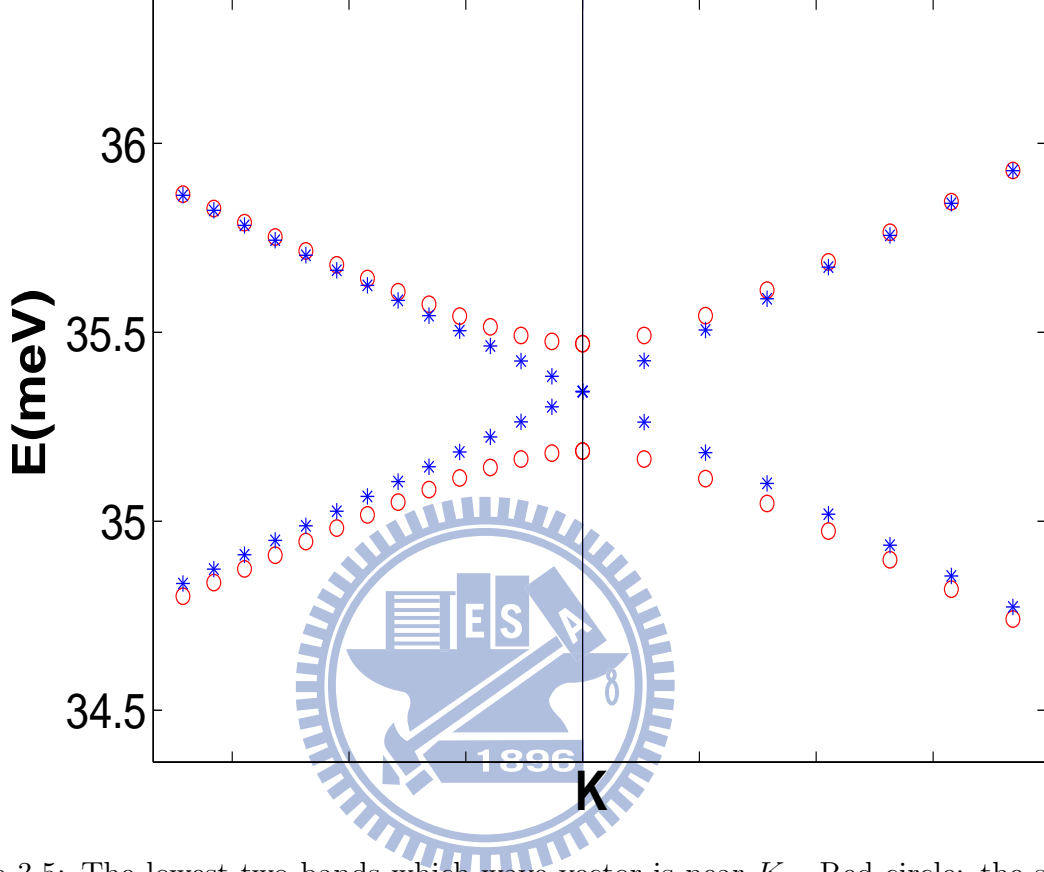


Figure 3.5: The lowest two bands which wave vector is near K_1 . Red circle: the system with SOI; blue star: the system without SOI, $\lambda=120\text{\AA}^2(\text{InAs})$; $m^* = 0.023m_e$; $U_0 = 165\text{meV}$; $a=40\text{nm}$; $d=0.663a$.

states mixing at K_1 point without SOI (see Eq. (3.5)).

$$\begin{aligned}
 & \left[H_{SO}, \frac{\mathbf{p}^2}{2m^*} + V(\mathbf{r}) \right] \\
 &= \left[(\partial_x V) \mathbf{p}_y - (\partial_y V) \mathbf{p}_x, \frac{\mathbf{p}^2}{2m^*} + V(\mathbf{r}) \right]. \quad (3.22) \\
 & \neq 0
 \end{aligned}$$

Because of Eq. (3.22), the states at K point is a superposition state with the basis is the eigenstate without SOI, leading to open up a gap for first lowest energy band and second

lowest energy band (Fig. 3.5).

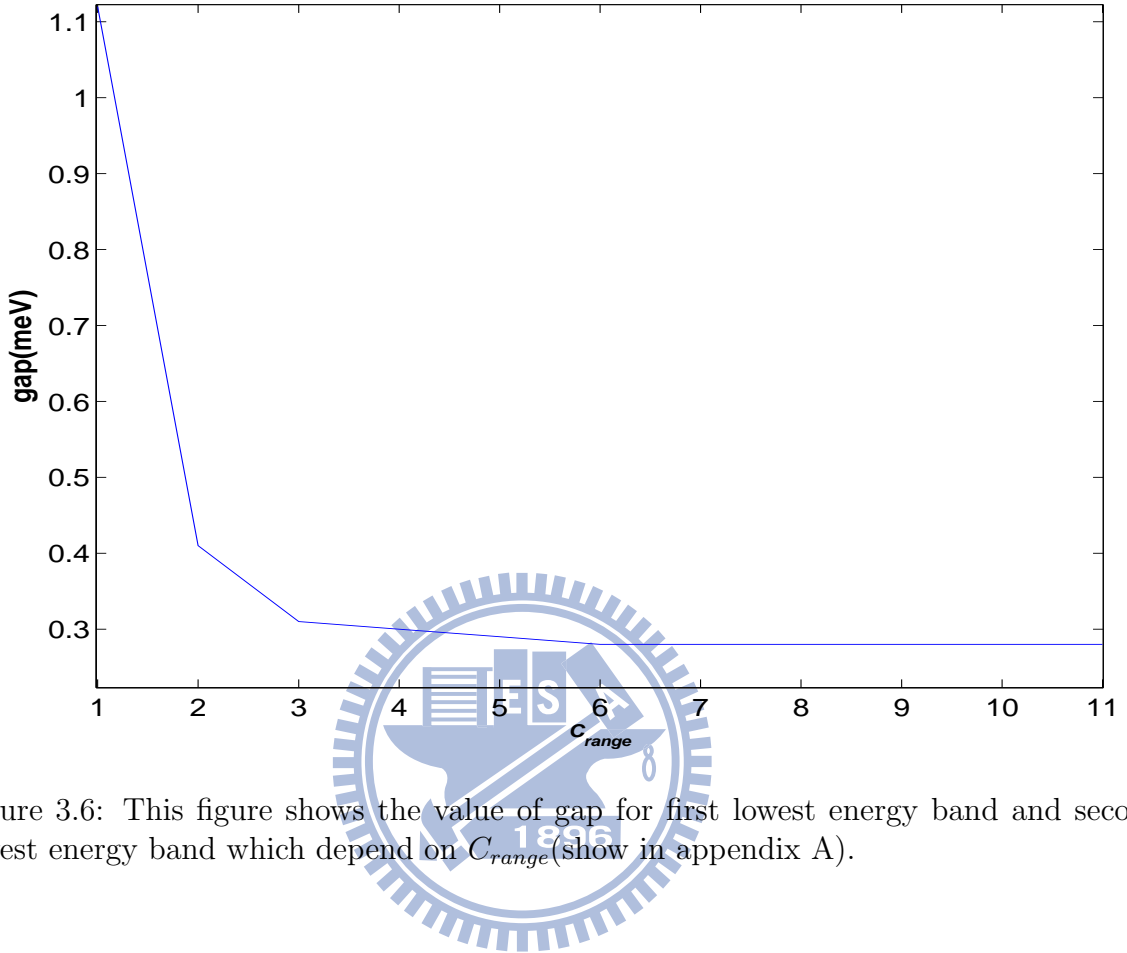


Figure 3.6: This figure shows the value of gap for first lowest energy band and second lowest energy band which depend on C_{range} (shown in appendix A).

The Fig. 3.6 shows the magnitude of the gap (between first lowest energy band and second lowest energy band) would decrease when the C_{range} (orbital index) increase. We have trying other parameters for different a , d , U_0 , and roughly discuss the results, because for $C_{range}=1$ (shown in appendix E).

3.5 The relationship between time reversal property and our system

The numerical results show the energy dispersion of spin-up and spin-down states are same energy dispersion. We analyze the these results by time reversal symmetry. The wave function and Schrödinger equation are given by

$$\Psi_{\boldsymbol{\kappa},s}(\mathbf{r}) = e^{i\boldsymbol{\kappa}\cdot\mathbf{r}} \sum_s u_{\boldsymbol{\kappa},s}(\mathbf{r}) \chi_s = e^{i\boldsymbol{\kappa}\cdot\mathbf{r}} \left(\begin{bmatrix} u_{\boldsymbol{\kappa},s}(\mathbf{r}) \\ 0 \end{bmatrix}_{s=1} + \begin{bmatrix} 0 \\ u_{\boldsymbol{\kappa},s}(\mathbf{r}) \end{bmatrix}_{s=-1} \right), \quad (3.23)$$

$$\begin{aligned} H\Psi_{\boldsymbol{\kappa},s}(\mathbf{r}) &= \left\{ H_0 \begin{pmatrix} 1 & 0 \\ 0 & 1 \end{pmatrix} + h_{so} \begin{pmatrix} 1 & 0 \\ 0 & -1 \end{pmatrix} \right\} e^{i\boldsymbol{\kappa}\cdot\mathbf{r}} \sum_n e^{i\mathbf{G}_n\cdot\mathbf{r}} \begin{pmatrix} c_{n,\boldsymbol{\kappa},s=1} \\ c_{n,\boldsymbol{\kappa},s=-1} \end{pmatrix} \\ &= e^{i\boldsymbol{\kappa}\cdot\mathbf{r}} \sum_n e^{i\mathbf{G}_n\cdot\mathbf{r}} \begin{pmatrix} E_{s=1} c_{n,\boldsymbol{\kappa},s=1} \\ E_{s=-1} c_{n,\boldsymbol{\kappa},s=-1} \end{pmatrix}, \end{aligned} \quad (3.24)$$

where the periodic function $u_{\boldsymbol{\kappa},s=\pm 1}(\mathbf{r}) = \sum_n e^{i\mathbf{G}_n\cdot\mathbf{r}} c_{n,\boldsymbol{\kappa},s}$; $s = \pm 1$ is meaning spin-up and spin-down and the definition of $H_{SO} = -\frac{i\lambda}{\hbar} \sum_m e^{i\mathbf{G}_m\cdot\mathbf{r}} V'_m \boldsymbol{\sigma} \cdot (\mathbf{G}_m \times \mathbf{p}) = h_{so} \sigma_z$. Because of $\sigma_z \chi_s = s \chi_s$ the Schrödinger equation turns out to be:

$$(H_{N.SO} + sh_{SO}) e^{i\boldsymbol{\kappa}\cdot\mathbf{r}} |u_{\boldsymbol{\kappa},s}\rangle \chi_s = E_{\boldsymbol{\kappa},s} e^{i\boldsymbol{\kappa}\cdot\mathbf{r}} |u_{\boldsymbol{\kappa},s}\rangle \chi_s. \quad (3.25)$$

Time reversal operator Θ acts on Eq. (3.25), one obtain that

$$(H_{N.SO} - sh_{SO}) e^{-i\boldsymbol{\kappa}\cdot\mathbf{r}} |u_{-\boldsymbol{\kappa},-s}\rangle \chi_{-s} = E_{\boldsymbol{\kappa},s} e^{-i\boldsymbol{\kappa}\cdot\mathbf{r}} |u_{-\boldsymbol{\kappa},-s}\rangle \chi_{-s}, \quad (3.26)$$

where

$$\begin{aligned} \Theta h_{SO} &= \Theta \left[-\frac{i\lambda}{\hbar} \sum_m e^{i\mathbf{G}_m\cdot\mathbf{r}} V'_m (\mathbf{G}_m \times \mathbf{p})_z \right] = \frac{i\lambda}{\hbar} \sum_m e^{i\mathbf{G}_m\cdot\mathbf{r}} V'_m (\mathbf{G}_{-m} \times -\mathbf{p})_z \Theta \\ &= -h_{SO} \Theta, \end{aligned} \quad (3.27)$$

and

$$\Theta |u_{\boldsymbol{\kappa},s}\rangle \chi_s = |u_{\boldsymbol{\kappa},s}\rangle^* \sigma_y \chi_s = |u_{\boldsymbol{\kappa},s}\rangle^* \chi_{-s} e^{i\delta} \Rightarrow |u_{-\boldsymbol{\kappa},-s}\rangle = |u_{\boldsymbol{\kappa},s}\rangle^*.$$

The eigenstate of Eq. (3.26) is $|u_{-\kappa,-s}\rangle$, so the eigenenergy of this system must be $E_{-\kappa,-s}$ which implicate $E_{\kappa,s} = E_{-\kappa,-s}$, and because $E_{\kappa,-s} = E_{-\kappa,-s}$, which comes from the parity operator π acting on Eq. (3.25), we obtain

$$(H_{\text{N.SOI}} + sh_{\text{SO}}) e^{-i\kappa \cdot \mathbf{r}} |u_{-\kappa,s}\rangle \chi_s = E_{\kappa,s} e^{-i\kappa \cdot \mathbf{r}} |u_{-\kappa,s}\rangle \chi_s, \quad (3.28)$$

where the rotating symmetry for triangular lattice (see Fig. 3.2 shows the system in our model with inversion symmetry, the result $E_{\kappa,s} = E_{\kappa,-s}$ is proven.

3.6 Brief summary

Thus far in this chapter, we show that the energy band structure with SOI effect in external periodic potential in 2DEG. There exist a massless Dirac point at K_1 without SOI effect (as show in chapert2), and we considered the MTP gradient which arise the SOI, the degenerated energy at K point can open up a gap, and we also have an analytic calculation to prove the numerical result is authentic.

Chapter 4

Berry curvature with SOI effect in our system

Berry curvature is as a local gauge potential and gauge field associated with the Berry phase. These concepts were introduced by Michael Berry in a paper published in 1984 [14] emphasizing how geometric phases provide a powerful unifying concept in several branches of classical and quantum physics. Such phase have come to be know as Berry phases. In this chapter, we will show the Berry curvature with SOI effect in our system.

4.1 Berry phase

In quantum mechanics, the Berry phase arises in a cyclic adiabatic evolution. The quantum adiabatic theorem applies to a system whose Hamiltonian $H(\boldsymbol{\kappa})$ depends on $\boldsymbol{\kappa}$ that varies with time t . If the n 'th eigenvalue $\varepsilon_n(\boldsymbol{\kappa})$ remains non-degenerate everywhere along the path and the variation with time t is sufficiently slow, then a system initially in the eigenstate $|u_{\boldsymbol{\kappa}(0),n}\rangle$ will remain in an instantaneous eigenstate $|u_{\boldsymbol{\kappa}(t),n}\rangle$, up to a phase, throughout the process. The state at time t can be written as

$$|\Psi_n(t)\rangle = e^{i\gamma_n(t)} e^{-\frac{i}{\hbar} \int_0^t dt' \varepsilon_n(\boldsymbol{\kappa}(t'))} |u_{\boldsymbol{\kappa}(t),n}\rangle, \quad (4.1)$$

where the second exponential term is "dynamic phase factor" and the first exponential term is the geometric term, with γ_n being the Berry phase. By plugging into the time-dependent Schrödinger equation, we can obtain the solution of $\gamma_n(t)$

$$\gamma_n(t) = i \int_0^t dt' \langle u_{\kappa(t'),n} | \frac{d}{dt'} | u_{\kappa(t'),n} \rangle = i \int_{\kappa(0)}^{\kappa(t)} d\kappa \cdot \langle u_{\kappa,n} | \frac{d}{d\kappa} | u_{\kappa,n} \rangle. \quad (4.2)$$

In the case of a cyclic evolution around a close path $\kappa(t) = \kappa(0)$,

From Stoke's theorem, we have

$$\gamma_n(C) = i \iint_C d\mathbf{S} \cdot \nabla_{\kappa} \times \langle u_{\kappa,n} | \nabla_{\kappa} u_{\kappa,n} \rangle = \iint_C d\mathbf{S} \cdot \Omega_n(\kappa), \quad (4.3)$$

where $\Omega_n(\kappa) = i \nabla_{\kappa} \times \langle u_{\kappa,n} | \nabla_{\kappa} u_{\kappa,n} \rangle$ is call the Berry curvature. One might worry that the arbitrary phase attached our expression in Eq. (4.3). To examine this we consider the following gauge transformation $|\tilde{u}_{\kappa,n}\rangle \equiv e^{i\xi(\kappa)} |u_{\kappa,n}\rangle$, where the $e^{i\xi(\kappa)}$ is a κ dependent phase factor. We get $\langle u_{\kappa,n} | \nabla_{\kappa} u_{\kappa,n} \rangle = i \nabla_{\kappa} \xi(\kappa) + \langle u_{\kappa,n} | \nabla_{\kappa} u_{\kappa,n} \rangle$, and in substituting into Eq. (4.3), the additional term $\nabla_{\kappa} \times \nabla_{\kappa} \xi(\kappa) = 0$. This step shows that the Berry curvature is independent of arbitrary phase factor which dependent on κ in the wave function. As such, the definition of Berry phase in Eq. (4.3) is uniquely defined.

4.2 Berry curvature analysis

For a closed path \mathcal{C} that forms the boundary of a surface \mathcal{S} , the closed-path Berry phase can be rewritten using Stokes' theorem as $\gamma_n = \int_{\mathcal{S}} d\mathbf{S} \cdot \Omega_n(\kappa)$.

From Eq. (4.3), we get:

$$\begin{aligned}
 \gamma_n(C) &= i \iint_C d\mathbf{S} \cdot \nabla_{\boldsymbol{\kappa}} \times \langle u_{\boldsymbol{\kappa},n} | \nabla_{\boldsymbol{\kappa}} u_{\boldsymbol{\kappa},n} \rangle \\
 &= i \iint_C d\mathbf{S} \cdot [\langle \nabla_{\mathbf{k}} u_{\boldsymbol{\kappa},n} | \times | \nabla_{\boldsymbol{\kappa}} u_{\boldsymbol{\kappa},n} \rangle + \langle u_{\boldsymbol{\kappa},n} | \nabla_{\boldsymbol{\kappa}} \times \nabla_{\boldsymbol{\kappa}} u_{\boldsymbol{\kappa},n} \rangle] \\
 &= \iint_C d\mathbf{S} \cdot \boldsymbol{\Omega}_n(\boldsymbol{\kappa}).
 \end{aligned} \tag{4.4}$$

The formulation is as shown below: a complete set $\sum_{n'} |\nabla_{\boldsymbol{\kappa}} u_{\boldsymbol{\kappa},n'}\rangle \langle \nabla_{\boldsymbol{\kappa}} u_{\boldsymbol{\kappa},n'}| = 1$ has been inserted in the second row of Eq. (4.4), and they are grouped into $n \neq n'$ and $n = n'$ terms.

$$\begin{aligned}
 \boldsymbol{\Omega}_n(\boldsymbol{\kappa}) &= i \langle \nabla_{\boldsymbol{\kappa}} u_{\boldsymbol{\kappa},n} | \times | \nabla_{\boldsymbol{\kappa}} u_{\boldsymbol{\kappa},n} \rangle \\
 &= i \left(\sum_{n \neq n'} \langle \nabla_{\mathbf{k}} u_{\boldsymbol{\kappa},n} | u_{\boldsymbol{\kappa},n'} \rangle \times \langle u_{\boldsymbol{\kappa},n'} | \nabla_{\boldsymbol{\kappa}} u_{\boldsymbol{\kappa},n} \rangle + \sum_{n=n'} \langle \nabla_{\boldsymbol{\kappa}} u_{\boldsymbol{\kappa},n} | u_{\boldsymbol{\kappa},n'} \rangle \times \langle u_{\boldsymbol{\kappa},n'} | \nabla_{\boldsymbol{\kappa}} u_{\boldsymbol{\kappa},n} \rangle \right).
 \end{aligned} \tag{4.5}$$

Because of $\nabla_{\boldsymbol{\kappa}} \langle u_{\boldsymbol{\kappa},n} | u_{\boldsymbol{\kappa},n} \rangle = 0$,

$$\begin{aligned}
 &\nabla_{\boldsymbol{\kappa}} \langle u_{\boldsymbol{\kappa},n} | u_{\boldsymbol{\kappa},n} \rangle \\
 &= \langle \nabla_{\boldsymbol{\kappa}} u_{\boldsymbol{\kappa},n} | u_{\boldsymbol{\kappa},n} \rangle + \langle u_{\boldsymbol{\kappa},n} | \nabla_{\boldsymbol{\kappa}} u_{\boldsymbol{\kappa},n} \rangle = \langle u_{\boldsymbol{\kappa},n} | \nabla_{\boldsymbol{\kappa}} u_{\boldsymbol{\kappa},n} \rangle^* + \langle u_{\boldsymbol{\kappa},n} | \nabla_{\boldsymbol{\kappa}} u_{\boldsymbol{\kappa},n} \rangle = 0,
 \end{aligned} \tag{4.6}$$

where $\langle u_{\boldsymbol{\kappa},n} | \nabla_{\boldsymbol{\kappa}} u_{\boldsymbol{\kappa},n} \rangle$ must be pure imaginary, as a result of Eq. (4.5) the second term of the second row is zero.

There is a useful relation for obtaining the numerical formulation:

$$\begin{aligned}
 \langle u_{\boldsymbol{\kappa},n'} | (\nabla_{\boldsymbol{\kappa}} H) | u_{\boldsymbol{\kappa},n} \rangle &= \langle u_{\boldsymbol{\kappa},n'} | (\nabla_{\mathbf{k}} H - H \nabla_{\boldsymbol{\kappa}}) | u_{\boldsymbol{\kappa},n} \rangle \\
 &= \langle u_{\boldsymbol{\kappa},n'} | \nabla_{\boldsymbol{\kappa}} E_{\boldsymbol{\kappa},n} | u_{\boldsymbol{\kappa},n} \rangle - \langle u_{\boldsymbol{\kappa},n'} | E_{\boldsymbol{\kappa},n} \nabla_{\boldsymbol{\kappa}} | u_{\boldsymbol{\kappa},n} \rangle \\
 &= \nabla_{\boldsymbol{\kappa}} E_{\boldsymbol{\kappa},n} \langle u_{\boldsymbol{\kappa},n'} | u_{\boldsymbol{\kappa},n} \rangle + E_{\boldsymbol{\kappa},n} \langle u_{\boldsymbol{\kappa},n'} | \nabla_{\boldsymbol{\kappa}} u_{\boldsymbol{\kappa},n} \rangle - E_{\boldsymbol{\kappa},n'} \langle u_{\boldsymbol{\kappa},n'} | \nabla_{\boldsymbol{\kappa}} u_{\boldsymbol{\kappa},n} \rangle \\
 &= (E_{\boldsymbol{\kappa},n} - E_{\boldsymbol{\kappa},n'}) \langle u_{\boldsymbol{\kappa},n'} | \nabla_{\boldsymbol{\kappa}} u_{\boldsymbol{\kappa},n} \rangle,
 \end{aligned} \tag{4.7}$$

where the $H(\boldsymbol{\kappa})$ comes from $H(\boldsymbol{\kappa}) = U(\boldsymbol{\kappa}) H U^\dagger(\boldsymbol{\kappa}) = e^{-i\boldsymbol{\kappa}\cdot\mathbf{r}} H e^{i\boldsymbol{\kappa}\cdot\mathbf{r}}$. Because of Schrödinger equation: $H|\Psi_{\boldsymbol{\kappa},n}(\mathbf{r})\rangle = H U^\dagger(\boldsymbol{\kappa})|u_{\boldsymbol{\kappa},n}(\mathbf{r})\rangle = \varepsilon_n(\boldsymbol{\kappa})|\Psi_{\boldsymbol{\kappa},n}(\mathbf{r})\rangle = \varepsilon_n(\boldsymbol{\kappa})U^\dagger(\boldsymbol{\kappa})|u_{\mathbf{k},n}(\mathbf{r})\rangle$.

From Eq. (4.7), we obtain:

$$\langle u_{\boldsymbol{\kappa},n'} | \nabla_{\mathbf{k}} u_{\boldsymbol{\kappa},n} \rangle = \frac{\langle u_{\boldsymbol{\kappa},n'} | \nabla_{\boldsymbol{\kappa}} H | u_{\boldsymbol{\kappa},n} \rangle}{E_{\boldsymbol{\kappa},n} - E_{\boldsymbol{\kappa},n'}}, \quad n \neq n', \quad (4.8)$$

and substituted to Eq. (4.5). The numerical calculation of Berry curvature is read as:

$$\Omega_n(\boldsymbol{\kappa}) = i \sum_{n' \neq n} \frac{\langle u_{\boldsymbol{\kappa},n} | \partial_{k_x} H(\boldsymbol{\kappa}) | u_{\boldsymbol{\kappa},n'} \rangle \langle u_{\boldsymbol{\kappa},n'} | \partial_{k_y} H(\boldsymbol{\kappa}) | u_{\boldsymbol{\kappa},n} \rangle - (x \leftrightarrow y)}{[E_{n'}(\boldsymbol{\kappa}) - E_n(\boldsymbol{\kappa})]^2} \hat{z}. \quad (4.9)$$

The Eq. (4.9) shows explicitly, that the Berry curvature is due to the restriction to a single band n and to the resulting virtual transitions to other bands $n' \neq n$, and the numerical result n' is the effective number for two bands which are the nearest for each higher energy and lower energy (Because of the denominator $[E_n(\boldsymbol{\kappa}) - E_{n'}(\boldsymbol{\kappa})]^2$ in Eq. (4.9)). For example, the $n=1$, $n'=2, 3$ and another case the $n=4$, $n'=2, 3$ (lower energy), 5, 6 (higher energy).

4.2.1 The analytic result of Berry curvature

The wave function $\Psi_{\boldsymbol{\kappa},s}(\mathbf{r})$ may be approximately expressed as a linear combination of three plane-wave states.

The term $H_1 + H_{SO}$, when restricted to the sub-Hilbert space spanned by the two vectors (the degenerate eigenvectors of lowest two bands) is represented by a 2×2 matrix $\tilde{H}_1 + \tilde{H}_{SO}$ (shown in chapter 3.1.1), the meaning of this step is that we only focus on the Berry curvature of \mathbf{k} -space near K point (the Dirac point of the lowest band).

$$\tilde{H}_1 + \tilde{H}_{SO} = \begin{pmatrix} -\frac{\hbar v_0}{2} k_x & -\frac{\hbar v_0}{2} k_y + i\sqrt{3}s\lambda W A \\ -\frac{\hbar v_0}{2} k_y - i\sqrt{3}s\lambda W A & \frac{\hbar v_0}{2} k_x \end{pmatrix}, \quad (4.10)$$

$$\begin{pmatrix} -P_0k_x & -P_0k_y + i\Delta_s \\ -P_0k_y - i\Delta_s & P_0k_x \end{pmatrix} \begin{pmatrix} Y_{n,s} \\ Z_{n,s} \end{pmatrix} = n\sqrt{(P_0k)^2 + \Delta_s^2} \begin{pmatrix} Y_{n,s} \\ Z_{n,s} \end{pmatrix}, \quad (4.11)$$

where $\Delta_s = \sqrt{3}s\lambda WA$, $s=\pm 1$ (spin index), $P_0 = \frac{\hbar v_0}{2}$, $v_0 = \frac{\hbar K_1}{m^*}$; Schrödinger equation $[\tilde{H}_1(\boldsymbol{\kappa}) + \tilde{H}_{SO}(\boldsymbol{\kappa})] |u_{\boldsymbol{\kappa},n,s}\rangle = E_n |u_{\boldsymbol{\kappa},n,s}\rangle$; $n = \pm 1$ ($n = 1$, the second lowest band; $n = -1$, the first lowest band); $Y_{n,s}, Z_{n,s}$ are the elements of $|u_{\boldsymbol{\kappa},n,s}\rangle$. The solution of Eq. (4.11) is $Z_{n,s} = \frac{P_0k_x + n\sqrt{(P_0k)^2 + \Delta_s^2}}{(-P_0k_y + i\Delta_s)} Y_{n,s}$ and normalize $Y_{n,s}, Z_{n,s}$ ($Y_{n,s}^* Y_{n,s} + Z_{n,s}^* Z_{n,s} = 1$), we obtain

$$|Y_{n,s}|^2 = \frac{(P_0k_y)^2 + \Delta_s^2}{2 \left[(P_0k)^2 + \Delta_s^2 + nP_0k_x \sqrt{(P_0k)^2 + \Delta_s^2} \right]}. \quad (4.12)$$

Then we use the above equations, the Eq. (4.9) in this case becomes (the analytic result of Berry curvature)

$$\begin{aligned} & \Omega_{n=\pm 1}(\boldsymbol{\kappa}) \\ &= i \frac{\left[(-P_0)^2 \begin{pmatrix} Y_{n,s}^* & Z_{n,s}^* \end{pmatrix} \begin{pmatrix} 1 & 0 \\ 0 & -1 \end{pmatrix} \begin{pmatrix} Y_{-n,s} \\ Z_{-n,s} \end{pmatrix} \begin{pmatrix} Y_{-n,s}^* & Z_{-n,s}^* \end{pmatrix} \begin{pmatrix} 0 & 1 \\ 1 & 0 \end{pmatrix} \begin{pmatrix} Y_{n,s} \\ Z_{n,s} \end{pmatrix} - c.c. \right]}{4(P_0^2 k^2 + \Delta_s^2)} \hat{z} \\ &= \frac{i \left[P_0^2 (Y_{n,s}^* Y_{-n,s} - Z_{n,s}^* Z_{-n,s}) (Y_{-n,s}^* Z_{n,s} + Z_{-n,s}^* Y_{n,s}) - c.c. \right]}{4(P_0^2 k^2 + \Delta_s^2)} \hat{z} \\ &= \frac{n\Delta_s P_0^2}{2 \left[(P_0k)^2 + \Delta_s^2 \right]^{\frac{3}{2}}} \hat{z}. \end{aligned} \quad (4.13)$$

4.2.2 The Berry curvature of numerical result compare with the analytic result

This section we will use the Berry curvature analytic formulation Eq. (4.13) to compare with the numerical results which consider three K points(unperturb points and same energy).

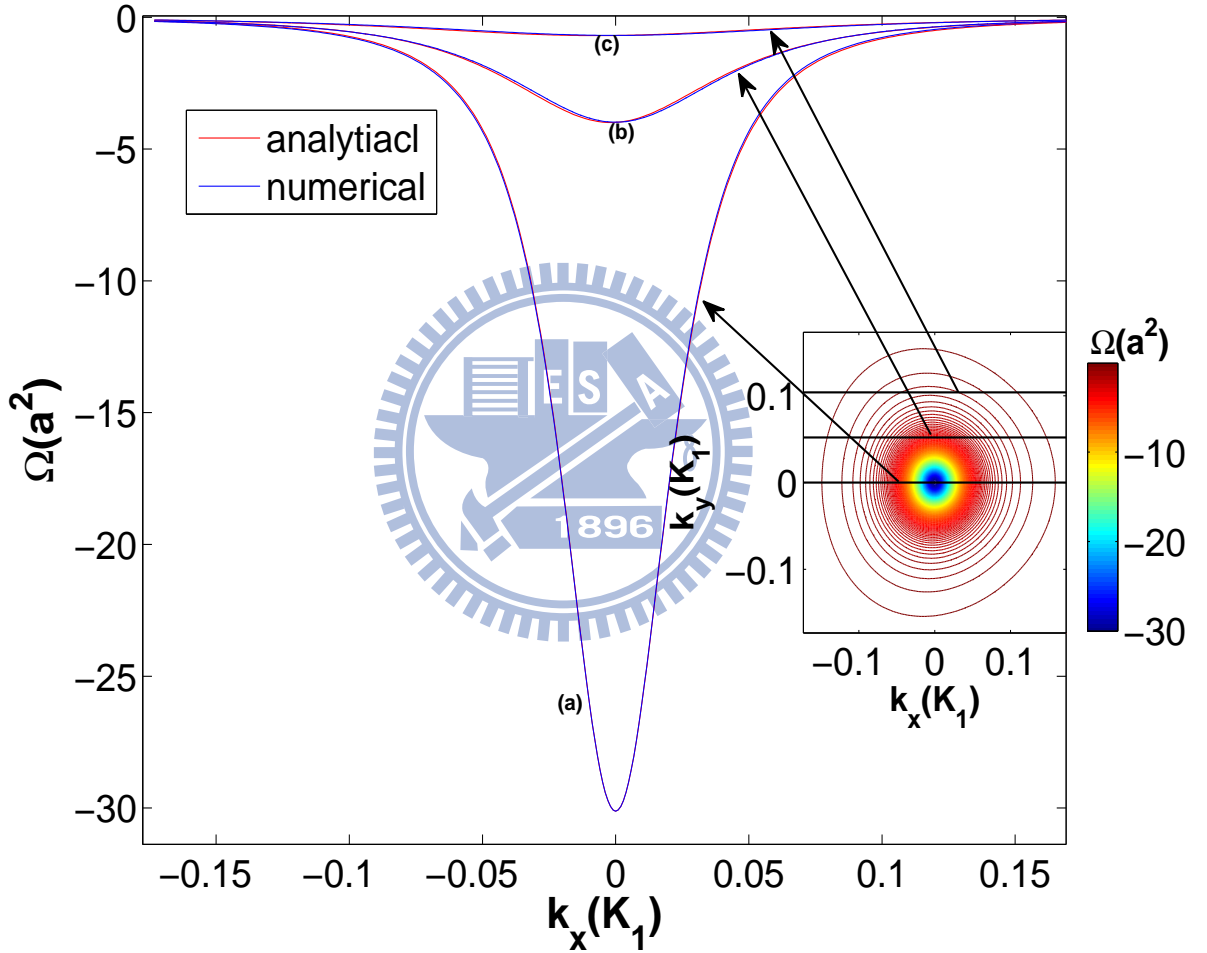


Figure 4.1: The inset shows the contour of Berry curvature for the lowest band (in spin-up case) by considering three K point and we chose (a) $k_y=0k_{y_{\max}}$, (b) $k_y=0.3k_{y_{\max}}$ and (c) $k_y=0.6k_{y_{\max}}$ (black line) corresponding to the dispersion which is expanded from K_1 ($k_x = k_y = 0$) in the main panel. The blue line is analytic result $n=-1, s=1$ ($C_{\text{range}}=1$); the red line is numerical result (the lowest band).

From the Fig. 4.1 and Fig. 4.2 we can observe the magnitude of analytic Berry curvature at K point confirm to the numerical result. The analytic Berry curvature match the

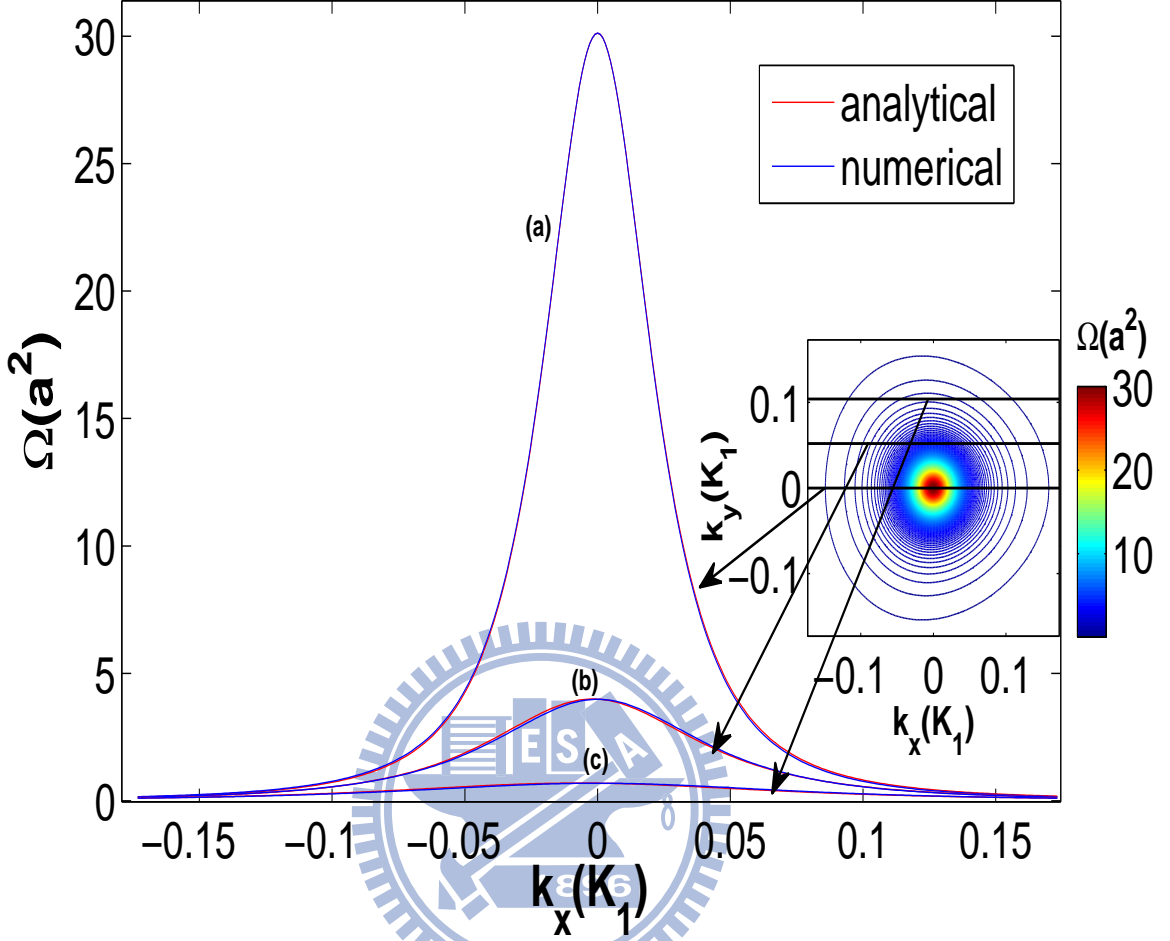


Figure 4.2: The inset shows the contour of Berry curvature for the second lowest band (in spin up case) by considering three K point and we chose (a) $k_y=0k_{y_{\max}}$, (b) $k_y=0.3k_{y_{\max}}$ and (c) $k_y=0.6k_{y_{\max}}$ (black line) corresponding to the dispersion which is expanded from K_1 ($k_x = k_y = 0$) in the main panel. The blue line is analytic result $n=1, s=1$ ($C_{\text{range}}=1$); the red line is numerical result (the second lowest band).

numerical results except K point.

The effect Berry curvature for first lowest energy band distribute around K point, and when C_{range} (shown in appendix A) increase the Berry curvature would stable ($C_{\text{range}} \approx 11$, are shown in Fig. 4.3).

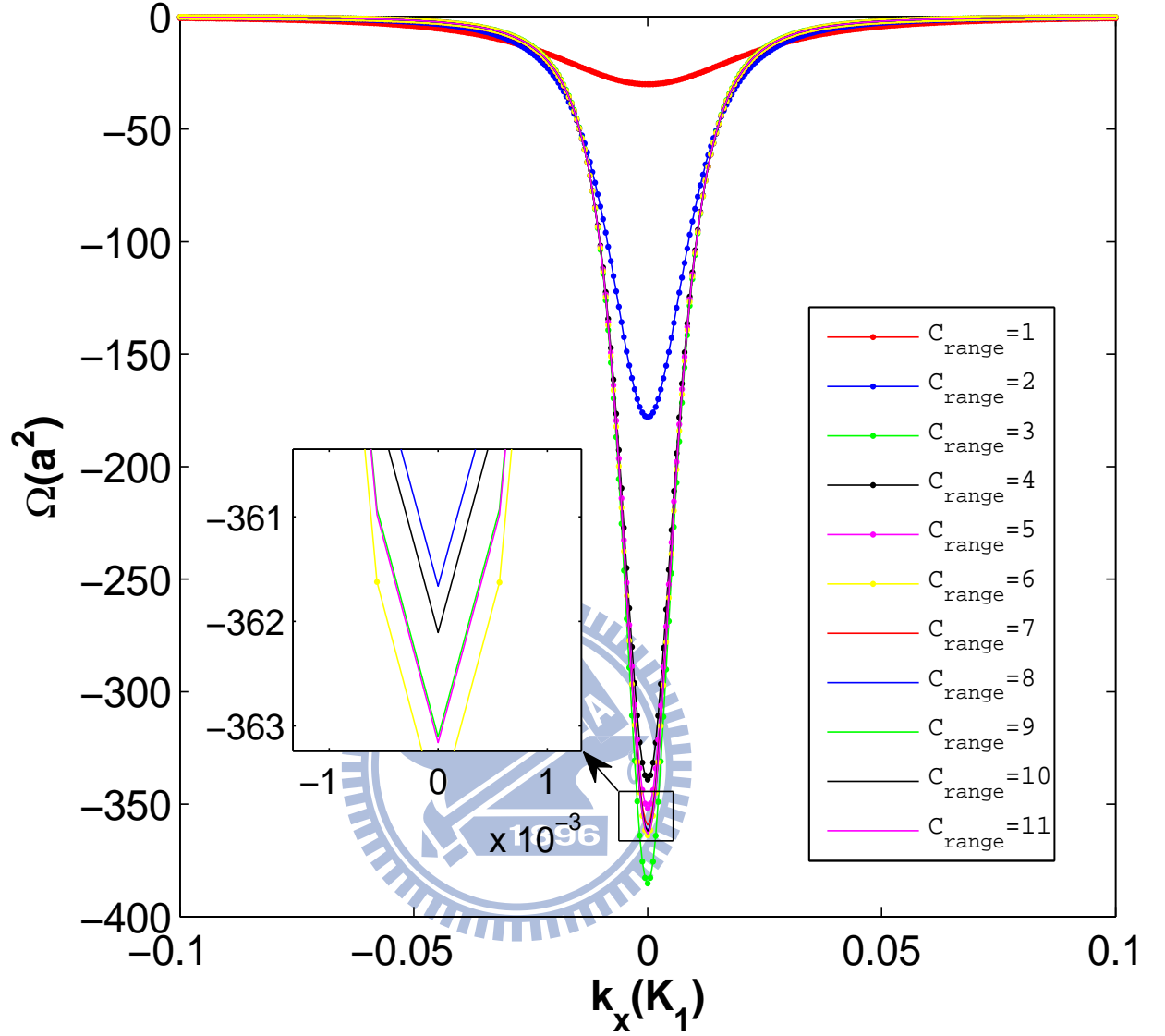


Figure 4.3: The C_{range} increase to 11, the numerical Berry curvature would almost stable.

4.2.3 The relationship between time reversal property and Berry curvature

The numerical results show that the spin-up and spin-down Berry curvatures are opposite sign (see Fig. 4.4 and Fig. 4.5), the curvature satisfies $\Omega_{n,s}(\boldsymbol{\kappa}) = -\Omega_{n,-s}(-\boldsymbol{\kappa})$. In this subsection, we will derive some symmetry relation of the Berry curvature. The specific symmetry we consider are the inversion symmetry (via parity operator π) and the time reversal symmetry (via time-reversal operator Θ). Our Hamiltonian H has the property

$[H, \boldsymbol{\pi}] = 0$ and $[H, \boldsymbol{\Theta}] = 0$. We start from the expression of the Berry curvature

$$\boldsymbol{\Omega}_n(\boldsymbol{\kappa}) = i \langle \nabla_{\boldsymbol{\kappa}} u_{\boldsymbol{\kappa},n} | \times | \nabla_{\boldsymbol{\kappa}} u_{\boldsymbol{\kappa},n} \rangle = \nabla_{\boldsymbol{\kappa}} \times \mathbf{A}_{n,s}(\boldsymbol{\kappa}), \quad (4.14)$$

where $\mathbf{A}_{n,s}(\boldsymbol{\kappa})$ is called Berry connection (like a vector potential in k-space), the curve of $\mathbf{A}_{n,s}(\boldsymbol{\kappa})$ is Berry curvature. Because of the inversion symmetry (proven by rotating 60° in chapter 3), we insert $\boldsymbol{\pi}\boldsymbol{\pi}^{-1}$ into Berry connection Eq. (4.14)

$$\mathbf{A}_{n,s}(\boldsymbol{\kappa}) = i \langle u_{\boldsymbol{\kappa},n,s} | \boldsymbol{\pi}\boldsymbol{\pi}^{-1} \nabla_{\boldsymbol{\kappa}} \boldsymbol{\pi}\boldsymbol{\pi}^{-1} | u_{\boldsymbol{\kappa},n,s} \rangle = i \langle u_{-\boldsymbol{\kappa},n,s} | \nabla_{\boldsymbol{\kappa}} | u_{-\boldsymbol{\kappa},n,s} \rangle = -\mathbf{A}_{n,s}(-\boldsymbol{\kappa}). \quad (4.15)$$

Here, we point out that $\boldsymbol{\pi}^{-1} \nabla_{\boldsymbol{\kappa}} \boldsymbol{\pi} = \nabla_{\boldsymbol{\kappa}}$ because $\boldsymbol{\kappa}$ in $\nabla_{\boldsymbol{\kappa}}$, or in $| \nabla_{\boldsymbol{\kappa}} u_{\boldsymbol{\kappa},n} \rangle$ is a classical vector, not an operator. Furthermore, $\boldsymbol{\pi}^{-1} e^{i\boldsymbol{\kappa}\cdot\mathbf{r}} | u_{\boldsymbol{\kappa},n,s} \rangle = e^{-i\boldsymbol{\kappa}\cdot\mathbf{r}} | u_{-\boldsymbol{\kappa},n,s} \rangle$, where $\boldsymbol{\pi}^{-1}\mathbf{r} = -\mathbf{r}\boldsymbol{\pi}^{-1}$, and $\boldsymbol{\pi}^{-1} | u_{\boldsymbol{\kappa},n,s} \rangle = | u_{-\boldsymbol{\kappa},n,s} \rangle$. The symmetry property of the Berry connection we obtain in Eq. (4.15) is for the same spin index but for opposite $\boldsymbol{\kappa}$. Corresponding, the symmetry property of Berry curvature is given by

$$\boldsymbol{\Omega}_{n,s}(\boldsymbol{\kappa}) = \nabla_{\boldsymbol{\kappa}} \times \mathbf{A}_{n,s}(\boldsymbol{\kappa}) = -\nabla_{\boldsymbol{\kappa}} \times \mathbf{A}_{n,s}(-\boldsymbol{\kappa}) = \boldsymbol{\Omega}_{n,s}(-\boldsymbol{\kappa}), \quad (4.16)$$

Eq. (4.16) is resulted from inversion symmetry. The symmetry relation for $\boldsymbol{\Omega}_{n,s}(\boldsymbol{\kappa})$, due to time-reversal symmetry is derived in following. Denoting $|\alpha\rangle = |u_{\boldsymbol{\kappa},n,s}\rangle$,

$|\beta\rangle = i \nabla_{\boldsymbol{\kappa}} |u_{\boldsymbol{\kappa},n,s}\rangle$ we have

$$\mathbf{A}_{n,s}(\boldsymbol{\kappa}) = i \langle u_{\boldsymbol{\kappa},n,s} | \nabla_{\boldsymbol{\kappa}} | u_{\boldsymbol{\kappa},n,s} \rangle = \langle \alpha | \beta \rangle. \quad (4.17)$$

Corresponding, we denote $|\tilde{\alpha}\rangle = \boldsymbol{\Theta} |\alpha\rangle = |u_{-\boldsymbol{\kappa},n,-s}\rangle$,

$|\tilde{\beta}\rangle = \boldsymbol{\Theta} |\beta\rangle = -i \nabla_{\boldsymbol{\kappa}} |u_{-\boldsymbol{\kappa},n,-s}\rangle$. We have the identity $\langle \alpha | \beta \rangle = \langle \tilde{\beta} | \tilde{\alpha} \rangle$ such that

$$\langle \alpha | \beta \rangle = \langle \tilde{\beta} | \tilde{\alpha} \rangle = i \langle \nabla_{\boldsymbol{\kappa}} \langle u_{-\boldsymbol{\kappa},n,-s} | \rangle | u_{-\boldsymbol{\kappa},n,-s} \rangle = -i \langle u_{-\boldsymbol{\kappa},n,-s} | \nabla_{\boldsymbol{\kappa}} | u_{-\boldsymbol{\kappa},n,-s} \rangle = \mathbf{A}_{n,-s}(-\boldsymbol{\kappa}),$$

$$(4.18)$$

Between the second and the third steps in Eq. (4.18), we used the relationship $(\nabla_{\boldsymbol{\kappa}} \langle u_{\boldsymbol{\kappa},n,s} |) |u_{\boldsymbol{\kappa},n,s}\rangle = -\langle u_{\boldsymbol{\kappa},n,s} | \nabla_{\boldsymbol{\kappa}} |u_{\boldsymbol{\kappa},n,s}\rangle$, which is derived as follows

$$\begin{aligned} \nabla_{\boldsymbol{\kappa}} \langle u_{\boldsymbol{\kappa},n,s} | u_{\boldsymbol{\kappa},n,s}\rangle &= 0 \\ \Rightarrow (\nabla_{\boldsymbol{\kappa}} \langle u_{\boldsymbol{\kappa},n,s} |) |u_{\boldsymbol{\kappa},n,s}\rangle + \langle u_{\boldsymbol{\kappa},n,s} | \nabla_{\boldsymbol{\kappa}} |u_{\boldsymbol{\kappa},n,s}\rangle &= 0 \\ \Rightarrow (\nabla_{\boldsymbol{\kappa}} \langle u_{\boldsymbol{\kappa},n,s} |) |u_{\boldsymbol{\kappa},n,s}\rangle &= -\langle u_{\boldsymbol{\kappa},n,s} | \nabla_{\boldsymbol{\kappa}} |u_{\boldsymbol{\kappa},n,s}\rangle. \end{aligned} \quad (4.19)$$

From Eq. (4.18), we obtain the Berry curvature

$$\nabla_{\boldsymbol{\kappa}} \times \mathbf{A}_{n,s}(\boldsymbol{\kappa}) = \nabla_{\boldsymbol{\kappa}} \times \mathbf{A}_{n,-s}(-\boldsymbol{\kappa}) = -\nabla_{-\boldsymbol{\kappa}} \times \mathbf{A}_{n,-s}(-\boldsymbol{\kappa}) = -\Omega_{n,-s}(-\boldsymbol{\kappa}). \quad (4.20)$$

Eq. (4.20) is resulted from time-reversal symmetry. Inversion and time-reversal symmetries together give us

$$\Omega_{n,s}(\boldsymbol{\kappa}) = -\Omega_{n,-s}(-\boldsymbol{\kappa}) = -\Omega_{n,-s}(\boldsymbol{\kappa}). \quad (4.21)$$

This symmetry in Eq. (4.20) is clearly demonstrate in our numerical results, presented in Fig. 4.4 and Fig. 4.5. Thus confirming the validity of our numerical calculation.

4.2.4 The numerical result of Berry curvature

This subsection shows the numerical results of Berry curvature for the lowest energy band and the second lowest energy band (the other figures for high energy band are showed in appendix D).

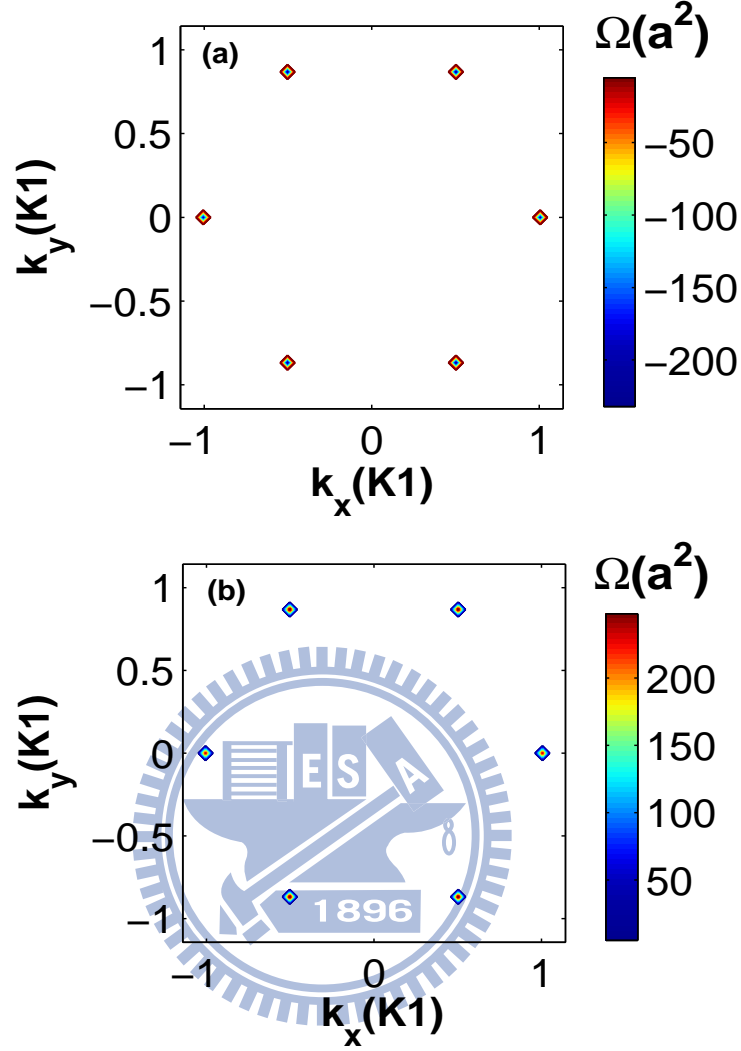


Figure 4.4: The Berry curvature of the lowest energy band for $n=1$ (a) the contour for spin-up (b) the contour for spin-down ($n'=2,3$); $\lambda=120\text{\AA}^2$ (InAs); $m^* = 0.023m_e$; $U_0 = 165\text{meV}$; $a=40\text{nm}$; $d=0.663a$ (where $k_x=k_y=0$ is Γ point).

The Berry curvature distributions imply that the energy difference with others band is the main effect and the wave function term is the minor effect for leading the main contribution of Berry curvature, we can observe these from Eq. (4.9). And the important information in Fig. 4.4 and Fig. 4.5 is that the periodic triangular lattice in our system with inversion symmetry ($K = K'$ in k -space), the Berry curvature distributions is the same at six corners of BZ.

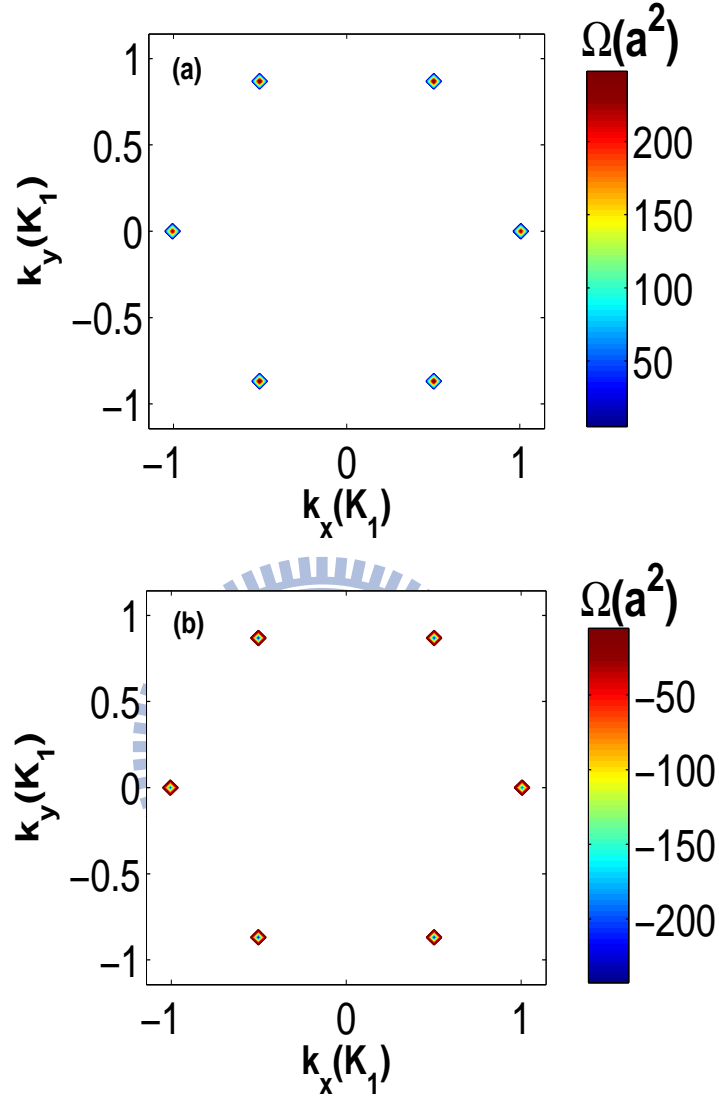


Figure 4.5: The Berry curvature of the second lowest energy band for $n=1$ (a) the contour for spin-up (b) the contour for spin-down ($n'=2,3$); $\lambda=120\text{\AA}^2$ (InAs); $m^* = 0.023m_e$; $U_0 = 165\text{meV}$; $a=40\text{nm}$; $d=0.663a$ (where $k_x=k_y=0$ is Γ point).

4.3 Brief summary and discussion

This chapter we introduced the Berry curvature which comes from the Berry phase, and also show the numerical results of Berry curvature for each energy bands in first BZ. Finally, we discuss the correlation between Berry curvature and time reversal property to guarantee the correct numerical results are correct.

However, the another important thing is to compare with the Berry curvature of graphene (see Fig. 4.6). Because of graphene without the inversion symmetry property (the Berry curvature $K \neq K'$, see Fig. 4.6 (b)), we can understand simply from Fig. 4.7.

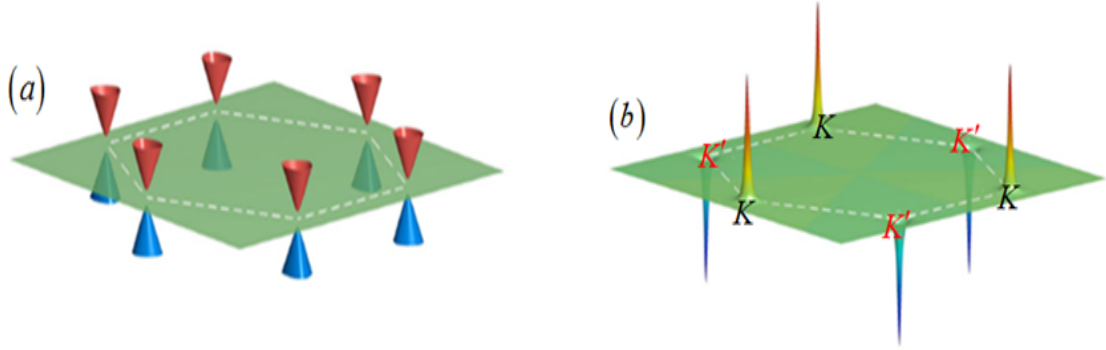


Figure 4.6: The (a) show the energy dispersion of graphene in BZ. (b) The Berry curvature of graphene in BZ. [15]

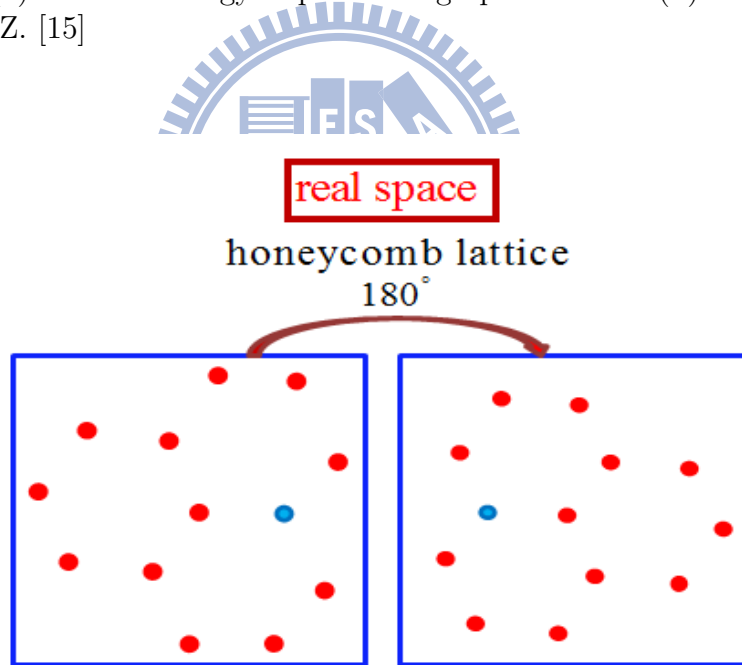


Figure 4.7: There are without rotating symmetry in graphene, which imply $K \neq K'$ in k-space (the blue point note the system which has been rotated).

Chapter 5

Searching for quantum spin Hall effect in our system

The QSH systems are insulating in the bulk, they have an energy gap separating the valence and conduction bands, but on the boundary they have gapless edge or surface states that are topologically protected and immune to impurities or geometric perturbations [16], [17],[18], [19].

Therefore, this chapter we will use the topological invariant (Chern number and Z_2 number) to examine the edge state and classify the insulator for open boundary case.

5.1 The Chern number of the energy band

The Chern invariant is rooted in the mathematical theory of fiber bundles (Nakahara, 1990), but it can be understood physically in terms of the Berry phase (Berry, 1984) associated with the Bloch wave functions $|u_n(\boldsymbol{\kappa})\rangle$. Provided there are no accidental degeneracies when \mathbf{k} is $|u_n(\boldsymbol{\kappa})\rangle$ transported around a closed loop, acquires a well defined Berry phase given by the line integral of $A_n = i \langle u_n | \nabla_{\boldsymbol{\kappa}} | u_n \rangle$. This may be expressed as a surface integral of the Berry flux (Berry curvature) $\mathcal{F}_n = \nabla \times A_n$. The Chern invariant is the total Berry flux in the Brillouin zone, and distinguishes the two states (bulk and

CHAPTER 5. SEARCHING FOR QUANTUM SPIN HALL EFFECT IN OUR SYSTEM

edge state) is a topological invariant similar to the genus.

The Chern theorem, which states that the integral of the Berry curvature over a close manifold is quantized in unit of 2π . This number is the so-called Chern number.

$$C_n = \frac{1}{2\pi} \int_{BZ} d^2\mathbf{k} \mathcal{F}_n. \quad (5.1)$$

The total Chern number, summed over all occupied bands, $C_{\text{occupied}} = \sum_{n=1}^N C_n$ that is invariant even if there are degeneracies between occupied bands, provided the gap separating occupied and empty bands remains finite. A fundamental consequence of the topological classification of gapped band structures is the existence of gapless conducting states at interfaces where the topological invariant changes. Such edge states are well known at the interface between the integer quantum Hall state and vacuum (Halperin, 1982) and deeply related to the topology of the bulk quantum Hall state.

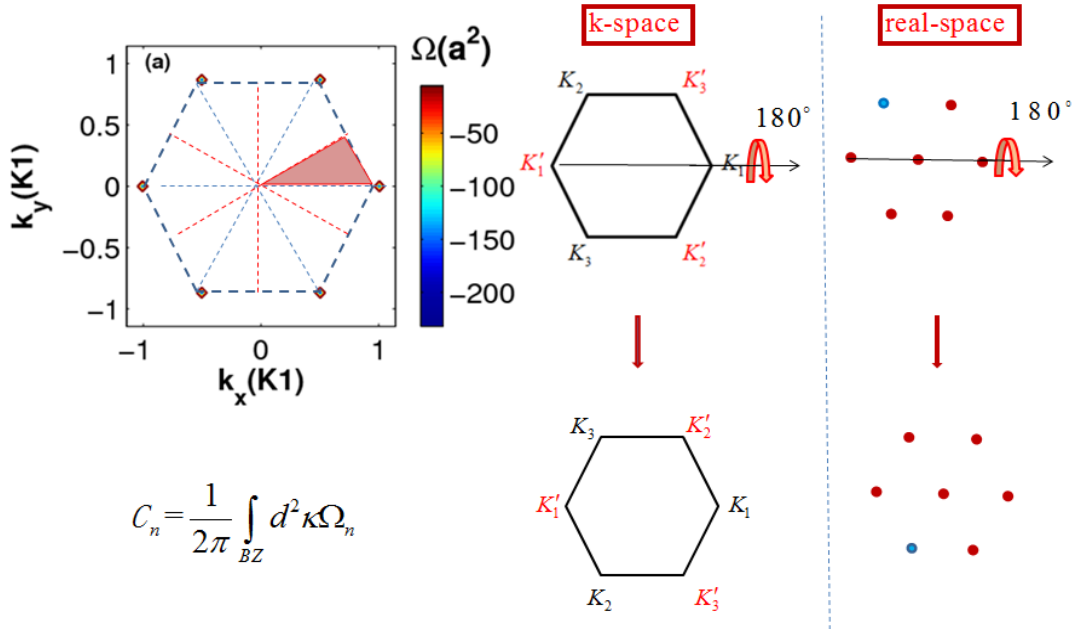


Figure 5.1: The rotating symmetry property for triangular lattice, the original system in real-space correspond to the BZ in k -space (top right), rotating x axis 180° the position in real-space is not change (the blue point note the system which has been rotated) and k_y becomes $-k_y$ in k -space (bottom right). The (a) shows the pink triangular is the smallest repeated unit cell in BZ.

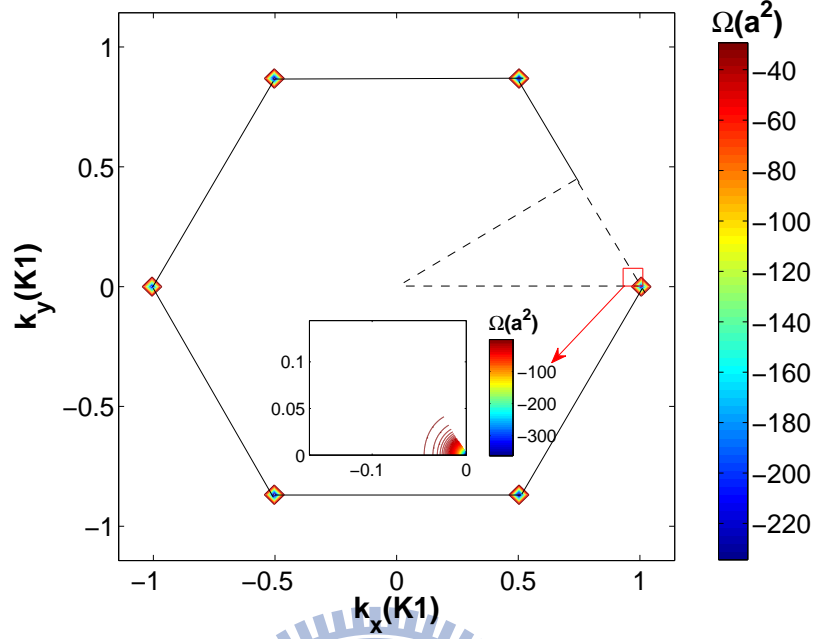


Figure 5.2: The hexagon black line shows the area of Brillouin zone and the area of triangle dashed line is the basic area for integrating which we mention at below in main panel, and the inset shows the contour of Berry curvature near K_1 (red box) is isotropic with κ .

In the process of integrating the first Brillouin zone (BZ) for Chern number (see Eq. (5.1)). We can use the property of rotating symmetry (triangular lattice ($K=K'$) and Fig. 5.1) for efficient numerical calculation, so we only need to integrate the area in first BZ which is overed one twelfth BZ (see the area of triangle dash line in Fig. 5.2). This integral result multiplies 12 is equivalent to the integration over all BZ. It's a convenient method for saving much time for numerical process.

$$C_n = \frac{1}{2\pi} \int_{BZ} \Omega_n \kappa d\kappa d\phi. \quad (5.2)$$

Because of the Berry curvature is isotropic from K or Γ (ex: the inset in Fig. 5.2), we use the cylindrical coordinate to be the basis axis (see Eq. (5.2)) to obtain the more complete data than using rectangular coordinates .

And the Chern numbers for each energy bands (which are showed in Fig. 5.7) actually are not a perfect integer for numerical results (C_a in Fig. 5.3), but the trend which is

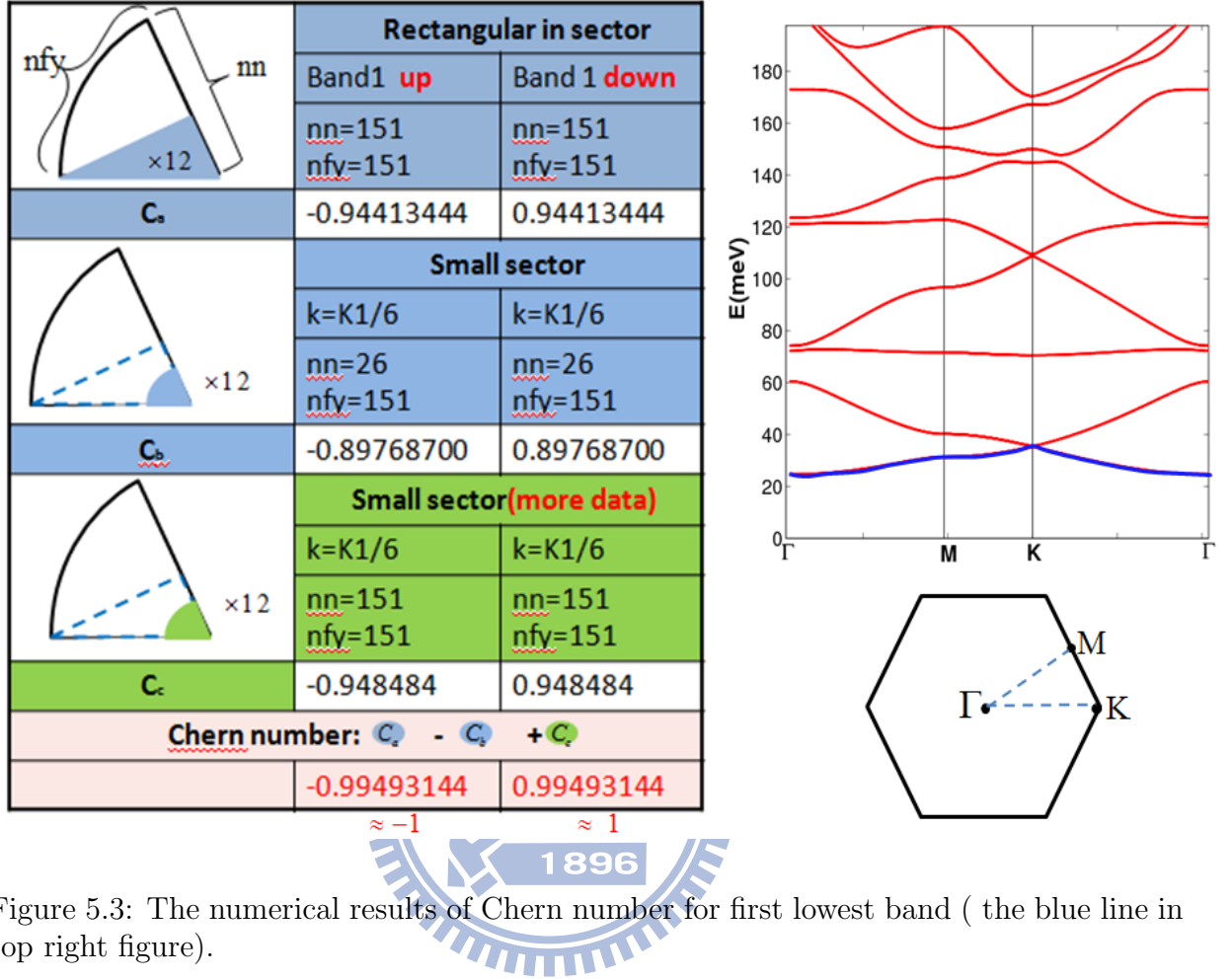


Figure 5.3: The numerical results of Chern number for first lowest band (the blue line in top right figure).

standing on more data from the effective contribution (ex: the effective contribution for first lowest energy band is around K point: C_c) shows the Chern number ($C_a - C_b + C_c$ see Fig. 5.3) will be an integer (be stable).

5.2 Z_2 invariant

A system with helical edge states is said to be in a QSH state, because there are a net spin flow forward along the top edge and backward along the bottom edge, just like the separated transport of charge in the quantum Hall (QH) state (see Fig. 5.4).

The calculation of S_z number (ν) is simpler if the crystal has extra symmetry . For instance, if the 2D system conserves the perpendicular spin S_z , then the up and down spins

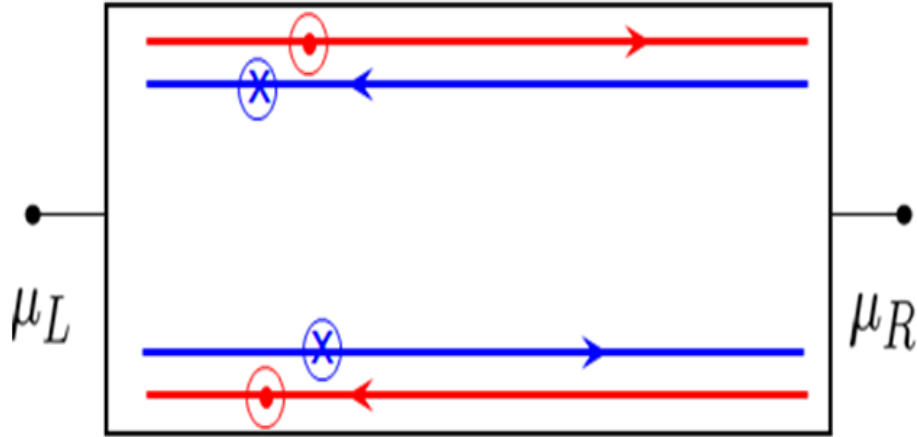


Figure 5.4: Quantum spin Hall effect: the upper edge contains a forward mover (like a magnetic field \mathbf{B} with \hat{z} direction) with up spin and a backward mover (like a magnetic field \mathbf{B} with $-\hat{z}$ direction) with down spin, and conversely for the lower edge.

have independent Chern integers $\mathcal{C}_\uparrow, \mathcal{C}_\downarrow$. Time reversal symmetry requires $\mathcal{C}_\uparrow + \mathcal{C}_\downarrow = 0$, and the difference $\mathcal{C}_\sigma = (\mathcal{C}_\uparrow - \mathcal{C}_\downarrow) / 2$ defines a quantized spin Hall conductivity (Sheng et al., 2006). The Z_2 invariant is then simply [20] as showed as below:

$$\nu = \mathcal{C}_\sigma \text{ mod } 2. \quad (5.3)$$

In our system, this case satisfies the aforementioned conditions. Therefore, the value of $\nu=0$ stands for conventional insulator and $\nu=1$ denotes quantum spin Hall insulator (see Fig. 5.5).

In Fig. 5.5 shows the Fermi energy is between conduction band and valence band in open boundary system. The QSH state occurs at the edge, because the topological Z_2 number change from $\nu=0$ (in vacuum) to $\nu=1$ (in semi-conductor).

The discussion for the term mod2 in Eq. (5.3) which comes from classifying topological insulator which is trivial or nontrivial in a small perturbation case (Fig. 5.6).

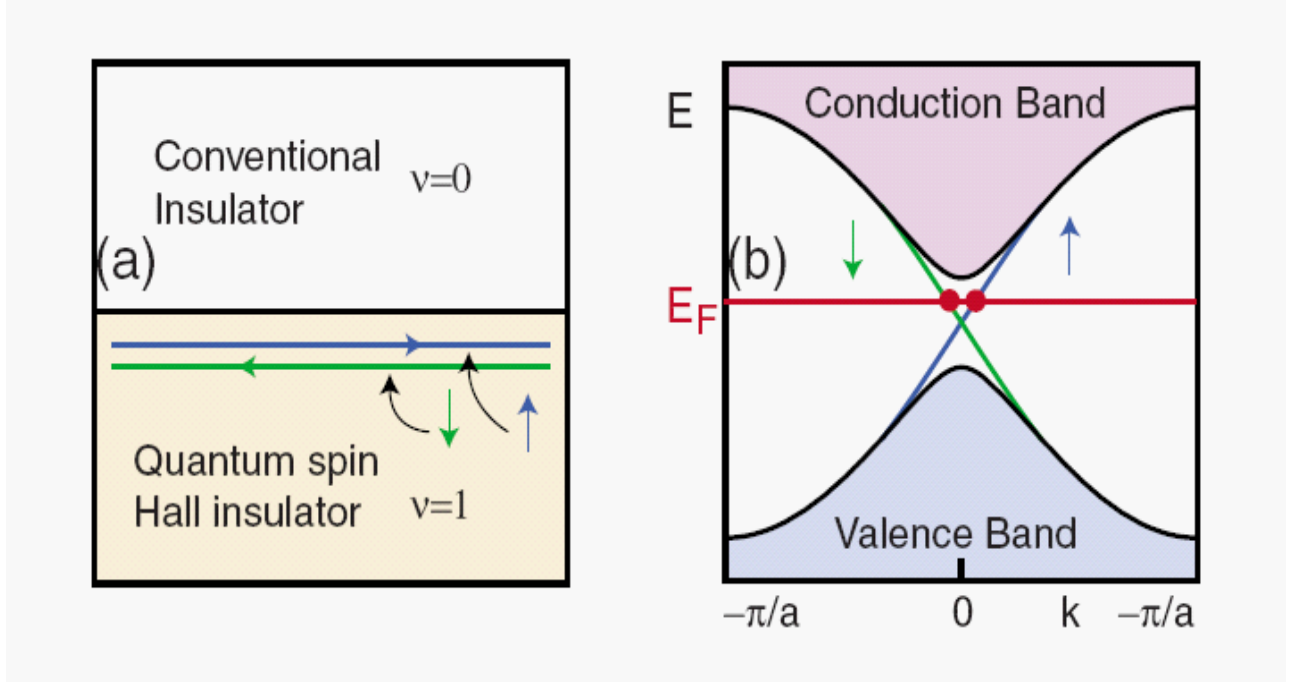


Figure 5.5: (Color online)Edge states in the quantum spin Hall insulator (QSHI). (a) The interface between a QSHI and an ordinary insulator. (b) The edge state dispersion in the graphene model in which up(blue arrow) and down(green arrow) spins propagate in opposite directions [20].

The surface states meet at an odd number (which associate with Z_2 number) of points with a small perturbation case in k -space, the QSH effect would occur. For example, there are a time reversal pair (in Fig. 5.6 right hand side) with Fermi level on the crossing point of edge state, the spin-up and spin-down states follow the time reversal symmetry $E(\boldsymbol{\kappa}, \boldsymbol{\sigma}) = E(-\boldsymbol{\kappa}, -\boldsymbol{\sigma})$, and in the perturbation case, the Kramers degeneracy ($\Theta H = H \Theta$, where H in Eq. (5.4); $H |n\rangle = E |n\rangle$, implies $|n\rangle$ and $\Theta |n\rangle$ have same E) is robust, which make the edge states (at the crossing point) be protected even in the present of a perturbation in system.

$$H = \left[\frac{\mathbf{p}^2}{2m^*} + V(\mathbf{r}) \right] + \left[\frac{-\lambda}{\hbar} \boldsymbol{\sigma} \cdot (\nabla V \times \mathbf{p}) \right]. \quad (5.4)$$

And another case (in Fig. 5.6 left hand side), when the surface states meet at an

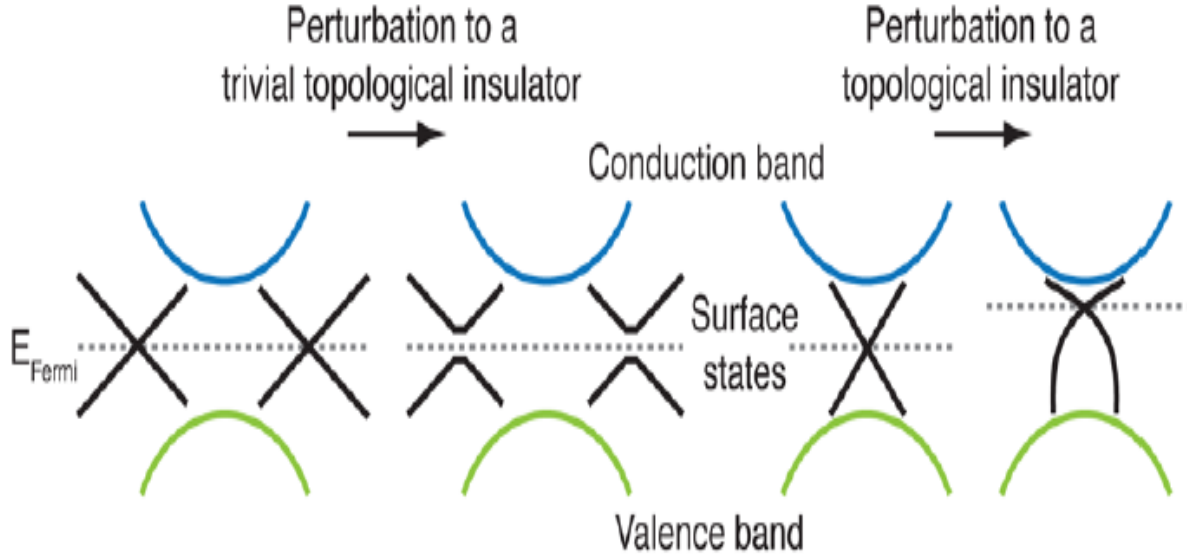


Figure 5.6: The sketches show the electronic structure (energy versus momentum) for a trivial insulator (left) and a strong topological insulator (right), such as $\text{Bi}_{1-x}\text{Sb}_x$. In both cases, there are allowed electron states (black lines) introduced by the surface that lie in the bulk band gap (the bulk valence and conduction bands are indicated by the green and blue lines, respectively). In the trivial case, even a small perturbation (changing the chemistry of the surface) can open a gap in the surface states, but in the nontrivial case, the conducting surface states are protected. (Illustration: Alan Stonebraker/stonebrakerdesignworks.com)

even number of points, the edge states (at the crossing point) would not be protected (meaning opened up gaps) because of the mixed states (at the crossing point) still yield Kramers degeneracy for a small perturbation case.

5.3 Brief summary

Topological classification is basic on the topological invariant (Chern number and Z_2 number) changes in bulk system, the special states at interfaces will exist for boundary. In this chapter, we have calculated the Chern number in bulk system for each band and expected to appear the edge states by the change invariant for open boundary case. And the another important point, the QSH state is expected in open boundary case by Z_2 number change. For example, the Chern number $\mathcal{C}_{\uparrow_{occupied}} = -1$, $\mathcal{C}_{\downarrow_{occupied}} = 1$ for Fermi

CHAPTER 5. SEARCHING FOR QUANTUM SPIN HALL EFFECT IN OUR SYSTEM

energy (can be modulated by Fig. 5.8) between first lowest energy band and second lowest energy band. We expect the spin-up and spin-down edge states will occur in open boundary case. And for QSH states, Because of the Z_2 number=1 for Fermi energy between first lowest energy band and second lowest energy band, the QSH states be expected in open boundary system (Fig. 5.7).

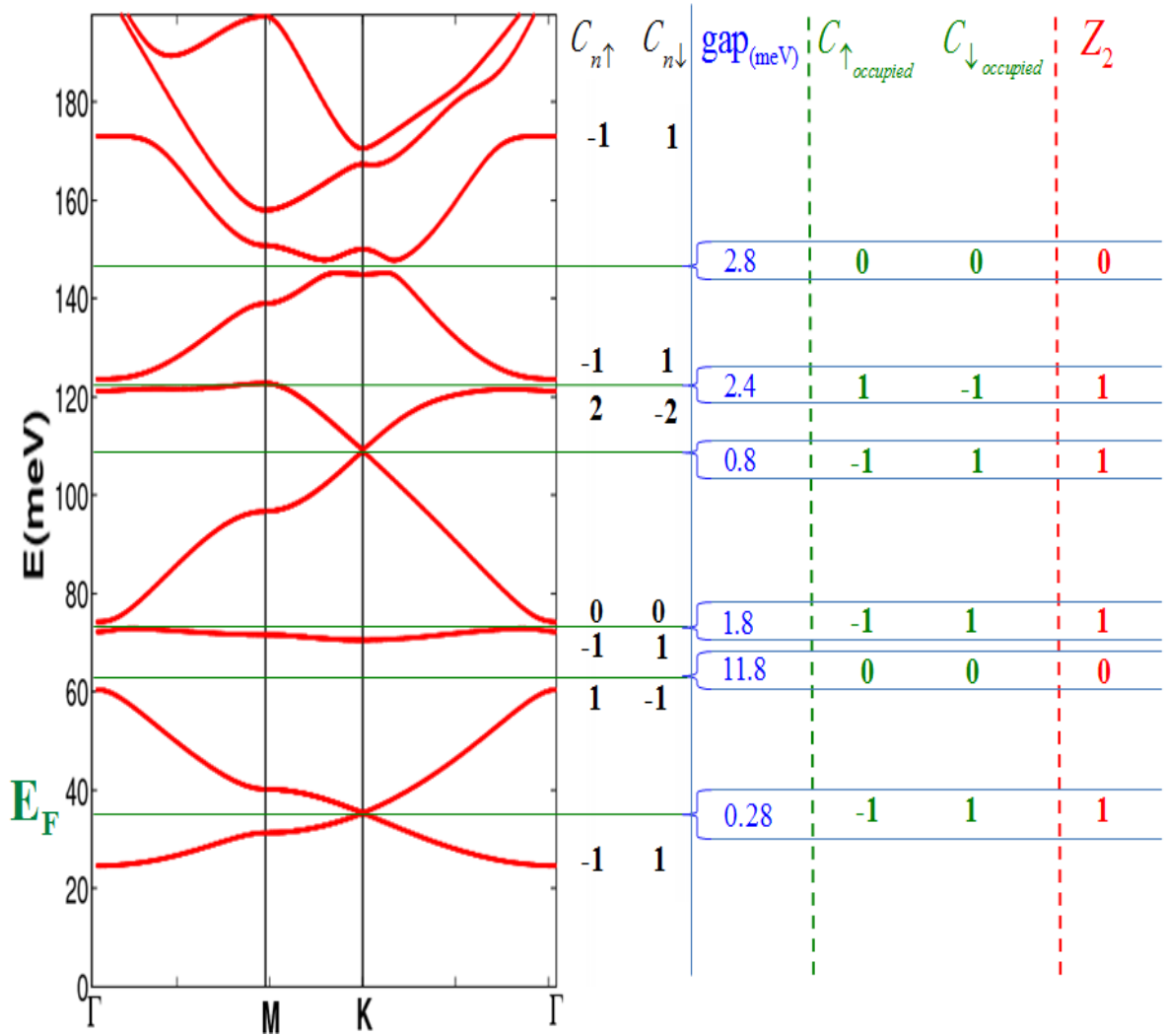


Figure 5.7: This figure shows Chern number of spin-up and spin-down for each energy bands and the comparison for Fermi energy, $C_{\uparrow_{occupied}}$, $C_{\downarrow_{occupied}}$, Z_2 number.

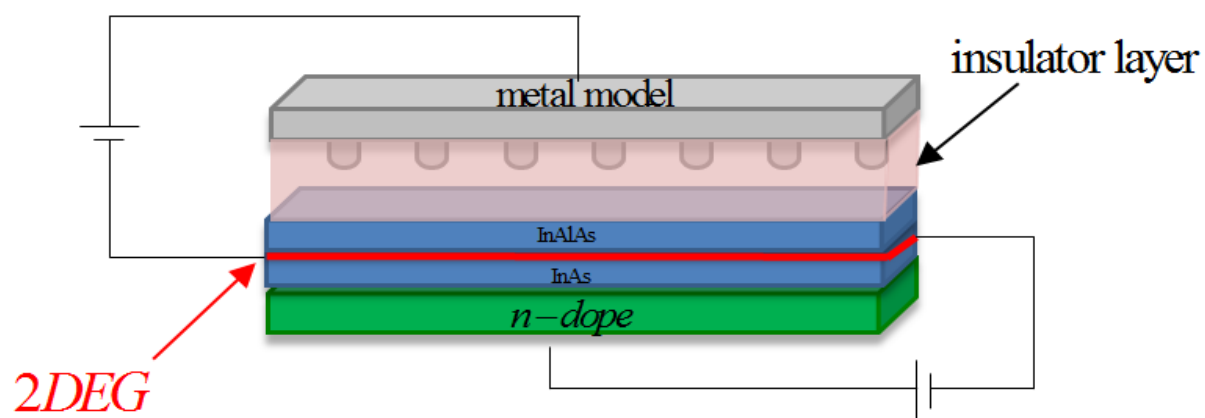


Figure 5.8: The setup of experiment, we use the external bias making the n-dope layer to control the Fermi energy.

Chapter 6

Conclusion and future work

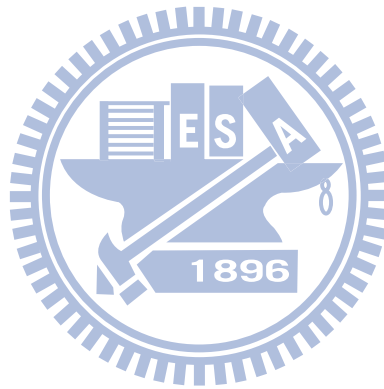
6.1 Conclusion

In conclusion, we show that by including the spin-orbit interaction due to the the muffin-tin potential lattice, the Dirac cones can open up to give global energy gap. The lattice is a triangular lattice and the spin-orbit interaction arises from the in-plane potential gradient of the potential lattice.

We have shown that the system can enter into a quantum spin Hall by changing the Fermi energy. This is concluded from our Chern number calculation. Our results show that, the Chern number for a energy band and for a given spin state can be nonzero ($C_{n,s} \neq 0$). This is different from that for graphene. It is due to the inversion symmetry in our system and the lack of inversion symmetry in graphene. Subsequently, our Chern number calculation shows that edge states could exist when the Fermi energy falls within certain energy intervals. Finally, we show from our Z_2 number result that quantum spin Hall states could exist when the Fermi energy falls within certain energy intervals.

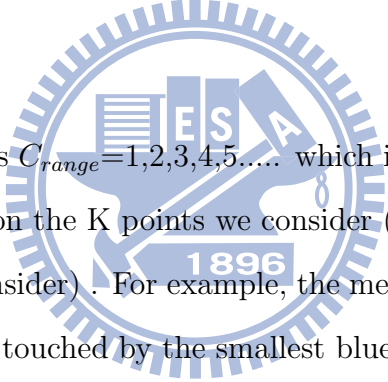
6.2 future work

In the future, we will study the case for the open boundary in our system. For an explicit calculation of the edge states. This will be compared against the conclusion from the topological classification arguments.



Appendix A

Labeling the periodic wave function basis K points



We labels the blue circles as $C_{range}=1,2,3,4,5,\dots$ which is corresponding to Fig. A.1. The number of C_{range} depends on the K points we consider ($N_K = 3C_{range}^2$, where N_K is the numbers of K points we consider) . For example, the meaning of $C_{range}=1$ is that we only consider the red points are touched by the smallest blue circle . In this case ($C_{range}=1$), the red points has three, and the blue circle is triangular form. All the numerical results which the values are stable about $C_{range}=11$ (about $\pm 10^{-3}$ difference).

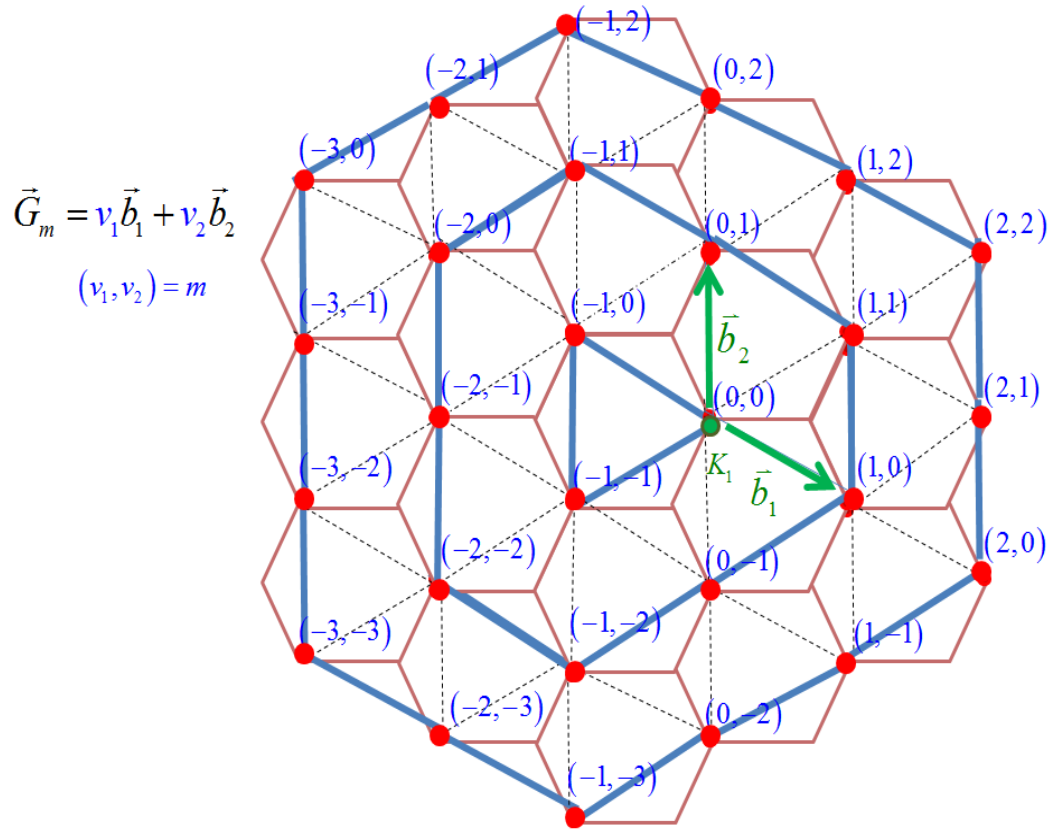


Figure A.1: The number m includes two index v_1, v_2 ; the green arrows denote the basis vector $\mathbf{b}_1, \mathbf{b}_2$ in k -space; the green point is K_1 which is the expanded point for wave function; the red points are all K points for m ; the hexagons are Brillouin zones and the blue circles are defined as a number: C_{range} .

Appendix B

The calculations about the periodic potential coefficient V'_m

In this appendix, we show how to determine the coefficient V'_m in Eq. (2.3). The 2DEG is modulated by a two-dimensional MTP array with the explicit potential form

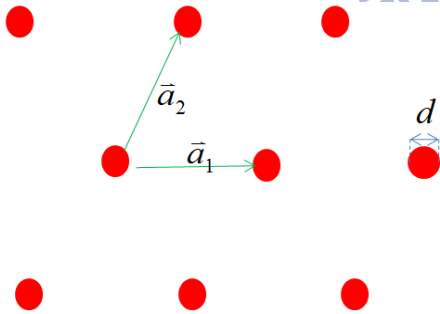


Figure B.1: A muffin-tin type with center-to-center distance a . The external potential energy is U_0 inside the disk with diameter d and zero outside the disk.

$$\begin{aligned}
V(\mathbf{r}) &= \sum_{ij} \tilde{V}(\mathbf{r} - \mathbf{R}_{ij}) \\
&= \sum_{i,j=-\infty}^{\infty} \tilde{V}\left(\mathbf{r} - 2\pi i \frac{\mathbf{a}_1}{2\pi} - 2\pi j \frac{\mathbf{a}_2}{2\pi}\right) \\
&= \sum_{ij} \tilde{V}\left(\mathbf{r} - \tau_1 \frac{\mathbf{a}_1}{2\pi} - \tau_2 \frac{\mathbf{a}_2}{2\pi}\right) \\
&= \sum_{i,j=-\infty}^{\infty} \tilde{V}(2\pi i, 2\pi j, \mathbf{r}) \\
&= \sum_{i,j=-\infty}^{\infty} \tilde{V}(\tau_1, \tau_2, \mathbf{r}),
\end{aligned} \tag{B.1}$$

where $\mathbf{R}_{ij} = i\mathbf{a}_1 + j\mathbf{a}_2$ ($\mathbf{a}_1, \mathbf{a}_2$ are the basis vectors in real space (see Fig. B.1)). Then we used Poisson sum formula (see Eq. (B.2)) cast the real-space infinite sum into the reciprocal-space sum.

$$\begin{aligned}
\sum_{i=-\infty}^{\infty} f(2\pi i) &= \frac{1}{2\pi} \sum_{v=-\infty}^{\infty} F(v) \\
F(v) &= \int_{-\infty}^{\infty} f(\tau) e^{-iv\tau} d\tau.
\end{aligned} \tag{B.2}$$

Therefore, we obtain the expression of periodic potential

$$\begin{aligned}
V(\mathbf{r}) &= \frac{1}{2\pi} \sum_{v_1=-\infty}^{\infty} \int_{-\infty}^{\infty} \frac{1}{2\pi} \sum_{v_2=-\infty}^{\infty} \int_{-\infty}^{\infty} \tilde{V}(\tau_1, \tau_2, \mathbf{r}) e^{-iv_1\tau_1} d\tau_1 e^{-iv_2\tau_2} d\tau_2 \\
&= \left(\frac{1}{2\pi}\right)^2 \sum_{v_1=-\infty}^{\infty} \sum_{v_2=-\infty}^{\infty} \int_{-\infty}^{\infty} \tilde{V}\left(\mathbf{r} - \frac{\tau_1}{2\pi} \mathbf{a}_1 - \frac{\tau_2}{2\pi} \mathbf{a}_2\right) e^{-iv_1\tau_1} e^{-iv_2\tau_2} d\tau_1 d\tau_2,
\end{aligned} \tag{B.3}$$

APPENDIX B. THE CALCULATIONS ABOUT THE PERIODIC POTENTIAL
COEFFICIENT V'_M

$$\begin{aligned}
 \mathbf{b}_1 &= 2\pi \frac{\mathbf{a}_2 \times \hat{z}}{\hat{z} \cdot (\mathbf{a}_1 \times \mathbf{a}_2)}, & \mathbf{b}_1 \cdot \mathbf{a}_1 &= 2\pi, \\
 & & \mathbf{b}_1 \cdot \mathbf{a}_2 &= 0, \\
 \text{where} & & \text{so} & \\
 \mathbf{b}_2 &= 2\pi \frac{\hat{z} \times \mathbf{a}_1}{\hat{z} \cdot (\mathbf{a}_1 \times \mathbf{a}_2)}, & \mathbf{b}_2 \cdot \mathbf{a}_2 &= 2\pi, \\
 & & \mathbf{b}_2 \cdot \mathbf{a}_1 &= 0, \\
 \mathbf{v} &= \sum_{\gamma}^2 v_{\gamma} \mathbf{b}_{\gamma}; \boldsymbol{\tau} = \sum_{\gamma}^2 \tau_{\gamma} \mathbf{a}_{\gamma}; \mathbf{v} \cdot \boldsymbol{\tau} = 2\pi \sum_{\gamma}^2 v_{\gamma} \tau_{\gamma}, & & \text{(B.4)}
 \end{aligned}$$

where \mathbf{v} is the vector in \mathbf{k} -space (\mathbf{b}_{γ} is basis vector in \mathbf{k} space); $\boldsymbol{\tau}$ is real-space vector, and $v_{\gamma}, \tau_{\gamma}$ are coefficients for those basis vectors, then we substitute Eq. (B.4) into Eq. (B.3) can obtain the intergral term show by

$$\begin{aligned}
 & \int \tilde{V}(\mathbf{r} - \frac{\boldsymbol{\tau}}{2\pi}) e^{-i\frac{\mathbf{v} \cdot \boldsymbol{\tau}}{2\pi}} d\tau_1 d\tau_2 \\
 &= (2\pi)^2 \int \tilde{V}(\boldsymbol{\tau}') e^{-i\mathbf{v} \cdot (\mathbf{r} - \boldsymbol{\tau}')} d\tau'_1 d\tau'_2 \\
 &= \frac{(2\pi)^2}{a_1 a_2 \sin 60^\circ} e^{-i\mathbf{v} \cdot \mathbf{r}} \int \tilde{V}(\boldsymbol{\tau}) e^{i\mathbf{v} \cdot \boldsymbol{\tau}} d\boldsymbol{\tau},
 \end{aligned} \tag{B.5}$$

where we use $\boldsymbol{\tau}' = \mathbf{r} - \frac{\boldsymbol{\tau}}{2\pi}$ in second row in Eq. (B.5), and the integral term in above equation is

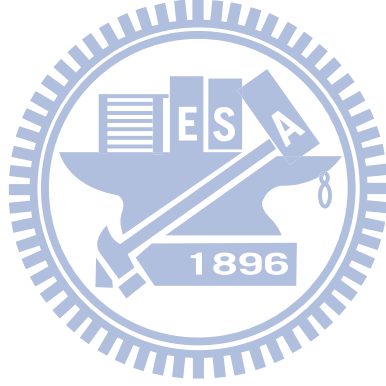
$$\begin{aligned}
 & \int \tilde{V}(\boldsymbol{\tau}) e^{i\mathbf{v} \cdot \boldsymbol{\tau}} d\boldsymbol{\tau} \\
 &= U_0 \int_0^{\frac{vd}{2}} e^{iv\tau \cos \phi} \tau d\phi d\tau = U_0 \int_0^{\frac{vd}{2}} \int_0^{2\pi} e^{ix \cos \phi} \frac{x}{v} d\phi \frac{1}{v} dx = U_0 \left(\frac{1}{v}\right)^2 \int_0^{\frac{vd}{2}} \int_0^{2\pi} \sum_{-\infty}^{\infty} (i)^n J_n(x) e^{in\phi} x d\phi dx \\
 &= U_0 \left(\frac{1}{v}\right)^2 \int_0^{\frac{vd}{2}} 2\pi J_0(x) x dx = 2\pi U_0 \left(\frac{1}{v}\right)^2 x J_1(x) \Big|_0^{\frac{vd}{2}} = \frac{\pi d U_0}{v} J_1\left(\frac{vd}{2}\right),
 \end{aligned} \tag{B.6}$$

then we substitute Eq. (B.6) into Eq. (B.5) to rewrite Eq. (B.3) in the form of

APPENDIX B. THE CALCULATIONS ABOUT THE PERIODIC POTENTIAL
COEFFICIENT V'_M

$$\begin{aligned}
 V(\mathbf{r}) &= \sum_{ij}^{\infty} \tilde{V}(\mathbf{r} - \mathbf{R}_{ij}) = \left(\frac{1}{2\pi}\right)^2 \frac{(2\pi)^2}{a_1 a_2 \sin \frac{\pi}{3}} \left(\sum_{v_2=-\infty}^{\infty} \sum_{v_1=-\infty}^{\infty} e^{-i\mathbf{v}\cdot\mathbf{r}} \frac{\pi U_0 d}{v} J_1\left(\frac{vd}{2}\right) \right) \\
 &= \sum_{v_1 v_2=-\infty}^{\infty} e^{i\mathbf{v}\cdot\mathbf{r}} \frac{2\pi U_0 d}{\sqrt{3} v a_1 a_2} J_1\left(\frac{vd}{2}\right) = \sum_m e^{i\mathbf{G}_m \cdot \mathbf{r}} V'_m,
 \end{aligned} \tag{B.7}$$

where $\mathbf{G}_m = \mathbf{v}$, and the coefficient $V'_m = \frac{2\pi U_0 d}{\sqrt{3} G_m a_1 a_2} J_1\left(\frac{G_m d}{2}\right)$.



Appendix C

The numerical results of high energy bands structure

This appendix shows the contours for the high energy bands structure, we can see obviously the two-dimensional bands structure are a periodic system (the physical property in the system can be expressed by the first BZ).

The numerical result in Fig. C.1 confirm the inversion symmetry $E(\boldsymbol{\kappa}) = E(-\boldsymbol{\kappa})$ ($K = K'$, the rotating symmetry which we have discussed in chapter 3) is vertical .

APPENDIX C. THE NUMERICAL RESULTS OF HIGH ENERGY BANDS STRUCTURE

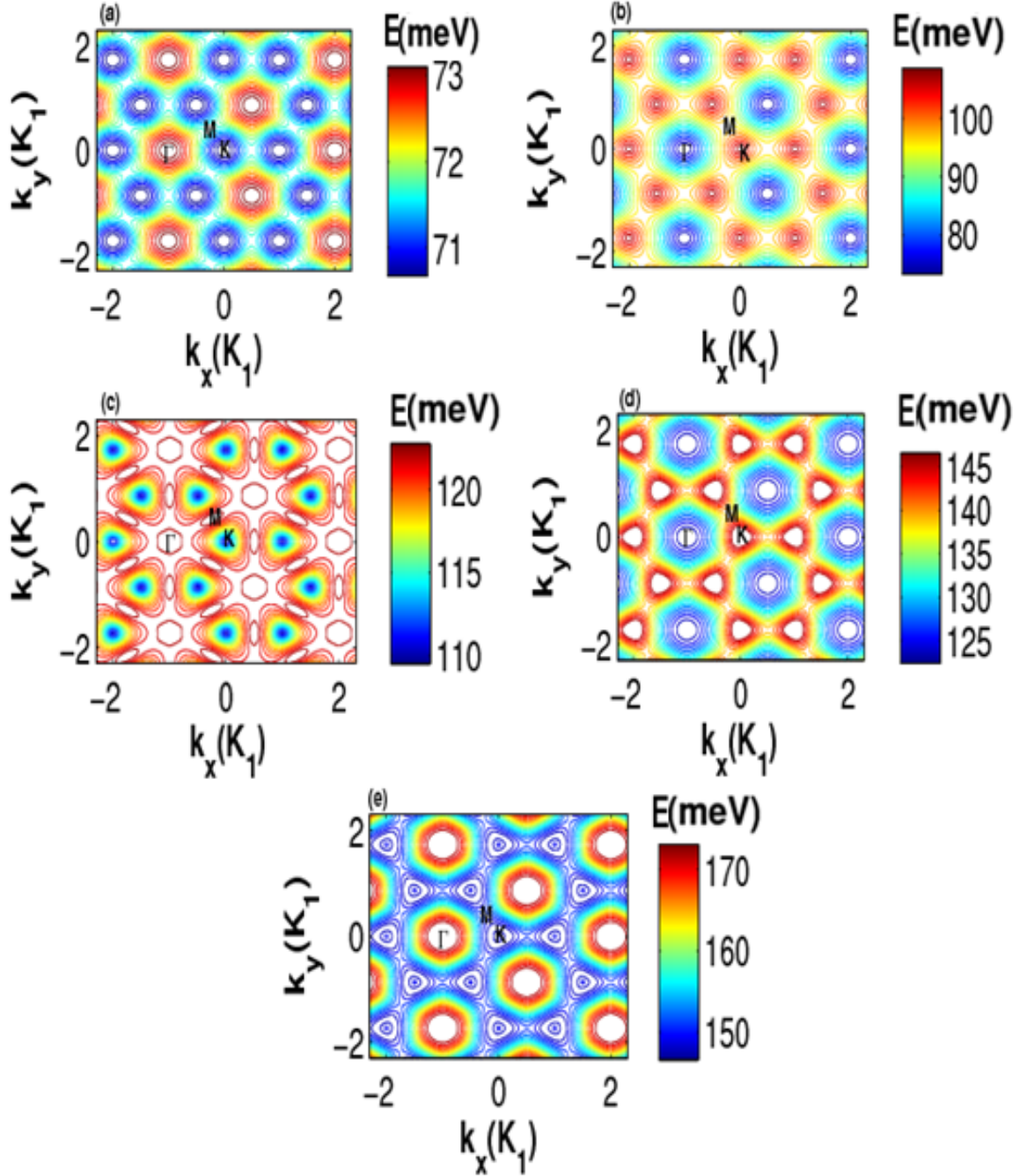


Figure C.1: This figure shows the contours of energy band structure without spin-orbit interaction for (a) the third lowest band (b) the fourth lowest band (c) the fifth lowest band (d) the sixth lowest band (e) the seventh lowest band, and the parameter is $m^* = 0.023m_e$, $a=40\text{nm}$, $d=0.663a$ and $U_0=165\text{ meV}$.

Appendix D

The Berry curvature of numerical results for high energy bands

This appendix will show the Berry curvature of numerical results with spin-orbit interaction for spin-up. The reason which we do not show the numerical results for spin-down electron is the magnitude of Berry curvature is as the same as spin-up electron but in different sign.

$$\Omega_n(\mathbf{k}) = i \sum_{n' \neq n} \frac{\langle u_{\mathbf{k},n} | \partial_{k_x} H(\mathbf{k}) | u_{\mathbf{k},n'} \rangle \langle u_{\mathbf{k},n'} | \partial_{k_y} H(\mathbf{k}) | u_{\mathbf{k},n} \rangle - (x \leftrightarrow y)}{[E_{n'}(\mathbf{k}) - E_n(\mathbf{k})]^2} \hat{z}. \quad (\text{D.1})$$

From Fig. D.2 we can see obviously the Berry curvature which the main variable for the curve is controlled by the energy difference (comparing with Eq. (D.1) and Fig. C.1).

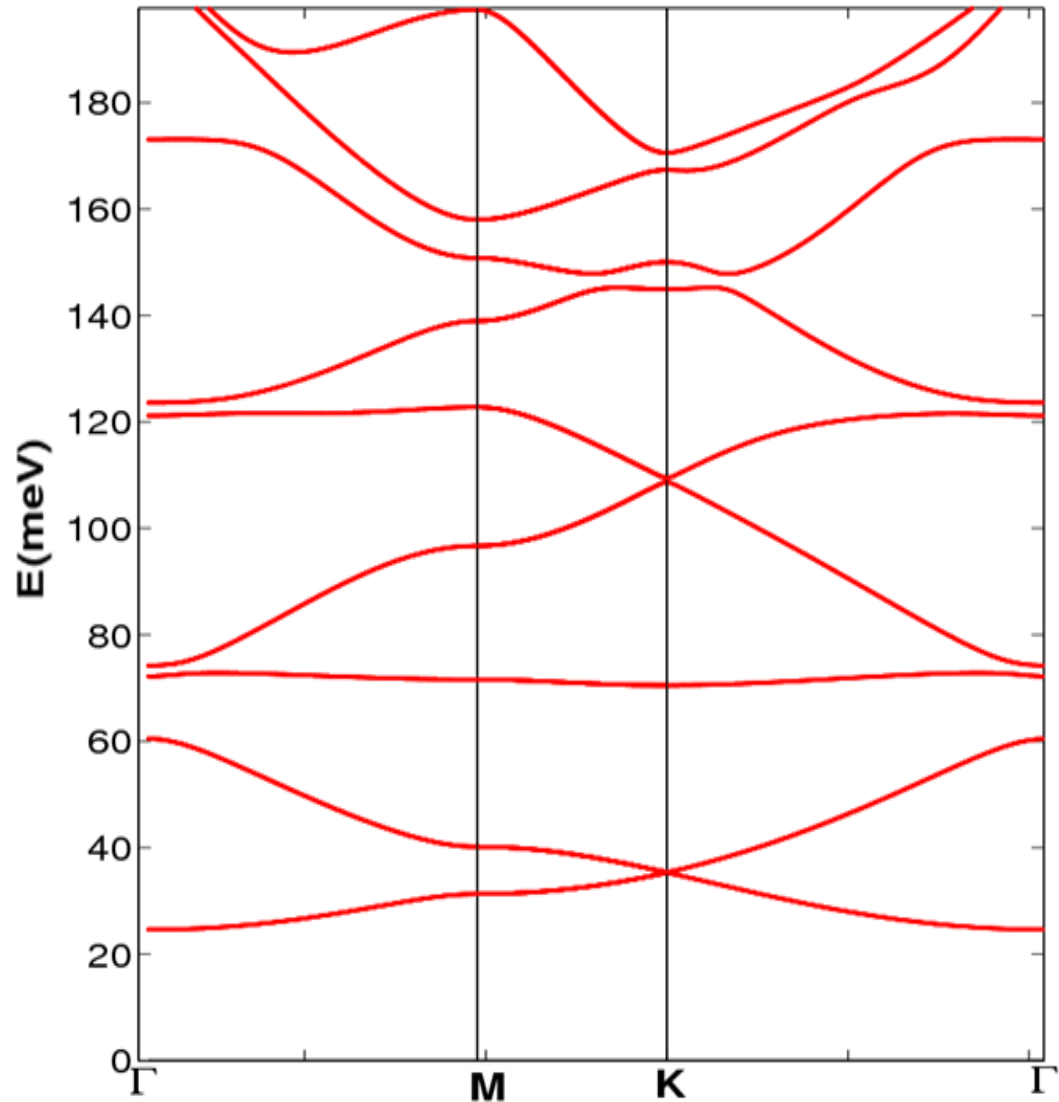


Figure D.1: The energy dispersion in present SOI in our system, and the parameters are $m^* = 0.023m_e$, $a=40\text{nm}$, $d=0.663a$ and $U_0=165\text{ meV}$.

APPENDIX D. THE BERRY CURVATURE OF NUMERICAL RESULTS FOR HIGH ENERGY BANDS

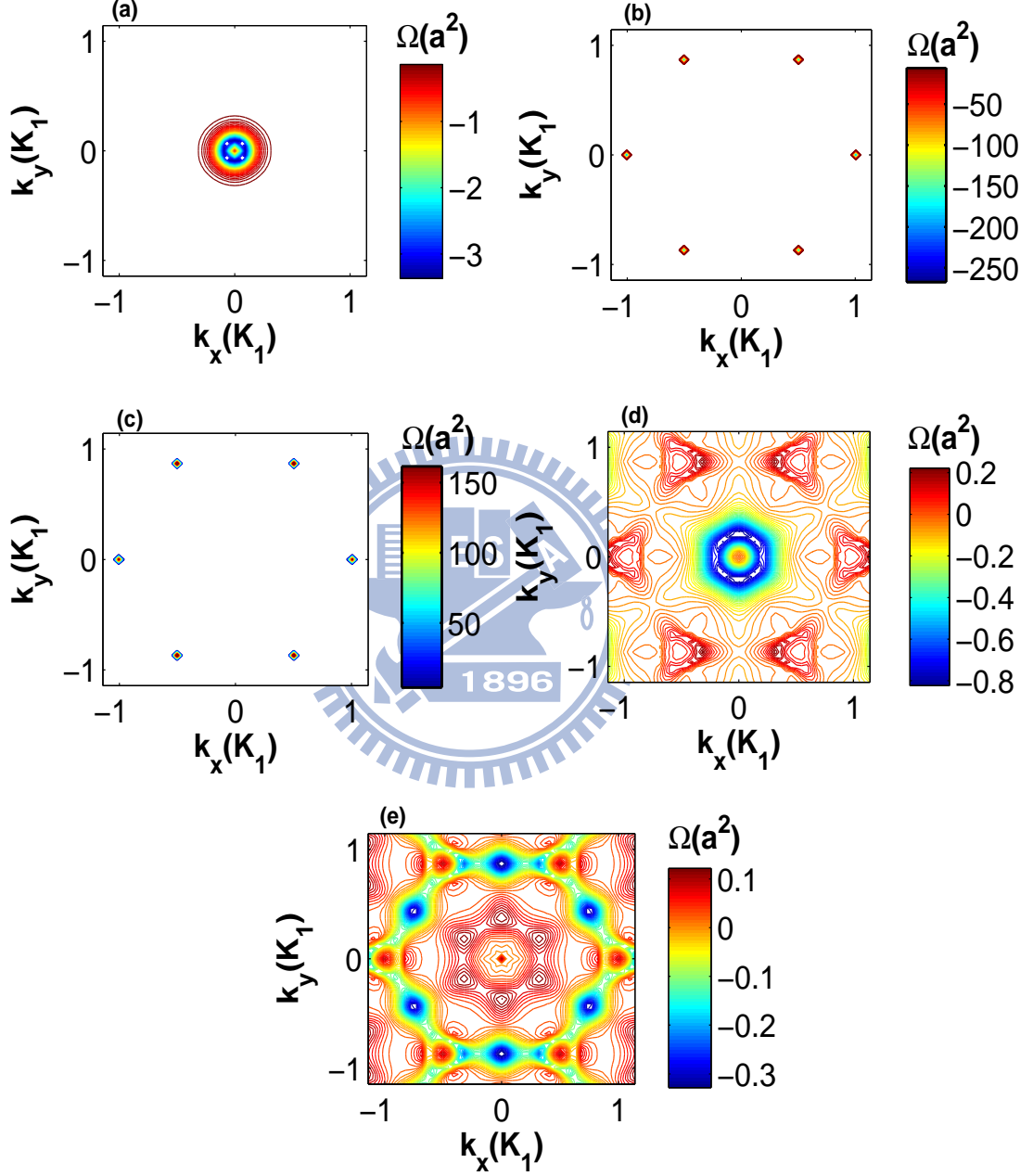


Figure D.2: This figure shows the contours of Berry curvature of numerical results with spin-orbit interaction for spin-up (a) the third lowest band (b) the fourth lowest band (c) the fifth lowest band (d) the sixth lowest band (e) the seventh lowest band. (where $m^* = 0.023m_e$, $a=40\text{nm}$, $d=0.663a$ and $U_0=165\text{ meV}$; $k_x = k_y = 0$ is Γ point.)

Appendix E

The other parameters for our system

In this thesis we only demonstrate one parameter ($a=40\text{nm}$, $d=0.663a$, $U_0=165\text{meV}$), so this appendix shows the other parameters for various a (the spatial period distance for MTP), and d (the potential disk diameter) and U_0 (external potential energy).

$$E_{gap} = 2\sqrt{3}A\lambda W. \quad (\text{E.1})$$

We can use the analytical formulation of energy gap (obtained in chapter3 Eq. (E.1)) for the lowest two band to roughly estimate the magnitude of gap with other parameters, where $A = \frac{K_0^2}{2\sqrt{3}}$ and $W = \frac{2\pi U_0 d}{\sqrt{3}K_0 a^2} J_1\left(\frac{K_0 d}{2}\right)$, ($K_0 = \frac{4\pi}{\sqrt{3}a}$). We notice that W is proportional to U_0 such that E_{gap} increase with increasing U_0 . The Fig. E.1 show the available parameters for obtain the results have same physic property (global gap). The reason why we didn't plot $a < 15\text{nm}$ is the limit of the experiment, and we hope to find the large gap and high degree of a . Fig. E.1 shows that E_{gap} is plotted by varying a and d for a given $U_0=165\text{meV}$. The dashed curve denotes the Dirac cone boundary and Dirac can not occur below this dashed curve in Fig. E.1(a). Fig. E.1(b) and (c) show the energy bands without global gap and with global gape, respectively.

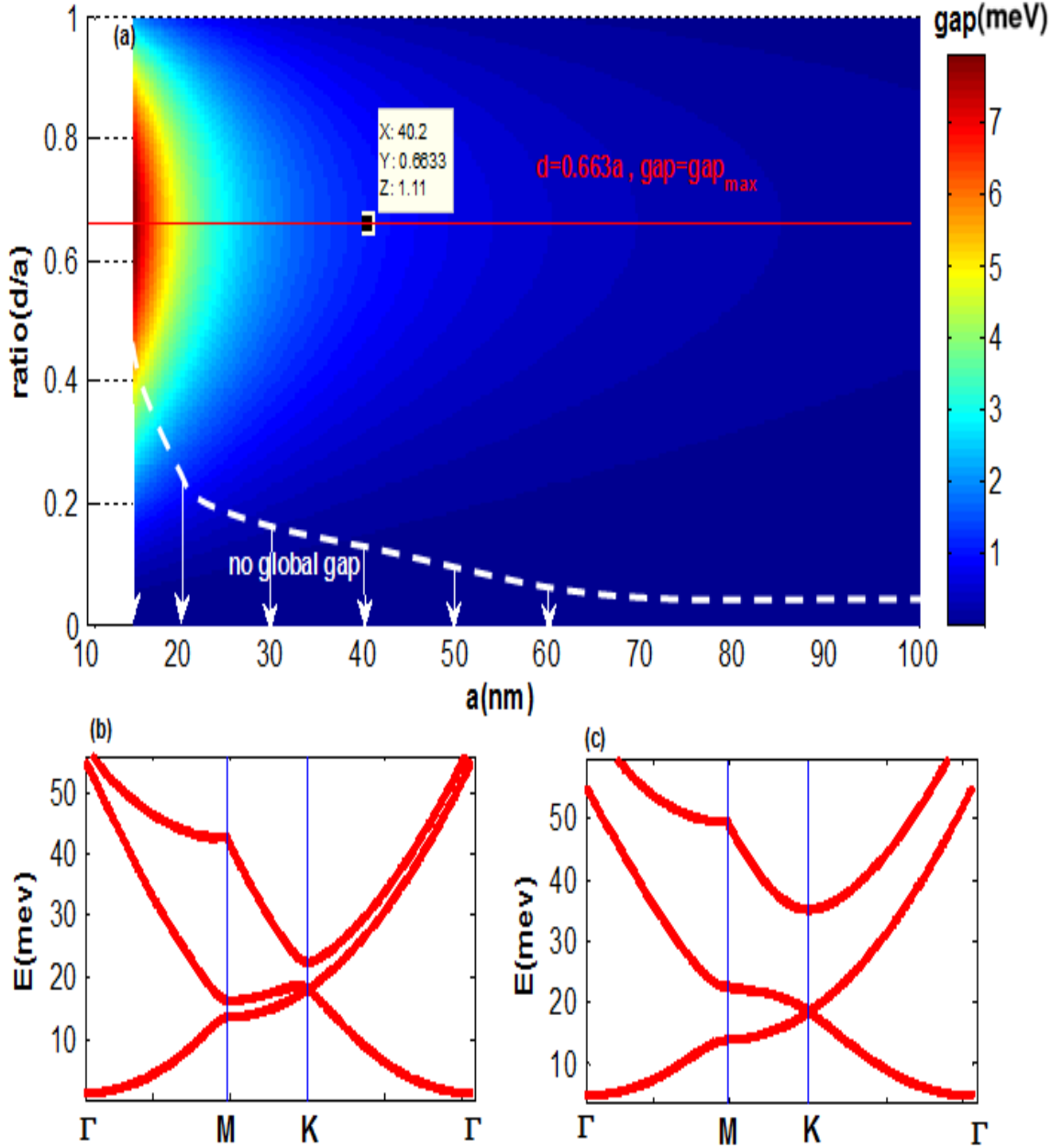


Figure E.1: (a) The contour plot of the energy gap for the lowest two bands by various parameters a , d but a fixed $U_0=165$ meV. The red line denotes the maximum gap when $d/a=0.663$ for all a , the white arrows denote that the systems without global gap at K point for $a=15, 20, 30, \dots$ (nm) correspond to those rates, so we roughly estimate the minimum rate line is the white dashed line for having global gap. (b) The global gap does not exist for $d=0.1a$, $a=40$ nm (c) The global gap does exist when $d=0.2a$, $a=40$ nm.

Bibliography

- [1] *Tight-Binding Based Modelling of Graphene Antidot Structures*, René Petersen.
- [2] *Topics in advanced quantum mechanics*, Barry R. Holstein (Addison Wesley).
- [3] H.-A. Engel, B. I. Halperin, and E. I. Rashba, Phys. Rev. Lett. **95**, 166605 (2005).
- [4] *Spin-Orbit Coupling in Two-Dimensional Electron and Hole systems*, Roland Winkler (Springer, 2003).
- [5] E.I.Rashba, Physica E 34, 31 (2006).
- [6] C.L. Kane and E.J. Mele, Physical Review Letters 95, 226801 (2005).
- [7] F.D.M. Haldane, Physical Review Letters 61, 2015 (1988).
- [8] B.A. Bernevig, T.L. Hughes and S.C. Zhang, Science 314, 1757 (2006).
- [9] Markus König, Steffen Wiedmann, Christoph Brune, Andreas Roth, Hartmut Buhmann, Laurens W. Molenkamp, Xiao-Liang Qi, and Shou-Cheng Zhang, Published online (2007); 10.1126/science.1148047.
- [10] B.A. Bernevig and S.C. Zhang, Physical Review Letters 96, 106802 (2006).
- [11] Marco Gibertini, Achintya Singha, Vittorio Pellegrini, and Marco Polini*, Phys. Rev. B, **79**, 121306, 241406(R) (2009).
- [12] C.-H. Park and S. G. Louie, Nano Lett. **9**, 1793 (2009).

BIBLIOGRAPHY

- [13] H.-A. Engel, B. I. Halperin, and E. I. Rashba, *Phys. Rev. Lett.* **95**, 166605 (2005).
- [14] Berry, M. V., *Proceedings of the Royal Society of London. A. Mathematical and Physical Sciences* 392 (1802): 45V57.(1984).
- [15] Xiao and Yao et al, *Phys. Rev. Lett* (2008).
- [16] C. L. Kane and E. J. Mele, *Phys. Rev. Lett.* *95*, 226801 (2005).
- [17] B.A. Bernevig and S.C. Zhang, *Phys. Rev. Lett.* *96*, 106802 (2006).
- [18] J. E. Moore and L. Balents, *Phys. Rev. B*, *75*, 121306 (2007);R. Roy, *Phys. Rev. B* *79* 195322 (2009).
- [19] X. L. Qi, T. Hughes and S. C. Zhang, *Phys. Rev. B* *78*, 195424 (2008).
- [20] Shou-cheng Zhang, *Physics* *1*, 6 (2008).

